

Direct Synthesis of 2D/3D Carbon Hybrid
Material and Its Application

Dissertation

zur Erlangung des Doktorgrades der Naturwissenschaften
(Dr. rer. nat.)

der

Naturwissenschaftlichen Fakultät II
Chemie, Physik und Mathematik

der Martin-Luther-Universität
Halle-Wittenberg

vorgelegt von

Herrn Xubin Lu
geb. am 10.07.1984 in China

Declaration

I declare that this thesis was composed by myself, that the work contained herein is my own except where explicitly stated otherwise in the text, and that this work has not been submitted for any other degree or professional qualification except as specified.

Reviewed by:

Prof. Dr. Michael Bron

Prof. Dr. Mehtap Öezaslan

Date of submission: 10.09.2019

Date of oral presentation: 05.03.2020

Halle(Saale)

Xubin Lu

Acknowledgements

I would like to express my deep and sincere appreciation to my supervisor, Prof. Dr Michael Bron. Thank you for your toleration and broad-mindedness all the time. Thank you for offering me a precious chance to go on my scientific work. I also would like to show my gratitude to Prof. Dr Michael Bron for giving me enough freedom to develop my own scientific creativity. His extensive knowledge and his logical way of thinking have been of great value for me.

I am sincerely indebted to my supervisor, Prof. Dr. Bernd Abel, Professor of Leibniz Institute of Surface Engineering (IOM), Wilhelm-Ostwald-Institute for Physical and Theoretical Chemistry and Institute of Chemical Technology of the University Leipzig for his support and insightful discussions during my work. My gratitude and appreciation are also extended to Dr. Aron Varga for several valuable ideas and discussions.

It is my particular wish to thank Prof. Dr. h.c. Bernd Rauschenbach, Professor of Leibniz Institute of Surface Engineering for his great help and support.

I would like to thank Prof. Dr. Jia Li, Professor of Tsinghua University and the membership of his group: Mr. Xin Yang and Mr. Xi Wu for the calculations of DFT and intellectual discussions.

During this work, I have collaborated with all my colleagues for whom I have great regard, and I wish to extend my thanks to Mr. Eik Koslowski and Mrs. Annett Quetschke for XPS, XRD, and TEM measurements, My thanks are also given to Dr. Sabine Schimpf for the safety training and CVD guide, and our group secretary Mrs. Anki Hassi for her help and administrative support. I also received a lot of valuable comments from Dr. Matthias Steimecke, who offered the training of Raman spectroscopy. I am grateful for the excellent technical support of Mr. Roland Schlosser. I wish to express my sincere thanks to Dr. Stefan Rümmler and Mark Hartman for the valuable discussion during our office hours. I also wish to thank Mrs. A. Prager, Dr. Fan Li, Dr. Chang Yang, Haojie Zhang, Dr. Kai Chang and Tariq Muhammad for XPS, I-V, STM, SEM and AFM measurements and valuable discussions. It is my particular wish to thank all my friends from Leipzig, Jena, and Bochum. They made the last couple of years to some of the best in my life.

I owe my loving thanks to my family: to my parents, my brother, my sister and particularly to my wife and my son for always giving me support, strength and hope. To their, I dedicate this thesis.

This work would not have been possible without support the Chinese scholarship council (CSC).

Xubin Lu

von-Danckelmann-Platz 4

Curriculum Vitae

Halle, 06120, Germany

xubin.lu@chemie.uni-halle.de

Education:

- | | |
|---|---|
| 2016~2019
<i>Ph.D candidate</i> | Industrial Chemistry of renewable energies, Martin Luther University, Halle-Wittenberg, Germany
Prof. Dr. Michael Bron
Direct synthesis of 2D/3D carbon hybrid material and its application |
| 2013~2016
<i>Ph.D candidate</i> | Chemistry Department of the Leibniz Institute of Surface Modification (IOM)
Prof. Dr. Bernd Abel and Dr. Aron Varga
Functionalized Carbon Materials in Solid Acid Fuel Cell Electrodes |
| 2010~2013
<i>Master of Science</i> | School of Chemistry and Chemical Engineering, Shaanxi Normal University (SNNU)
Prof. Dr. Zenglin Wang
Research and Development of Electroplating Copper Solution with High Filling Capability for Microvia Hole |
| 2006~2010
<i>Bachelor of Science</i> | Department of Chemistry and Chemical Engineering, Hexi Normal University (Bachelor of Science) |

Publications:

- [1]. J. Ding, X. B. Lu, L. X. Zan, Y. X. Sun, Q. Gao, and Z. L. Wang. Study on chromium-free roughening with manganese dioxide for ABS engineering plastic surface, *Electroplating & Finishing*, 2012, 31, 27-30.
- [2]. L. X. Zan, X. L. Wang, J. Ding, Y. X. Sun, Q. Gao, X. B. Lu, Z. L. Wang. The Effect of 2-Mercaptobenzothiazole on Electro-less Copper Plating, *Electroplating & Finishing*, 2012, 31, 20-23.
- [3]. L. S. Li, X. R. Li, X. B. Lu, Z. L. Wang. A Study of Low Temperature and Low Stress Electro-less Copper Plating Bath, *Int. J. Electrochem. Sci*, 2013, 8, 5191-5202

- [4]. X. B. Lu, L. J. Yao, Z. L. Wang. A Study of Bottom-up Electroplated Copper Filling by the Potential Difference Between Two Rotating Speeds of a Working Electrode, *J. Electroanal. Chem.*, 2014, 712, 25-32.
- [5]. C. Chang, X. B. Lu 2-Mercaptopyridine as a new leveler for bottom-up electroplated copper filling of micro-vias, *Electrochim. Acta*, 2016, 208, 33-38.
- [6]. X. B. Lu, Titanium as substrate for three-dimensional hybrid electrodes for vanadium redox flow battery applications, *ChemElectroChem*, 2020, 7, 737–744.
- [7]. X. Lu, X. Yang, F. Li, M. Tariq, M. Steimecke, J. Li, A. Varga, M. Bron and B. Abel. Plasma-etched functionalized graphene as a metal-free electrode catalyst in solid acid fuel cells. *J. Mat. Chem. A*, 2020, 8, 2445-2452.
- [8]. X. B. Lu, F. Li, M. Tariq and M. Bron. Graphene, Nanocrystal Graphene, and Nitrogen-doped Graphene Hybrid Electrode for Vanadium Redox Flow Battery Application, *RSC Advances*, 2020 (Submitted).
- [9] X. B. Lu, X. Yang, F. Li, H.J. Zhang, J. Li, M. Bron, Synthesis of N-doped Carbon Nanotubes with Abundant Graphitic Nitrogen as an Electrocatalyst for Water Splitting in Alkaline Solution, *J. Mat. Chem. A*, 2020, (Submitted)
- [10] H. J. Zhang, J. M. de S. e Silva, X. B. Lu, C. S. de Oliveira, B. Cui, X. P. Li, C. Lin, S. L. Schweizer, A. W. Maijenburg, M. Bron, R. B. Wehrspohn, Novel stable three-dimensional (3D) stainless steel-based electrodes for efficient water splitting, *Adv. Mater. Interface*, 2019, 6, 1900774.

Patents:

- [1]. X. B. Lu, Z. L. Wang. Electroplating Copper Plating Solution for Bottom-up Filling Microvia Hole: Publication number: CN102995076 A. Application number: CN 201210521115.
- [2]. X. B. Lu, Z. L. Wang. A New Type of Leveler: Publication number: CN103103586 A. Application number: CN 201310056965.
- [3]. X. B. Lu, Z. L. Wang. A New Type of Leveler to Low the Surface: Publication number: CN103103587 A. Application number: CN 201310057889.

Program:

- [1]. National Natural Science Foundation of China. (No. 21273144).
- [2]. Innovation Funds of Graduate Programs, Shaanxi Normal University (No. 2012CXS045).

Abstract

Carbon nanomaterials are inexpensive materials with advantageous electric conductivity that can be produced via various methods from a broad range of carbon sources. Thus, carbon materials can be applied as catalysts or catalyst supports in the development of more efficient processes or in next-generation energy storage devices as catalytic electrode materials, such as fuel cells, flow batteries, and electrocatalytic water splitting devices.

The synthesis and development of sp^2 carbon nanomaterials that are either intrinsically active or have the ability to anchor to a catalytically active carbon component are the aims of this thesis. To achieve these goals, graphene, a two-dimensional honeycomb lattice of sp^2 -bonded carbon atoms, has been synthesized over a Cu foil via the chemical vapour deposition (CVD) method. To improve the electrochemical activity of pristine graphene, metal-free, oxygen-functionalized, and nitrogen-doped graphene for use as an electrode catalyst in solid acid fuel cells (SAFCs) was prepared using O_2 and N_2 plasma treatment in the first part of this thesis.

Following this, Ti, an inert substrate towards the V(IV)/V(V) redox pair in a vanadium redox flow battery (VRFB), was used as a novel substrate combined with graphene, nanocrystalline graphene, nitrogen-doped graphene, and nitrogen-doped carbon nanotubes (NCNTs). Furthermore, the individual electrochemical performance of these hybrid electrodes can be determined due to the sluggish activity of Ti in the abovementioned reaction, which is critical to the basic study of one-dimensional, two-dimensional and three-dimensional carbon materials in VRFBs.

Finally, a highly abundant graphitic nitrogen compound and an extremely active electrocatalyst have been directly synthesized over Ni foam (Ni-F) at a low temperature (600 °C) via CVD. The electrochemical activity of both HER and OER was remarkably improved compared to that of pristine NiF. Moreover, density functional theory (DFT) calculations paired with experimental results were conducted in this thesis to investigate the relevant mechanism, which will guide future endeavours to develop both catalytically active and stable materials for next-generation energy storage and conversion to some extent.

Table of Content

Motivation.....	1
Chapter 1 Introduction.....	5
1.1 Graphene, carbon nanotube, and preparation.....	5
1.2 The growth mechanisms.....	7
1.3 Characterization of graphene.....	8
1.3.1 Crystal structure of graphene.....	8
1.3.2 The basics of Raman spectroscopy.....	9
1.3.3 Phonon dispersion of graphene.....	10
1.3.4 The first order scattering.....	11
1.3.5 The second-order scattering.....	12
1.3.6 The monolayer graphene.....	13
1.4 N-doped graphene.....	15
1.4.1 The Fermi energy and surface.....	15
1.4.2 Analysis of N-doped graphene via XPS and Raman.....	16
1.5 Fuel cell basics.....	18
1.5.1 Types of fuel cells.....	18
1.5.2 Solid acid compounds.....	19
1.5.3 Solid acid fuel cell.....	20
1.5.4 The open circuit voltage of fuel cells.....	21
1.5.5 The overpotential of fuel cells.....	23
1.6 The application of graphene and CNTs.....	25
1.6.1 Application in SAFC.....	25
1.6.2 Application in VRFB.....	26
1.6.3 Application in electrocatalytic water splitting.....	27
1.7 Reference.....	28
Chapter 2 Contribution of Zigzag Carbon and Armchair Carbon Coupled with Functionalized Groups to Oxygen Reduction Activity for Precious Metal Free Solid Acid Fuel Cell.....	42
2.1 Introduction.....	43
2.2 Methods.....	44
2.2.1 Transfer of 1-layer Graphene.....	45
2.2.2 Modification of 1-layer graphene.....	45

2.2.3	Electrochemical half-cell	46
2.2.4	Electrochemical characterization	46
2.2.5	Physical characterization	47
2.2.6	Computational details	47
2.3	Results and Discussion.....	48
2.3.1	Characterisation of monolayer graphene	48
2.3.2	Characterisation of the graphene-based electrode	49
2.3.3	Plasma-etched graphene.....	50
2.3.4	Electrochemical results	53
2.3.5	Mechanism	55
2.4	Conclusions	58
2.5	Reference	59
2.6	Supporting information.....	63
Chapter 3 Novel and High-efficient Three-Dimensional Hybrid Electrodes for Vanadium Redox Flow Battery Applications.....		75
3.1	Introduction	75
3.2	Methods	76
3.2.1	Synthesis of nitrogen-doped carbon nanotubes on the titanium substrate	76
3.2.2	Electrochemical performance	77
3.2.3	Physical characterization	77
3.3	Results and Discussion.....	78
3.3.1	Iron electrodeposition.....	78
3.3.2	NCNT characterisation.....	80
3.3.3	Electrochemical results	84
3.4	Conclusion	87
3.5	Reference	87
Chapter 4 Nanocrystal Graphene, Graphene, and Nitrogen-doped Graphene Hybrid Electrode for Vanadium Redox Flow Battery Applications		91
4.1	Introduction	91
4.2	Methods	92
4.3	Results and Discussion.....	93
4.4	Conclusion	97
4.5	Reference	97
Chapter 5 Synthesis of N-doped Carbon Nanotubes with Abundant Graphitic Nitrogen as an Electrocatalyst for Water Splitting in Alkaline Solution		100

5.1	Introduction	100
5.2	Methods	102
5.2.1	Synthesis of graphene and ultrathin graphite.....	102
5.2.2	Synthesis of NCNTs and N-doped graphite	102
5.2.3	Electrochemical characterization	103
5.2.4	IR correction	103
5.2.5	Calibration of the reference electrode	104
5.2.6	Electrochemically active surface area.....	104
5.2.7	Physical Characterization	104
5.2.8	Computational details	105
5.3	Results and Discussion.....	106
5.3.1	NCNTs Characterization	106
5.3.2	Hydrogen evolution reaction performance	108
5.3.3	Oxygen evolution reaction performance	110
5.3.4	Over water splitting performance	112
5.3.5	Simulation of hydrogen evaluation reaction	113
5.3.6	Simulation of oxygen evaluation reaction.....	116
5.4	Conclusion	118
5.5	Reference	118
5.6	Supporting information.....	124
	Summary and outlook	140

Motivation

The demand for energy is a topic of conversation in every sphere of society [1, 2]. The world is facing an energy crisis and climate warming due to the increase in the world's population and the limited availability of fossil fuels. The worldwide population is expected to grow from 7.2 billion in 2015 to 9.7 billion in 2050. At the same time, energy demand is expected to grow by approximately 1.8% annually [3, 4]. The energy crisis is probably the most important problem to be solved among other offshoot problems [4, 5].

The present primary energy sources are fossil fuel and nuclear energy [6, 7]. The disadvantages of fossil fuels are that these materials are finite and will be exhausted. The emission of the greenhouse gas (GHG) carbon dioxide (CO₂) is also the main reason for global climate warming [8, 9]. For nuclear energy, it is technically impossible to set up a reliable approach to address radioactive waste and build a plant with 100% security. The high risk still remains a challenge [10]. To meet the increasing energy demand and make joint efforts to preserve planet Earth, the only home of human beings, the global GHG emissions must be reduced to achieve zero worldwide carbon emissions by 2050 [3] (Figure M1). The development of alternative renewable and sustainable energy sources and systems with high energy-conversion efficiency is urgently desired.

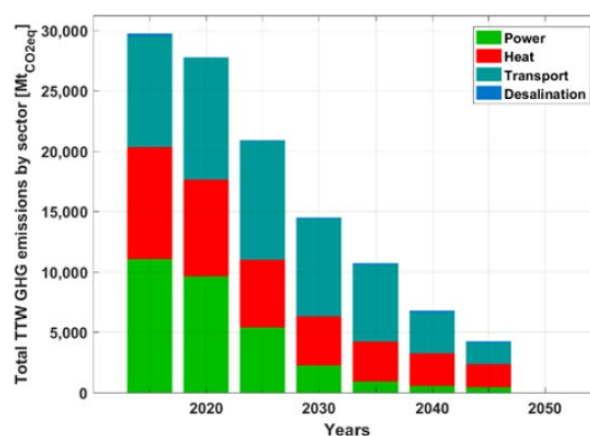


Figure M1. Total GHG emissions during the energy transition from 2015 to 2050 worldwide [3].

Recently, researchers from many fields have focused on renewable energy, e.g., solar photovoltage (PV), wind energy, fuel cells, photoelectrochemical cells, and hydrogen energy [11-14]. One of the most crucial benefits of transitioning to a 100% renewable energy system is the resulting significant reduction in GHG emissions. In addition, a 100% renewable energy system is less expensive than the current global energy system [3]. Figure M2 shows the desirable energy supply in the 100% renewable energy system by 2050. Both solar PV and wind energy will probably dominate in the majority of sources, such as hydrogen, geothermal, and biomass/waste [3, 8].

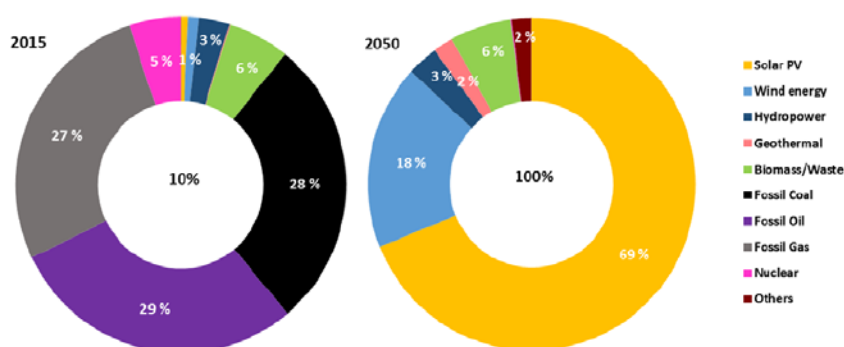


Figure M2. Shares of primary energy supply in 2015 and 2050 [3].

The generation, storage, and conversion of energy by renewable techniques commonly rely on storage devices and materials [15-17] such as electrochemical energy storage devices (batteries and supercapacitors) [18-21] and catalytic materials to achieve clean energy conversion (photo-/electrocatalytic water splitting). An electrochemical device, which is primarily based on the electrochemical redox reaction, can store electricity as chemical energy and can be recharged and reused as a power source. Highly efficient catalytic materials can further facilitate the abovementioned reaction. Accordingly, inexpensive, highly efficient, highly energy efficient and stable materials play an essential role in generating, storing and transporting electricity [11, 22, 23].

Of particular interest is that allotropic forms of carbon (Figure M3) such carbon nanotubes (CNTs), graphene, nitrogen-doped (N-doped) CNTs [24], and N-doped graphene [25] have been widely investigated over the past decade for application in energy generation, storage, and conversion because of their low cost, excellent mechanical properties, good electrical conductivity, and high activity.

In general, the properties of an atom are determined by the arrangement of the electrons in orbitals around the nucleus. The reactivity of atoms is determined by the valence electron configuration since these are the electrons that take part in chemical bonding [26]. Different hybridization states result in different chemical, mechanical, thermal, and electrical properties [4, 26].

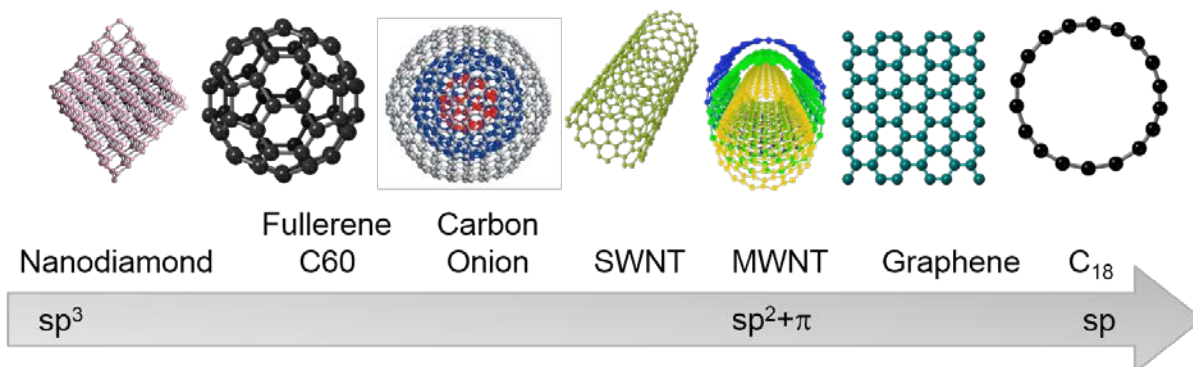


Figure M3. Hybridization states of carbon-based nanomaterials.

For carbon nanomaterials, improving the reactivity by tailoring the doping type and improving the dopant content may be a promising approach. Thus, it will be necessary to further investigate the effect of hybridization states on the activity in redox reactions involved in energy generation, storage, and conversation, such as the hydrogen evolution reaction (HER), the oxygen reduction reaction (ORR), and even the oxygen evolution reaction (OER). First, the dopant content can be improved, as incorporation of a heteroatom often markedly alters the electronic structure, and it has been suggested that heteroatoms may play an important role in promoting the catalytic activity of the HER, OER, and ORR [27, 28]. To obtain doped graphene with a high dopant content, both post-modification and direct synthesis of doped carbon nanomaterials will be studied in this thesis. In addition, the doping type, such as pyridinic nitrogen, pyrrolic nitrogen, graphitic nitrogen (g-N) and adsorbed nitrogen, is the main factor that affects the catalytic activity of N-doped carbon materials. Density functional theory (DFT) calculations show that the g-N possesses the highest activity towards the HER, OER, and ORR [29, 30]. Synthesis of doped carbon nanomaterials with abundant g-N combined with DFT calculations will be for the focus of further study. Thus, this dissertation reviews the state of the art of the relevant fields and proposes

future endeavours for energy conservation and storage, including solid acid fuel cells, vanadium redox flow batteries, and electrocatalytic water splitting devices.

Chapter 1 Introduction

1.1 Graphene, carbon nanotube, and preparation

Graphene, a two-dimensional honeycomb lattice of sp^2 -bonded carbon atoms, has triggered potentially huge interests since its discovery in 2004 [31]. Its extended honeycomb framework creates the essential frame block of separate vital allotropes; it can be stacked to construct 3-D graphite, as shown in Figure 1.1, rolled to form 1-D-nanotubes and wrapped to establish 0-D-fullerenes [32-35]. The sp^2 hybridized C-C bonding with π -electron clouds and very thin atomic thickness (0.345 nm) results in its extraordinary construction, remarkable electrical, thermal and automatic properties [31, 36-38]. The properties, especially its high strength/strain-to-failure^[31], high surface area and chemical stability have found applications in composites, Nano-electronics, energy storage, sensors, catalysis and biomedicine [16, 19, 39, 40]. It can be repeatedly peeled off layers of graphene from the highly oriented pyrolytic graphite (HOPG) via an adhesive tape, which was first reported by the in 2004 [38]. It is possible that obtain monolayer, high-quality graphene through this method. However, it is a challenge that flexibly tailors the number of layers and the size of graphene prepared via this method.

In general, the graphite or diamond can be synthesized by decomposing organic precursors under special conditions, for instance, high temperature and low pressure via chemical vapour deposition (CVD) technology [41]. The formation of graphite usually undergoes two essential procedures, carbonization and graphitization. The precursors can be transferred into carbon material under about 1200 °C [42] in the carbonization step. The graphitization of carbon material from a turbostratic structure to an ordered graphitic structure proceeds a much higher temperature than that of carbonization, about 1800 °C [42]. However, the introduction of metallic catalyst can reduce this temperature, which established the foundation of research in the synthesis of carbon nanotube (CNT) and graphene via CVD method when metal or metal particle serves as catalyst substrate [43, 44].

The introduction of metal accelerates the formation of an ordered graphitic structure. Given that the decomposition of precursor gas and graphitization, a similar process exists in the synthesis of graphene and CNT with CVD approach. Base on this, the synthesis of CNT has been first reported by Iijima via arc discharge process [45].

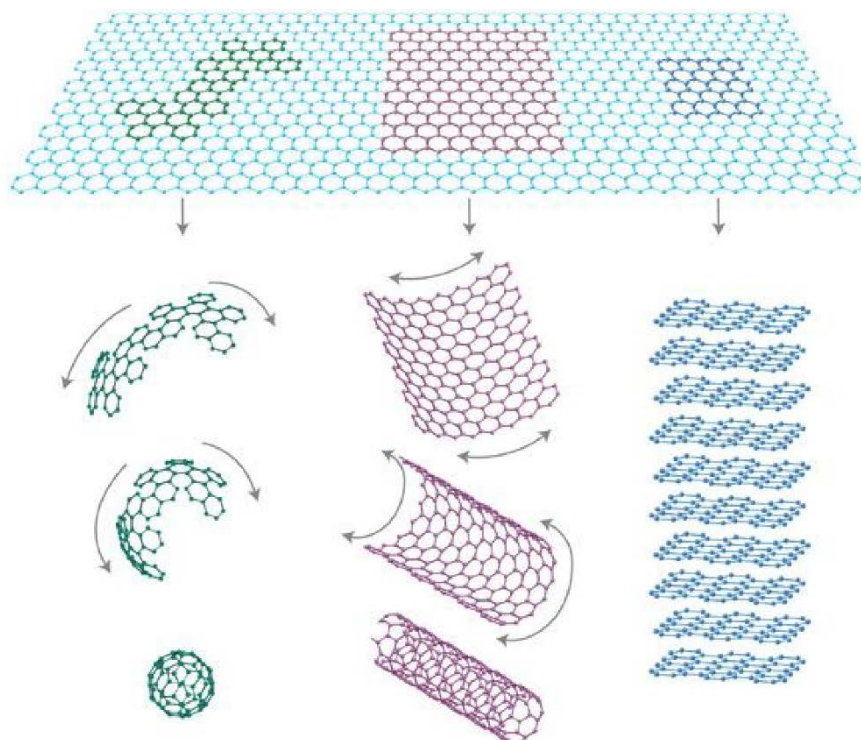


Figure 1. 1. Mother of all graphitic forms. Graphene is a 2D building material for carbon materials of all other dimensionalities. It can be wrapped up into 0D buck balls, rolled into 1D nanotubes or stacked into 3D graphite [35].

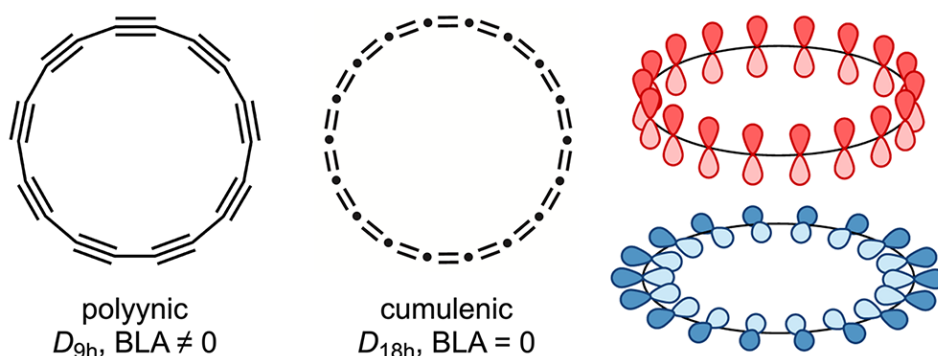


Figure 1. 2. Two possible structures of cyclo[18]carbon. The polyynic form with D_{9h} symmetry and the cumulenic form with D_{18h} symmetry, (BLA = bond length alternation) and visualization of their perpendicular π -systems [46].

Numerous reports on the CNT growth were published in various deposition approaches such as CVD method [47, 48], pyrolysis of hydrocarbon [49], and physical vapour deposition method ect. [50, 51]. The metal particles, e.g. Fe [52], Co [53], and Ni [54] particle, were applied as supporting catalyst to grow CNT via CVD approach. The

diameter of CNT can also be tailored by adjusting the diameter of the catalyst particle. In addition to the CVD approach has also been attracted to numerous researcher's interests throughout the world since Ruoff et al. [36] first reported that the synthesis of graphene on the Cu foil via CVD. Furthermore, the latest report shows that another carbon allotrope, cyclo[18] carbon (C₁₈), was generated by Anderson's group in 2019 [46], as shown in Figure 1.2. To date, the studies in preparing sp³, sp², and sp hybridized carbon nanomaterials have been artificially achieved. Based on previous significant researches, the graphene and CNT were synthesized via the CVD method in this thesis.

1.2 The growth mechanisms

Solid [55, 56], liquid [57], and gaseous [36] carbon sources have been used for graphene synthesis. With the similar decomposition process, the initial active carbon species start to form for the growth of graphene. The decomposition efficiency of any carbon source to some extent decides the subsequent quality, number of layers, and coverage of CVD graphene. Methane, a simple hydrocarbon, is a common precursor gas to contribute graphene. The C–H bond energy is 440 kJ mol⁻¹ in the methane molecule [58, 59], which will be completely decomposed exceeds 1200°C. This high temperature is a great challenge in a typical thermal CVD set-up. The Cu thus are broadly applied to reduce this temperature as a metal catalyst. Due to the strong bond energy (4.48 eV) [60], the high pressure can accelerate the break of the C–H bond. Using the most commonly applied methane as an example when Cu as the catalytic substrate. The carbon species can dissolve into the Cu substrate under high temperature. General reaction mechanism of forming graphene can be described as, 1) Mass transportation of the carbon precursor toward the substrate, 2) The conversion of active carbon species by means of dehydrogenation of carbon precursors, 3) Surface diffusion, 4) initial dimerization, 5) polymerization, 6) aromatization [59, 61-63].

Although the growth mechanism of CNT is still debated, the two common cases have been widely accepted. First, the top-growth model, the growth of CNTs crosses the metal particle bottom and pushes the whole particle off the substrate, which due to that the weak adhesion force between catalyst and substrate [64, 65]. On the contrary,

when exhibits a strong interaction between metal particle and substrate, the growth direction of CNT is compelled along the particle's apex. Hence, the CNT grows up with the particles rooted on its base; this is known as a root-growth model.

1.3 Characterization of graphene

Raman spectroscopy often uses to evaluate the structural properties of sp^2 carbon nanomaterial, e.g. graphene, CNT. Typically, the intensity ratio of the G band at 1580 cm^{-1} and 2-D band at 2680 cm^{-1} (I_G/I_{2D}) is generally considered a qualitative indicator for decreasing defect density in the graphene layer [66, 67], and single layers will depict values that are less than 0.5. The D, G, and 2D bands at ca. 1341 , 1588 , and 2682 cm^{-1} [19, 20] are analyzed, and the intensity ratio of the D to G band (I_D/I_G) is commonly used as an estimate of the quality of NCNTs. Given that the similar sp^2 network, the characterization will focus on the basics of graphene.

1.3.1 Crystal structure of graphene

The unit cell of monolayer graphene involves two carbon atoms, A and B, each contributing a triangular 2D network. However, each displaced from each other by a Carbon-Carbon band of about 0.142 nm [15, 39, 66, 68]. The structure can be seen as a triangular lattice composed of two vectors a_1 , a_2 with a basis of two atoms per unit cell, as shown in Figure 1.3a.

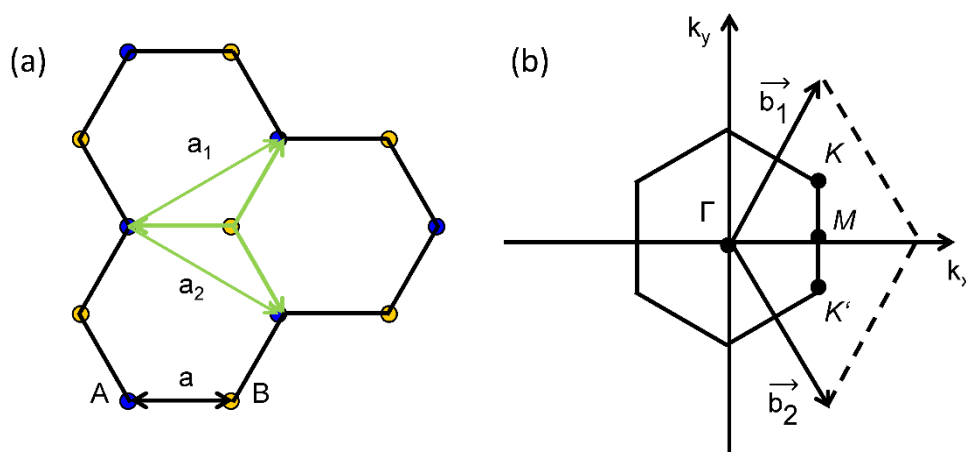


Figure 1. 3. (a) A top view of the real space unit cell of monolayer graphene showing the inequivalent atoms A and B and unit vectors a_1 and a_2 . (b) The reciprocal space unit cell shows the First Brillouin zone with its high symmetry points and lines, such as

Γ connecting to K; connecting to M; Γ was connecting K to M. The two primitive vectors b_1 and b_2 show and the two vectors on the top of the three hexagons show the reciprocal space coordinate axes.

$$a_1 = \frac{a}{2}(3, \sqrt{3}), a_2 = \frac{a}{2}(3, -\sqrt{3})$$

In reciprocal space, the unit cell is planar, as shown in Figure 1.3 b. the unit vectors b_1 and b_2 of the reciprocal lattice given by corresponding to a lattice of length in reciprocal space [69, 70]. The unit vectors b_1 and b_2 of the reciprocal hexagonal lattice are rotated by 30° from the unit vectors a_1 and a_2 in real space, respectively. Figure 1.3 b also shows some high symmetry points of first Brillouin zone: The Γ (Gamma) point at the zone centre, the M points in the middle of the hexagonal sides and the K and K' points at the corners of the hexagons. Other high symmetry points or lines are along ΓK , KM and ΓM . In monolayer graphene, three of the electrons form σ bonds which hybridize in a configuration, and the fourth electron of the carbon atom acquires the orbital which is perpendicular to the graphene plane and makes π covalent bonds. It is of particular importance that the physics of graphene are the two points K and K' at the corners of the graphene Brillouin zone (BZ) [71, 72].

$$b_1 = \frac{2\pi}{3a}(1, \sqrt{3}), b_2 = \frac{2\pi}{3a}(1, -\sqrt{3})$$

1.3.2 The basics of Raman spectroscopy

Raman spectroscopy based on the inelastic scattering, which hints that the energy or frequency of photons in single light changes upon interaction with the sample, the photons of the laser are absorbed by the matters and then re-emitted. The frequency of re-emitted photons is shifted up or down the pristine monochromatic light frequency, which is called the Raman effect [73]. It is potential that the scattered photons of light can either be of higher or lower energy than the incident photons. Figure 1.4 shows that there are three main scattering processes: Rayleigh scattering, Stokes scattering, and Anti-Stokes scattering. Rayleigh scattering without energy transfer, the scattered energy has the same energy as incident energy ($\hbar\omega_i = \hbar\omega_R$), where \hbar is Planck's constant (4.1357×10^{-15}). Raman scattering with energy transfer, if the scattered photon losses energy, it is identified Stokes line ($\hbar\omega_i > \hbar\omega_S$), and if the scattered photon gains energy, it is called Anti-Stokes line ($\hbar\omega_i < \hbar\omega_{aS}$).

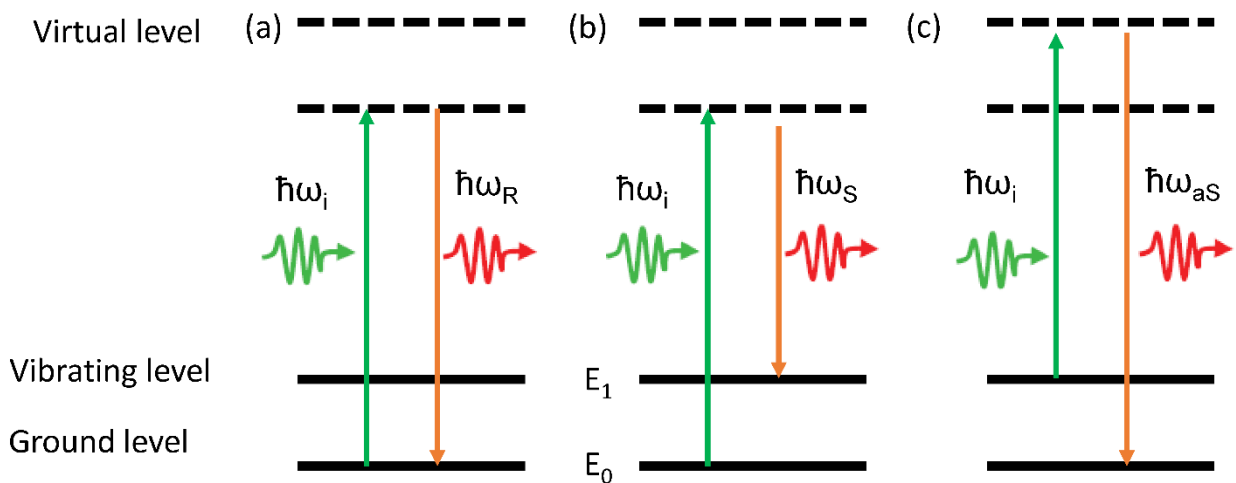


Figure 1. 4. (a) An electron is excited from the ground level and falls to the original ground level. (b) An electron is excited from the ground level and falls to a vibrational level. (c) An electron is excited from a vibrational level and falls to the ground level [72-74].

1.3.3 Phonon dispersion of graphene

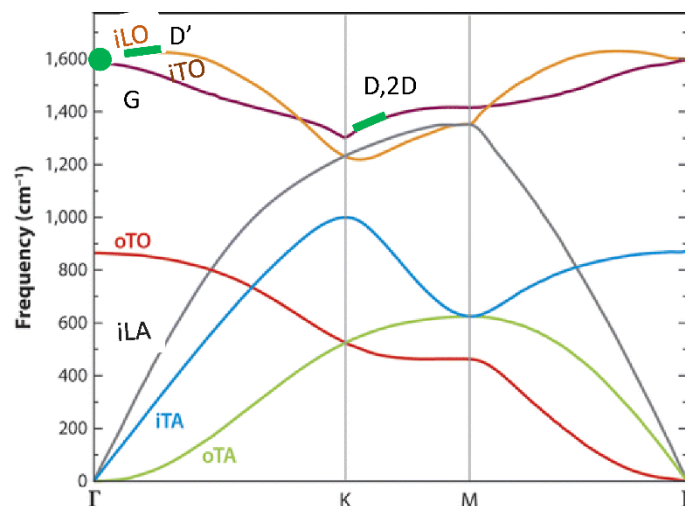


Figure 1. 5. Calculated phonon dispersion relation of graphene showing the iLO, iTO, oTO, iLA, iTA and oTA phonon branches [72].

The Raman-scattering analysis shown in Figure 1.5 is the most impressive and non-destructive approach for interpreting the performance of electrons and phonons in

graphene [32, 33]. A stronger understanding of the phonon dispersion of graphene plays a vital role in interpreting the Raman scattering of graphene. Due to that there are six phonon dispersion bands for the unit cell of 1-LG contains two carbons, A and B. There are acoustic (A), and three are optical (O) phonon modes. For the three acoustic and three optical phonon modes, one is an out-of-plane (oT) phonon mode, and the other two are in-plane modes, one longitudinal (L) and the other one transverse (iTO). Thus, starting from the highest energy at the Γ point in the Brillouin zone the various phonon modes are labelled as iLO, iTO, oTO, iLA, iTA and oTA [73, 75, 76].

This six phonon dispersion band (two being doubly degenerate) at the Brillouin zone centre. There is one degenerate in-plane optical mode, E_{2g} (Figure 1.6a), and one out-of-plane optical mode B_{2g} (Figure 1.6b). The E_{2g} phonons are Raman active [77], whereas the B_{2g} phonon is neither Raman nor infrared active. Atomic vibrations are partially screened by electrons. In a metal this screening can change rapidly as a function of individual points (wave vector q) of the Brillouin zone [78], giving rise to a divergence in the phonon dispersion(q vector) at these special points, which ultimately influenced by the shape of the Fermi surface. The consequent anomalous behaviour of the phonon dispersion is called Kohn anomaly [78, 79].

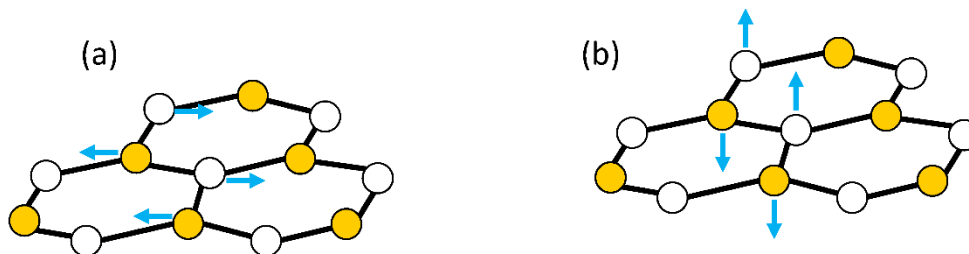


Figure 1. 6. Γ -point phonon-displacement pattern for graphene. Empty and filled circles represent inequivalent carbon atoms. Blue arrows show atom displacements. (a) E_{2g} and (b) B_{2g} [73, 75].

1.3.4 The first order scattering

Figures 1.7a shows the G band is that the bond stretched between pairs of sp^2 carbon atoms which belongs to the E_{2g} irreducible representation, which exists on all sp^2 carbon materials, just like graphene, graphite, amorphous carbon, and carbon nanotubes. The origin and dispersive behaviour in the frequency of G band originate

from the first-order scattering Raman processing. Usually, at the Γ point in the centre of the first Brillouin zone, an electron in the valence band is excited by the incident photon to create a virtual electron-hole pair, the electron or the hole is scattered by either an iTO or an iLO zone-centre phonon (Figure 1.4). Follow then, the electron and hole recombine and emit a photon that shifts to low frequency (1580 cm^{-1}) by the amount of energy given to the phonon. Due to the dispersion electron and hole belong to the same circle around the Γ point, the first-order Raman scattering of G band is also called intervalley process ^[66].

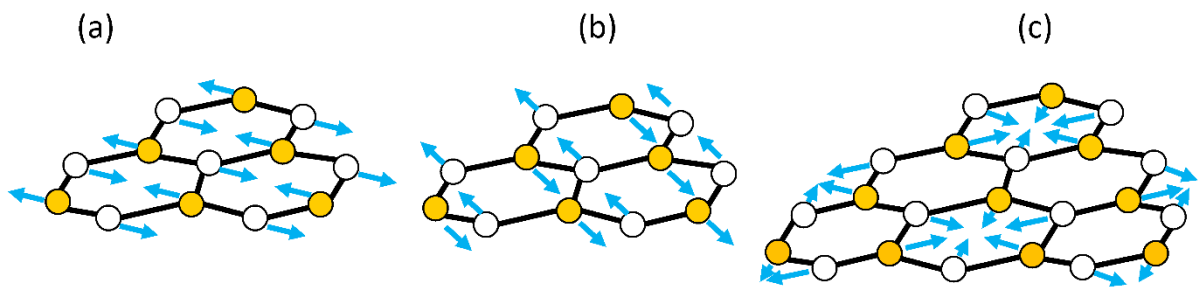


Figure 1. 7. (a) (b) Sketch of the phonon vibrations contributing to the main Raman G band vibration mode for the iTO and iLO phonons at the Γ point in graphene. (c) Sketch of the phonon vibrations contributing to the main Raman D and 2D (G') band vibration modes for the iTO K point in graphene ^[33, 75, 79].

1.3.5 The second-order scattering

Both D (1350 cm^{-1}) and 2D or G' (2680 cm^{-1}) band are associated with the second-order Raman scattering process originating from the in-plane breathing-like mode of the carbon rings, as shown in Figures 1.7 b and c. The second-order Raman scattering process is also called double-resonance process because the incident or scattered photon and the first or second phonon scattering are resonant with electronic levels in the graphene ^[71, 80].

For the D band, an electron-hole pair is excited by the incident phonon; one electron is elastically scattered by an iTO phonon to the K' point and then is inelastically scattered back to the K point before recombining with the hole, as shown in Figure 1.8. The Raman process must conserve energy and momentum, and the defect plays a role in conserving momentum during these events. Therefore, the defect could be any

breaking of the symmetry of the graphene lattice, e.g. armchair edge or zigzag edge, grain boundary, sp^3 defect etc. [71, 81]. Due to that the D is approximately half of that the G' -band frequency, the G' -band is also called 2D-band, which is the strongest peak in single layer graphene [33, 82]. Figure 1.8 also shows that the double-resonance process of the 2D band, one electron is inelastically scattered by iTO phonon to the K' point and then is inelastically scattered back by the iTO to the K point. The electron and hole then recombine and emit a phonon. Instead of an intervalley process, this double-resonance is called an intervalley process because it connects points in circles around inequivalent K and K' points in the first Brillouin zone of graphene [83].

D' band ($\sim 1620\text{ cm}^{-1}$) usually occurs by a defect of graphene, which also belongs to an intra-valley process as a result of two points contributing to the same circle around the K or K' point.

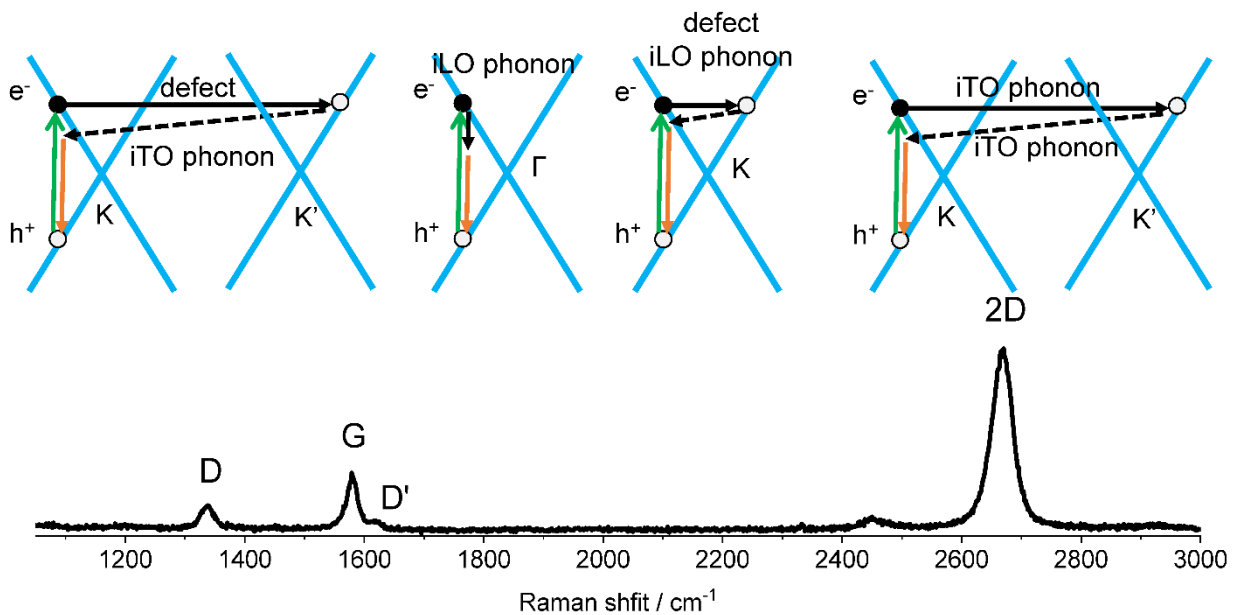


Figure 1. 8. Typical Raman spectrum of defect-containing graphene measured with a 523 nm laser. CVD-grown graphene sample for Raman measurement was transferred on a SiO_2 (600 nm)/Si substrate. Illustrations of the first-order Raman scattering process of G band and second-order Raman scattering processes of D, D' , G' band in graphene are shown together [32, 37, 66, 80].

1.3.6 The monolayer graphene

The high intensity of the 2D band at about 2680cm^{-1} is the obvious character of the monolayer graphene. In order to know why the 2D model is higher than the G model, at this point, it is necessary to make some general definitions. The original state electron of wave-vector k around K , the electron is scattered by a phonon or a defect of wave-vectors q and $-q$, (negative symbol standards for inverse direction) and an intermediate state of the electron, $k+q$ [66, 80, 84] (Figure 1.9).

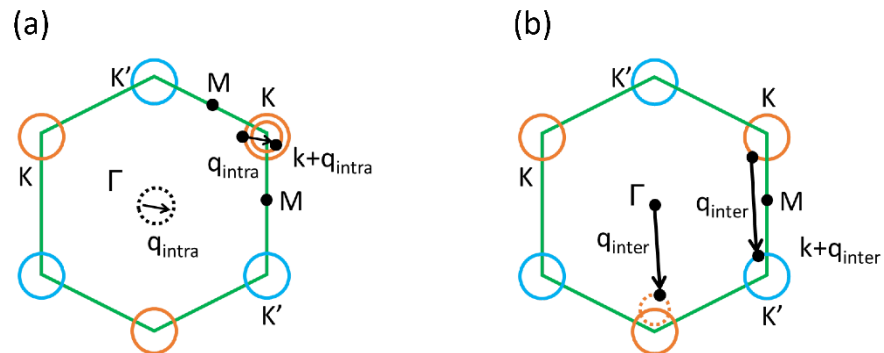


Figure 1. 9. (a) A top view of an intra-valley and (b) an inter-valley scattering from a given k vector at the K , Γ point and $k+q$ along the high symmetry ΓK and KK' direction [85].

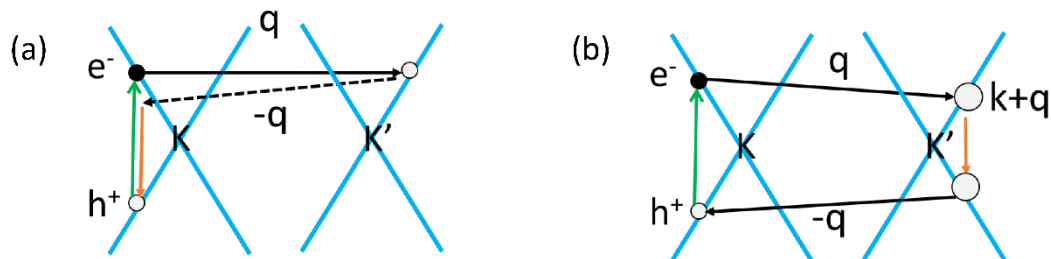


Figure 1. 10. Resonant processes of dispersive Raman modes in monolayer graphene, a) double resonance b) Triple resonance [66, 75, 86].

The second-order Raman scattering process, the electron is excited at k , and then inelastically scattered to the $k+q$ around K' , where the K' point is related to K by time-reversal symmetry. The electron is scattered back to the pristine state k , and recombines with a hole at K , as shown in Figure 1.10a. However, for the monolayer graphene, the valance band, and conduction band is almost mirror band of one another with respect to the Fermi energy. Meanwhile, the hole can scatter the electron. In this case, the hole will be scattered by the q but not to scatter back with wave-vector

–q. It leads to an important effect that both the electron and hole scattering processes will be resonant, which also is name Triple resonance process, which possibly can explain why the 2D band is more intense than the G band in monolayer graphene (Figure 1.10b).

1.4 N-doped graphene

Graphene, a two-dimensional honeycomb lattice of sp^2 -bonded carbon atoms, has triggered potentially huge interests for energy storage and conversion to generally favourable toward its unique structure and porosity. Direct synthesizing, post-treating and even cooperation with transition metal are effective approaches to improve chemical reactivity. Nitrogen elements possess stronger Lewis basicity to affect the electronic structure of carbon to improve the catalytic performance [37, 74, 87]. Therefore, synthesis of the doping sp^2 carbon nanomaterials has been played a significant role in enhancing its catalytic performance and alternating its electronic structure.

1.4.1 The Fermi energy and surface

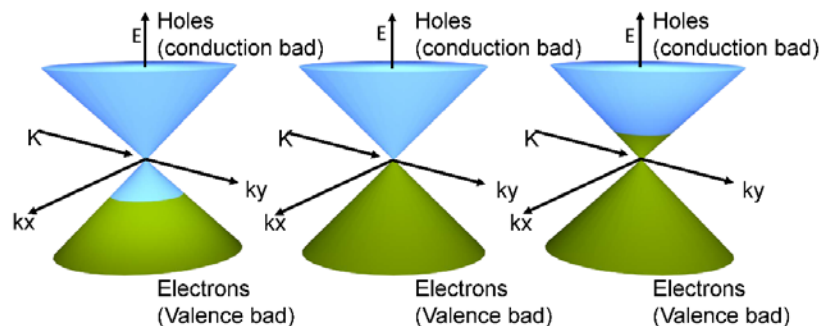


Figure 1. 11. A blow-up of the energy dispersion relation for graphene around the Dirac point (K) in the Brillouin zone. Green indicates levels filled with electrons while blue indicates empty levels (holes). Left shows that electrons are partially drained from the valence band (hole-doped graphene with the Fermi level displaced to a position below the Dirac point). The middle represents neutral graphene where the valence band (π bonding states) is completely filled with electrons, and the conduction band (π^* anti-bonding states) is completely empty. The right represents that electrons are forced into the conduction band (negatively doped graphene where the Fermi level is consequently above the Dirac point). [31, 88, 89]

Figure 1.11 shows that the Fermi energy is an energy of the highest occupied state. However, the Fermi surface is the surface of constant energy E_f in k space (it is a dual space after Fourier transform, usually used in magnetic resonance imaging). The Fermi surface separates the unfilled orbitals from the filled orbitals at absolute zero. The electrical properties of the metal are determined by the volume and shape of the Fermi surface because the current is due to change in the occupancy of states near the Fermi surface [68, 89, 90].

1.4.2 Analysis of N-doped graphene via XPS and Raman

The N-doped graphene contains respectively pyridinic nitrogen, pyrrolic nitrogen, graphitic nitrogen and adsorbed nitrogen at 398.7 eV, 400.1 eV, 402.0 eV and 405.0 eV [91, 92] by the analysis of XPS (Figure 1.12). Due to both the pyrrolic nitrogen and pyridinic nitrogen belong to p-type doped graphene, the hole in the graphene could result in that the Fermi level is more below than the Dirac point. In contrast, the n-typed doped graphene possesses remain electron [75, 93]. The remaining electron will release into the conduction band, and the Fermi level will move above the Dirac point [90, 94].

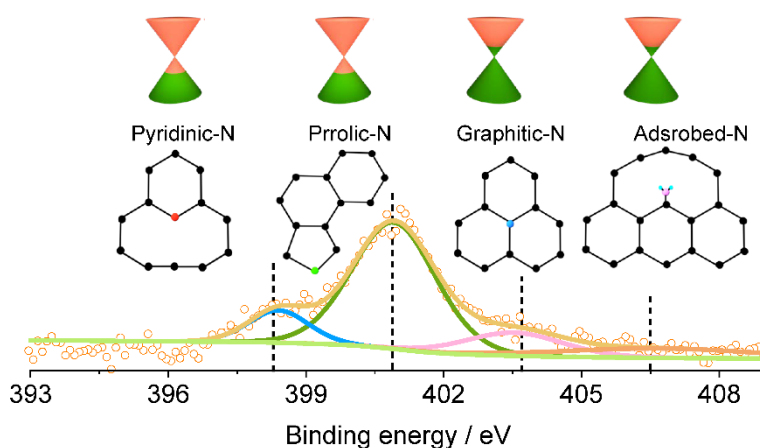


Figure 1. 12. XPS spectra of N1s and schematic presentation of the Fermi surfaces move with various type of doped graphene [87].

The literature review shows that the interaction between the extra electron from quantum dots and the phonon from graphene leads to the width of G-band become large or less with respect to the pristine graphene. The resistance of the p-type doped graphene is larger than n-type doped graphene regarding the raw graphene [95, 96]. The

graphene is treated with nitrogen plasma in our study, which belongs to electrically doped graphene. Because of nitrogen elements can take place the carbon elements in graphene grid, The G and 2D bands tend to upshift for both p-type doped graphene and n-type doped graphene [33, 77, 83]. In Figure 1.13, the shift in G and 2D peaks of N-doped graphene are respectively about 10 cm^{-1} and 9 cm^{-1} , corresponding to the pristine graphene. On the contrary, the G-band of n-type doped graphene tends to downshift while the G-band of p-type doped graphene upshifts when the graphene is doped by the surface transferring [36].

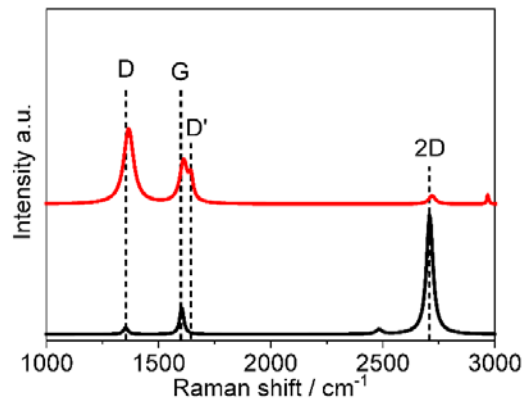


Figure 1. 13. The Raman shift of G and 2D bands compared with pristine graphene.

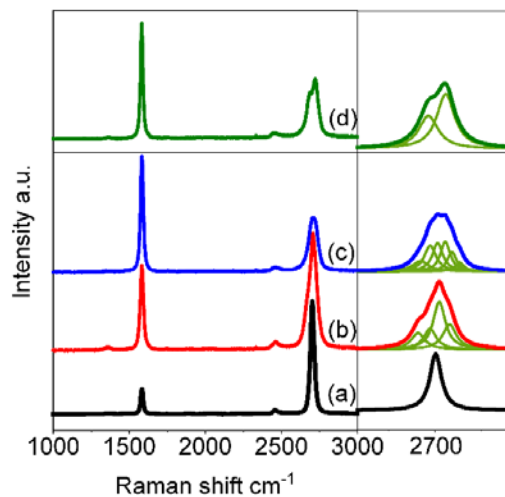


Figure 1. 14. The measured 2D Raman band with 532 nm laser energy for (a) 1-LG, (b) 2-LG, (c) 3-LG, and (d) Ultrathin graphite. The splitting of the 2D Raman band opens up in going from mono- to three-layer graphene and then closes up in going ultrathin graphite.

The number of the graphene layer is another main reason that both G and 2D bands tend to upshift in Raman spectra. Meanwhile, the intensity of 2D band reduces with the number of layers increase because of the relaxation of the DR Raman selection rules associated with the random orientation of the graphene layers with respect to each other [66, 81]. Figure 1.14 shows that the number of layers slightly increase with growth time extend. For the monolayer graphene, the 2D band contains one single Lorentzian peak with an FWHM of 24 cm^{-1} [66, 97]. When the graphene layers arrived at a level of few-layer or ultrathin graphite, broaden 2D band [72, 94] instead of single Lorentzian peak.

1.5 Fuel cell basics

1.5.1 Types of fuel cells

There are two fundamental technical challenges with fuel cell. First, the sluggish reaction rate resulting in low currents as well as power. In addition to that, hydrogen (H_2) is not a readily available fuel. To address these problems, numerous various fuel cell types have been developed. Typically, there are five classes of fuel cell have emerged as viable systems for the present and near future, which are distinguished by the electrolyte that is applied [98, 99].

The proton exchange membrane fuel cell (PEMFC) is one of the simplest fuel cells, which due to that the electrolyte is a solid polymer and immobile. The PEMFC possess rapid thermal cycling at a low temperature ($30\text{--}100 \text{ }^\circ\text{C}$). However, in order to maintain a high cell voltage under large current loads, it requires that the application of expensive catalysts such as platinum (Pt). Besides, the quite pure H_2 supply restricts the wide application of PEMFC [100, 101].

The (AFC) was developed and used because alkaline fuel cell has also operated at a lower temperature ($50\text{--}200 \text{ }^\circ\text{C}$). The disadvantage is that a high amount of Pt was loaded to overcome the slow reaction rate. Given that the carbon dioxide (CO_2) will react with the alkaline electrolyte, the fuel supplies, oxygen (O_2) and H_2 must be free from CO_2 [102].

The operating temperature of the phosphoric acid fuel cell (PAFC) is about 150–220 °C, so it is also called medium-temperature fuel cell. Both the reaction kinetics and thermal cycling remain for the medium-temperature fuel cell. The reaction rate has been improved by introducing porous electrodes, Pt catalysts, and fairly high temperature. Furthermore, The PAFC could provide an extraordinarily, reliable and maintenance-free power system. The fuels can be settled by reforming natural gas (e.g. methane) to H₂ and CO₂, which could be another challenge for the cost, complexity, and size of the fuel cell system^[103, 104].

The molten carbonate fuel cell (MCFC) ^[105] and solid oxide fuel cell (SOFC) ^[106, 107] are typically high-temperature fuel cells. At high temperature, the efficiency of reaction kinetics at the electrodes are dramatically improved. However, the compatibility of the components will be the main challenge. For instance, a large amount of extra equipment needed to maintain the full fuel cell system and the complex cooling system.

Consequently, the challenge to the fuel cells will tend to develop electrolyte and electrode materials with satisfactory ionic conductivities and electrocatalytic activities at lower temperatures ^[107].

1.5.2 Solid acid compounds

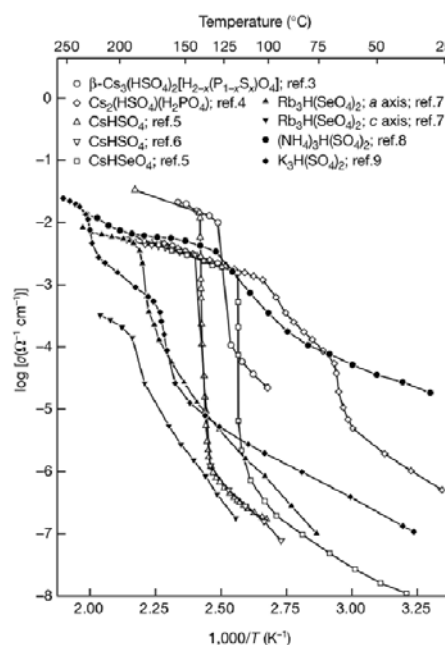


Figure 1. 15. Arrhenius plot of proton conductivity, σ_H , of a few solid acid compounds that exhibit a superprotonic phase transition ^[106].

Solid acid compounds, CsHSeO_4 [108], CsHSO_4 [106, 108], $\text{Cs}_3\text{H}(\text{SeO}_4)_2$ [109], $\text{Rb}_3\text{H}(\text{SeO}_4)_2$ [109], CsH_2PO_4 [98, 110], $(\text{NH}_4)_3\text{H}(\text{SO}_4)$ [111], have been widely studied because of superprotonic phase transition. The phase-transition behaviour results in the conductivity jump by several orders of magnitude to 10^{-2} S/cm [98, 106]. Figure 1.15 shows that the proton conductivity σ_{H} as a function of temperature for several solid acids.

1.5.3 Solid acid fuel cell

The proton conduction in oxyanion solid acids stops relying on the migration of hydronium ions compared with the PEMFCs [112]. Hence, this will simplify the requirement for humidification of the electrolyte. Figure 1.16 shows that the Arrhenius behaviour of CsH_2PO_4 proton conductivity, which due to the superprotonic transition from a low symmetry monoclinic phase to a high symmetry cubic phase [112, 113], as shown in Figure 1.17.

CsH_2PO_4 is the most viable solid acid fuel cell (SAFC) electrolyte, has been received wide attention as the electrolytes in the next generation fuel cell. As the solid acid proton conductors, it possesses a high proton conductivity of 2.2×10^{-2} S/cm at 240°C [98], which belongs to the moderate temperature fuel cell.

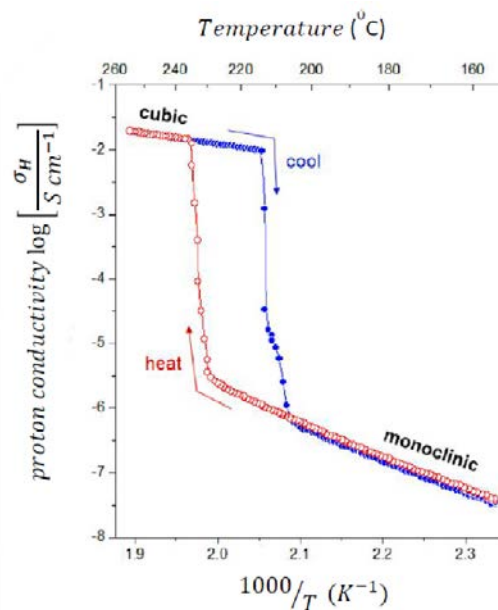


Figure 1. 16. Arrhenius plot of proton conductivity (σ) of Super-protonic phase transition in CsH_2PO_4 in humidified N_2 [112].

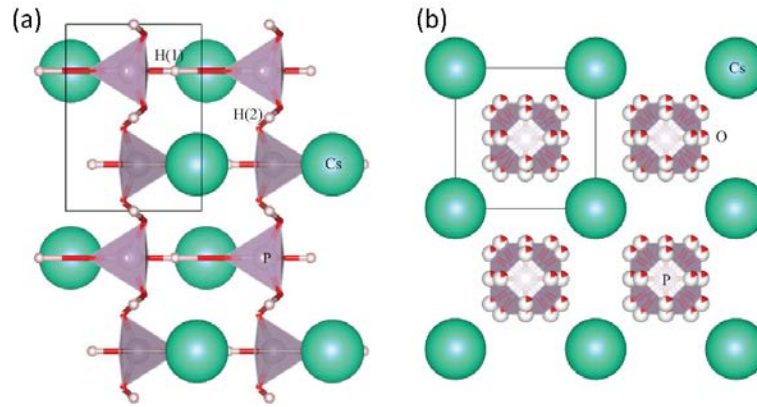


Figure 1. 17. Crystal structures of CsH_2PO_4 in (a) the monoclinic paraelectric phase with space group $P2_1/m$, and (b) the cubic superprotonic phase with space group $Pm\bar{3}m$ [113].

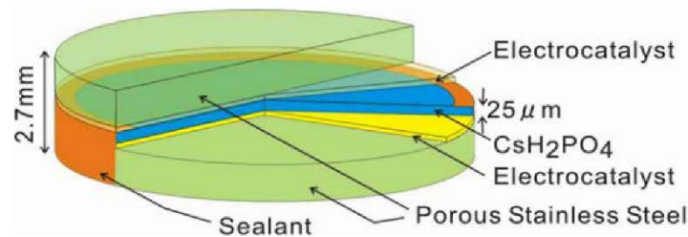


Figure 1. 18. Schematic diagram of a fabricated cell [114, 115]

SAFC is also characterized by lowest permeability to fuels of the electrolyte, high electrocatalytic conductivity and lower catalyst poisoning at a moderate temperature about 228 °C. Uda et al. obtained peak power density of 305 mW cm^{-2} and 415 mW cm^{-2} with 25 μm CsH_2PO_4 electrolyte when fuel is methanol, ethanol and hydrogen, respectively [98, 114]. This funding could be a promising transfer of SAFC from laboratory curiosities into highly competitive energy conversion devices. Figure 1.18 shows that the sandwich-like cell configuration [114].

Figure 1. 18. Schematic diagram of a fabricated cell [114]

1.5.4 The open circuit voltage of fuel cells

Fuel cells are electrochemical devices that combine hydrogen fuel (but also others like methanol) with oxygen to convert chemical energy into electricity [99, 106]. The fuel cell is similar to a combustion engine that intakes fuel continuously without a need to

recharge. The fuel cell is also like a battery in that an electrochemical reaction occurs as long as fuel is available. In general, a fuel cell is composed of electrodes (anode electrode and cathode electrode) and electrolyte. At the anode, hydrogen is electrochemically oxidized to protons and electrons. Oxygen is electrochemically reduced to form water at the cathode [98, 99]. A simple schematic of a fuel cell based on proton-conducting electrolyte in Figure 1.19. The driving force for the conversion of energy is the Gibbs free energy of the reaction. The half-cell reactions for a proton-conducting electrolyte are:

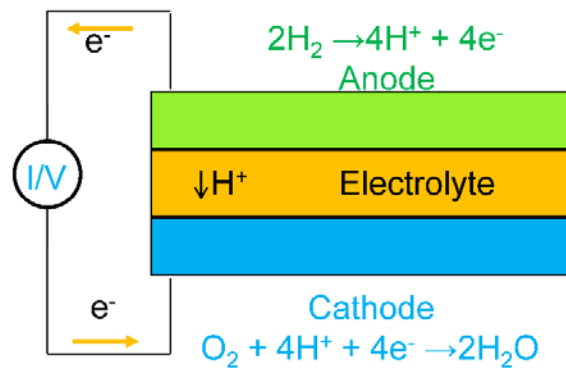
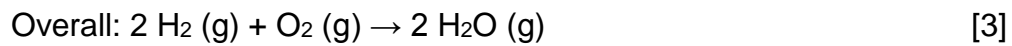
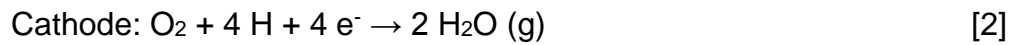


Figure 1. 19. A simple schematic of a fuel cell based on a proton-conducting electrolyte membrane [98, 116].

The open circuit voltage (OCV) of the fuel cell can derive from the Gibbs free energy of the reaction 3 for the case when all species are in their standard states (1 atm, pure gases). It can be related to the electrochemical voltage as follow.

$$\Delta G^0(T) = -nFE^0(T) \quad [1]$$

Where E^0 is the Nernstian voltage of the fuel cell, n is the number of electrons transferred, ΔG^0 (Temperature = 298K) = -237 kJ/mol, and F is Faraday's constant (96.485 C mol⁻¹). From equation 1, $E^0 = 1.25 \text{ V}$ ($n = 4$ in this case).

To compute the Nernst potential at more realistic conditions, one can readily show that:

$$E_{eq}(T) = E^0(T) - \frac{RT}{nF} \ln \frac{p_{H_2O}^{2(c)}}{p_{H_2}^{2(a)} p_{O_2}^{(c)}} \quad [2]$$

Where E_{eq} is the equilibrium or theoretical Nernst potential, p_i is the partial pressure of species i at the anode (a) or cathode (c). Values for $\Delta G^0(T)$ can be computed from the formation energies for the reactants and products.

1.5.5 The overpotential of fuel cells

The key performance measure of a fuel cell is that maintain a high cell voltage under large current loads. However, when a fuel cell is made and put to use, the operation voltage is less than expected or Nernstian voltage. Due to the irreversible losses as the current is drawn from the cell. The overpotential η is defined as the drop in voltage from equilibrium to drive a particular process. The measured voltage, E , can be written as [98, 114]:

$$E = E_{eq} - \eta_{leaks} - \eta_{act} - \eta_{iR} - \eta_{diff} \quad [3]$$

Where E_{eq} is Nernstian voltage, η_{leaks} is the voltage loss due to gas leaks across the electrolyte or partial electronic conductivity of the electrolyte. η_{act} is activation overpotential caused by the slowness of the reactions taking place on the surface of the electrodes. A proportion of the voltage generated is lost in driving the chemical reaction that transfers the electrons to or from the electrode. The η_{act} can be given via the relation [98]

$$\eta_{act} = \frac{RT}{2\alpha F} \ln \frac{i}{i_0} \quad [4]$$

Where α is called the charge transfer coefficient, i_0 is the exchange current density. η_{iR} is overpotential due to Ohmic resistances in the cell such as the electrical resistance of the electrodes, mostly from ion transport through the electrolyte, and is characterized by a linear regime in the polarization curve. Mass transport drop, η_{diff} ,

at high current as a result of the depletion of reactants at the electrodes faster than they can be supplied. η_{iR} can be calculated as:

$$\eta_{iR} = jR = j \frac{L}{\sigma} \quad [5]$$

Where L is the electrolyte thickness, σ is the proton conductivity, and j is the current density. Therefore, Ohmic losses can be minimized by fabricating electrodes that are as thin as possible and preventing leakage.

Figure 1. 20 shows that the largest source of overpotential loss is as a result of slow kinetics at the electrodes (η_{act}). η_{leaks} can be minimized by proper sealing of the electrodes and selecting an electrolyte that is a pure ion conductor with high density and low porosity.

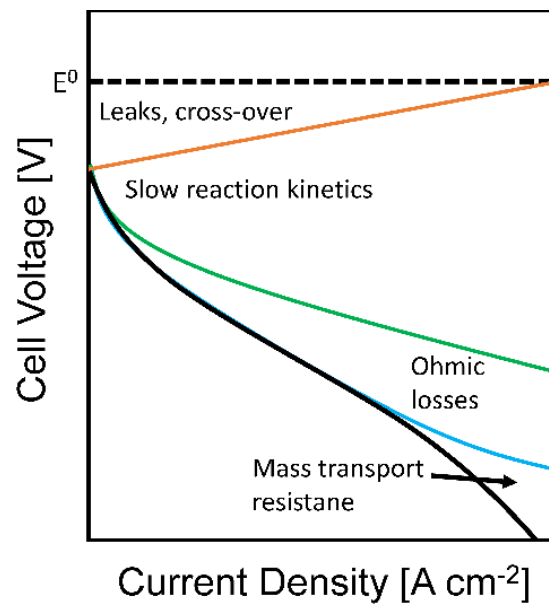


Figure 1. 20. Schematic of a fuel cell voltage vs current density [98].

It is obvious that to minimize η_{act} and improve electrode activity according to equation 4, larger values of charge transfer coefficient (α) and exchange current density (i_0) are desirable. The value of α primarily dependent on inherent material properties. To improve the value of i_0 , the number of active sites per electrode area can be increased, or the intrinsic activity of the electrode modified. Therefore, to lower the value of η_{act} , electrodes not only be catalytically active, but also transport participating electrons and

ions to and from active sites, and have sufficient porosity to minimize value of η_{diff} . It is impossible that one material meets all of these requirements in general. It is the most reason that a porous composite of electrolyte and catalyst particles as the electrode is synthesized.

1.6 The application of graphene and CNTs

Carbon-based materials widely served as costless and stable electrode materials in energy conversion and storage technology, such as fuel cell [116-118], electro/photocatalytic water splitting [119-122], and all-vanadium redox flow batteries (VRFB) [123, 124], have been attracted attention in recent years. This attention stems from the possibilities to tailor the electronic and structural features of graphene and CNTs by introducing surface functional groups (C–OOH, C=O, C–OH) and heteroatoms (nitrogen, boron, sulfur) in pristine graphene and CNTs. There have been great progress and researches in the development of various hybrid materials, post-modifications [125, 126], and enhancement of properties [127-129]. These findings will be a promising approach to developing a non-precious metal catalyst for the next generation energy conversion and storage technology.

1.6.1 Application in SAFC

Graphene is considered as one of the most versatile and promising materials for a wide range of technological applications. Recently, various graphene-like materials, e.g. flakes [130, 131], bundles [132, 133], reduced graphene oxide (RedGo) [134, 135], etc., have been demonstrated as catalytically active components in electrochemical cells, promoting electrode reactions. Multiple groups have published novel synthesis routes to obtain doped or functionalized carbon nanotubes (CNTs) and graphene with remarkable catalytic activity suggesting the possibility of even replacing precious metal catalysts [136-138]. However, the information of pristine graphene as the working electrode is still not completely studied in SAFC. In addition, dopants such as nitrogen, sulfur, boron or surface functional groups such as C=O, C–OH, and C–OOH groups alter the electronic structure of the carbon materials significantly and as such may play a significant role promoting electrochemical reactions in their vicinity. Therefore, it will be significant for filling in a gap in the research of SAFC combined with pristine graphene.

1.6.2 Application in VRFB

The vanadium redox flow battery (VRFB) is applied extensively in large-scale electrochemical energy storage systems since its chemistry is entirely based on vanadium ions at different valence states, and thus are free from cross-contamination problems [139, 140]. An entire battery system of VRFB was first successfully performed at the University of New South Wales by Maria Skyllas-Kazacos in the 1980s [139]. In VRFB, the energy is stored in two solutions using redox pair of dissolved species, and the respective redox species are the $\text{VO}^{2+}/\text{VO}_2^+$ and $\text{V}^{2+}/\text{V}^{3+}$ redox couples in the positive and negative electrolyte solution [139, 141], respectively. A proton-exchange membrane separates the positive and negative compartment, preventing cross-mixing of the two electrolyte solutions [142]. Figure 1.21 shows the schematic of a VRFB.

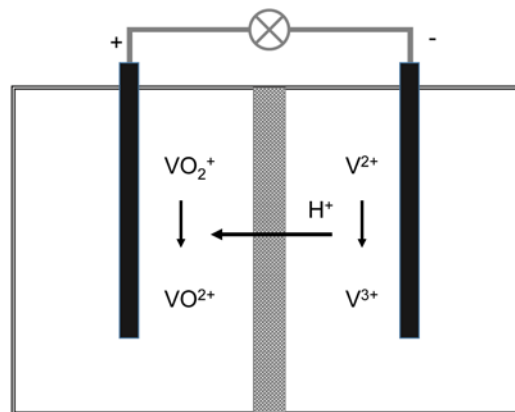
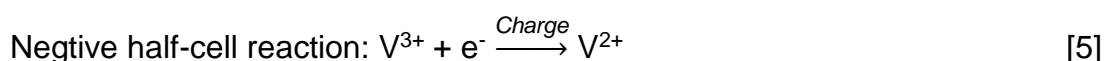
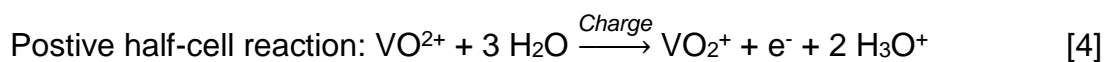


Figure 1. 21. Simple schematic of an all-vanadium redox flow battery.

The positive and negative electrochemical reactions are given by reactions 4 and 5, respectively, while reaction 6 described the net reaction [123, 139, 143].



$$\text{Cell voltage (pH = 0): } E = \phi_{\text{neg}} - \phi_{\text{pos}} = -0.26 \text{ V} - 1.00 \text{ V} = -1.26 \text{ V}$$

The redox reactions of both $\text{VO}^{2+}/\text{VO}_2^+$ and $\text{V}^{2+}/\text{V}^{3+}$ typically occur at the electrodes. Thus, the electrode materials play an important role in facilitating the relevant reactions

in VRFB. Numerous carbon materials, such as graphite felts ^[144], carbon nanotubes ^[124] mesoporous carbon ^[123], and nitrogen-doped carbon nanotubes ^[145] have been used as catalytically active ingredients in VRFB. Given that the presence of strongly acidic electrolytes excludes the application of less expensive materials, the electrochemical activity of individual graphene and CNT have rarely been appropriately evaluated to date. Thus, it is interesting to evaluate a combination of graphene or CNTs with high-stable Ti substrate as a novel hybrid electrode for VRFB. Moreover, the electrochemical performance of isolated sp² carbon nanomaterial can be identified.

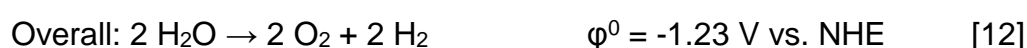
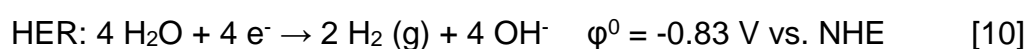
1.6.3 Application in electrocatalytic water splitting

Clean and renewable energy-driven water splitting to produce hydrogen and oxygen has been commonly evaluated as a promising solution to the global energy crisis and demand problem ^[146, 147]. The water splitting reaction consists of two half-reactions, namely the HER and OER, both of which suffered from sluggish kinetics. According to the medium that is used, two different reaction processes have been widely accepted. These can be briefly described as follows ^[148, 149]:

When an acidic medium is present:



When an alkaline medium is present



As the state-of-the-art catalysts for water electrolysis, precious-metal-group materials (e.g., platinum and noble metal oxides) play an important role in boosting the slow

kinetics of HER and OER (e.g., Pt for HER [150, 151], RuO₂ for OER [152]), while their large-scale application is severely restricted by their high cost and accessibility [153-156]. Metal foams have highly porous, possess low thermal conductivity and are rich, high-strength and ultra-light materials. It has been attracted extensive attention in the last few years [157-159], especially nickel foam, which has been demonstrated to be an inexpensive and alternative material served as low over-potential and inexpensive [150, 160, 161]. Furthermore, carbon-based materials such as graphene [158], N-doped graphene [25], carbon nanotubes (CNTs) [24], and N-doped CNTs (NCNTs) [162] have been extensively investigated owing to their low cost, excellent mechanical properties, good electrical conductance and primarily high activity towards. However, the utmost electrochemical performance of Ni foam combined graphene, graphite, N-doped graphene, and N-doped CNTs remains unknown. Hence, the probably utmost electrochemical performance of Ni foam combined with sp² carbon materials was studied in this thesis.

1.7 Reference

- [1] L.S. Roselin, R.S. Juang, C.T. Hsieh, S. Sagadevan, A. Umar, R. Selvin, H.H. Hegazy, Recent Advances and Perspectives of Carbon-Based Nanostructures as Anode Materials for Li-ion Batteries, *Materials*, 12 (2019) 1229.
- [2] J. Liu, Q. Ma, Z. Huang, G. Liu, H. Zhang, Recent Progress in Graphene-Based Noble-Metal Nanocomposites for Electrocatalytic Applications, *Adv. Mater.*, 31 (2019) e1800696.
- [3] M. Ram, D. Bogdanov, A. Aghahosseini, A. Gulagi, A.S. Oyewo, M. Child, U. Caldera, K. Sadovskaia, J. Farfan, L. Barbosa, M. Fasihi, S. Khalili, B. Dalheimer, G. Gruber, T. Traber, F.D. Caluwe, H.J. Fell, C. Breyer, Global Energy System based on 100% Renewable Energy – Power, Heat, Transport and Desalination Sectors. Study by Lappeenranta University of Technology and Energy Watch Group, Lappeenranta, Berlin, March 2019.
- [4] M. Notarianni, J. Liu, K. Vernon, N. Motta, Synthesis and applications of carbon nanomaterials for energy generation and storage, *Beilstein J. Nanotechnol.*, 7 (2016) 149-196.
- [5] R.E. Smalley, Future Global Energy Prosperity: The Terawatt Challenge, *MRS Bulletin*, 30 (2011) 412-417.

- [6] BP Statistical Review of World Energy, in: B.S.R.o.W. Energy (Ed.), 2018.
- [7] M.S. Mauter, M. Elimelech, Environmental Applications of Carbon-Based Nanomaterials, *Environ. Sci. Technol.*, 42 (2008) 5843-5859.
- [8] J.G.J. Olivier, K.M. Schure, J.A.H.W. Peters, Trends in global CO₂ and total greenhouse gas emissions, PBL Netherlands Environmental Assessment Agency, The Hague, 2017.
- [9] J. Malmodin, D. Lundén, The Energy and Carbon Footprint of the Global ICT and E&M Sectors 2010–2015, *Sustainability*, 10 (2018).
- [10] J.-E. Yang, Fukushima Dai-Ichi Accident: Lessons Learned and Future Actions from the Risk Perspectives, *Nucl. Eng. Technol.*, 46 (2014) 27-38.
- [11] A.M. Abdalla, S. Hossain, A.T. Azad, P.M.I. Petra, F. Begum, S.G. Eriksson, A.K. Azad, Nanomaterials for solid oxide fuel cells: A review, *Renew. Sust. Energ. Rev.*, 82 (2018) 353-368.
- [12] I. Roger, M.A. Shipman, M.D. Symes, Earth-abundant catalysts for electrochemical and photoelectrochemical water splitting, *Nat. Rev. Chem.*, 1 (2017) 1-14.
- [13] S. Das, J.A. Robinson, M. Dubey, H. Terrones, M. Terrones, Beyond Graphene: Progress in Novel Two-Dimensional Materials and van der Waals Solids, *Annu. Rev. Mater. Res.*, 45 (2015) 1-27.
- [14] E.C. Garnett, M.L. Brongersma, Y. Cui, M.D. McGehee, Nanowire Solar Cells, *Annu. Rev. Mater. Res.*, 41 (2011) 269-295.
- [15] M.J. Allen, V.C. Tung, R.B. Kaner, Honeycomb Carbon: A Review of Graphene, *Chem. Rev.*, 110 (2010) 132-145.
- [16] D. Chen, L. Tang, J. Li, Graphene-based materials in electrochemistry, *Chem. Soc. Rev.*, 39 (2010) 3157-3180.
- [17] A. Ambrosi, C.K. Chua, N.M. Latiff, A.H. Loo, C.H. Wong, A.Y. Eng, A. Bonanni, M. Pumera, Graphene and its electrochemistry - an update, *Chem. Soc. Rev.*, 45 (2016) 2458-2493.
- [18] A. Ismach, C. Druzgalski, S. Penwell, A. Schwartzberg, M. Zheng, A. Javey, J. Bokor, Y. Zhang, Direct chemical vapor deposition of graphene on dielectric surfaces, *Nano Lett.*, 10 (2010) 1542-1548.
- [19] D. Cohen Tanugi, J.C. Grossman, Water desalination across nanoporous graphene, *Nano Lett.*, 12 (2012) 3602-3608.

- [20] S.-Y. Yang, K.-H. Chang, H.-W. Tien, Y.-F. Lee, S.-M. Li, Y.-S. Wang, J.-Y. Wang, C.-C.M. Ma, C.-C. Hu, Design and tailoring of a hierarchical graphene-carbon nanotube architecture for supercapacitors, *J. Mater. Chem.*, 21 (2011) 2374-2380.
- [21] Z. Yang, J. Tian, Z. Yin, C. Cui, W. Qian, F. Wei, Carbon nanotube- and graphene-based nanomaterials and applications in high-voltage supercapacitor: A review, *Carbon*, 141 (2019) 467-480.
- [22] X. Chen, B. Wu, Y. Liu, Direct preparation of high quality graphene on dielectric substrates, *Chem. Soc. Rev.*, 45 (2016) 2057-2074.
- [23] J.B. Wu, M.L. Lin, X. Cong, H.N. Liu, P.H. Tan, Raman spectroscopy of graphene-based materials and its applications in related devices, *Chem. Soc. Rev.*, 47 (2018) 1822-1873.
- [24] Y.K. Kim, H. Park, Light-harvesting multi-walled carbon nanotubes and CdS hybrids: Application to photocatalytic hydrogen production from water, *Energy Environ. Sci.*, 4 (2011) 685-694.
- [25] Y.M. Li, Z.G. Wang, X.J. Lv, N-doped TiO₂ nanotubes/N-doped graphene nanosheets composites as high performance anode materials in lithium-ion battery, *J. Mater. Chem. A*, 2 (2014) 15473-15479.
- [26] L. Lin, B. Deng, J. Sun, H. Peng, Z. Liu, Bridging the Gap between Reality and Ideal in Chemical Vapor Deposition Growth of Graphene, *Chem. Rev.*, 118 (2018) 9281-9343.
- [27] L.P. Zhang, Z.H. Xia, Mechanisms of Oxygen Reduction Reaction on Nitrogen-Doped Graphene for Fuel Cells, *J. Phys. Chem. C*, 115 (2011) 11170-11176.
- [28] J. Deng, P.J. Ren, D.H. Deng, L. Yu, F. Yang, X.H. Bao, Highly active and durable non-precious-metal catalysts encapsulated in carbon nanotubes for hydrogen evolution reaction, *Energy Environ. Sci.*, 7 (2014) 1919-1923.
- [29] Y. Zhao, R. Nakamura, K. Kamiya, S. Nakanishi, K. Hashimoto, Nitrogen-doped carbon nanomaterials as non-metal electrocatalysts for water oxidation, *Nat. Commun.*, 4 (2013) 2390.
- [30] B.S. Yeo, A.T. Bell, Enhanced activity of gold-supported cobalt oxide for the electrochemical evolution of oxygen, *J. Am. Chem. Soc.*, 133 (2011) 5587-5593.
- [31] K.S. Novoselov, A.K. Geim, S.V. Morozov, D. Jiang, M.I. Katsnelson, I.V. Grigorieva, S.V. Dubonos, A.A. Firsov, Two-dimensional gas of massless Dirac fermions in graphene, *Nature*, 438 (2005) 197-200.

- [32] A.C. Ferrari, J.C. Meyer, V. Scardaci, C. Casiraghi, M. Lazzeri, F. Mauri, S. Piscanec, D. Jiang, K.S. Novoselov, S. Roth, A.K. Geim, Raman spectrum of graphene and graphene layers, *Phys. Rev. Lett.*, 97 (2006) 187401.
- [33] A.C. Ferrari, Raman spectroscopy of graphene and graphite: Disorder, electron–phonon coupling, doping and nonadiabatic effects, *Solid State Commun.*, 143 (2007) 47-57.
- [34] Q.F. Zheng, B.G. Han, X. Cui, X. Yu, J.P. Ou, Graphene-engineered cementitious composites: Small makes a big impact, *Nanomater. Nanotechnol.*, 7 (2017) 1-18.
- [35] G. AK, N. KS., The rise of graphene, *Nat. Mater.*, 6 (2007).
- [36] X. Li, W. Cai, J. An, S. Kim, J. Nah, D. Yang, R. Piner, A. Velamakanni, I. Jung, E. Tutuc, S.K. Banerjee, L. Colombo, R.S. Ruoff, Large-area synthesis of high-quality and uniform graphene films on copper foils, *Science*, 324 (2009) 1312-1314.
- [37] B. Krauss, T. Lohmann, D.H. Chae, M. Haluska, K. von Klitzing, J.H. Smet, Laser-induced disassembly of a graphene single crystal into a nanocrystalline network, *Phys. Rev. B*, 79 (2009).
- [38] K.S. Novoselov, A.K. Geim, S.V. Morozov, D. Jiang, Y. Zhang, S.V. Dubonos, I.V. Grigorieva, A.A. Firsov, Electric Field Effect in Atomically Thin Carbon Films, *science*, 306 (2004) 666-669.
- [39] M. Batzill, The surface science of graphene: Metal interfaces, CVD synthesis, nanoribbons, chemical modifications, and defects, *Surf. Sci. Rep.*, 67 (2012) 83-115.
- [40] A.W. Tsen, L. Brown, M.P. Levendorf, F. Ghahari, P.Y. Huang, R.W. Havener, C.S. Ruiz-Vargas, D.A. Muller, P. Kim, J. Park, Tailoring electrical transport across grain boundaries in polycrystalline graphene, *Science*, 336 (2012) 1143-1146.
- [41] V.N. Mochalin, O. Shenderova, D. Ho, Y. Gogotsi, The properties and applications of nanodiamonds, *Nat. Nanotechnol.*, 7 (2011) 11-23.
- [42] J.R. Wang, Vitreous Carbon-A New Versatile Electrode Material, *Electrochemical Acta*, 26 (1981) 1721–1726.
- [43] J. Kong, A.M. Cassell, H. Dai, Chemical vapor deposition of methane for single-walled carbon nanotubes, *Chem. Phys. Lett.*, 292 (1998) 567-574.
- [44] P. Chen, High H₂ Uptake by Alkali-Doped Carbon Nanotubes Under Ambient Pressure and Moderate Temperatures, *Science*, 285 (1999) 91-93.
- [45] S. Iijima, Helical microtubules of graphitic carbon, *Nature*, 354 (1991) 56-58.
- [46] K. Kaiser, H.L. Anderson, F. Schulz, P. Gawel, L. Gross, L.M. Scriven, An sphybridized molecular carbon allotropecyclo[18]carbon, *Science*, 1914 (2019).

- [47] G.S. Choi, Y.S. Cho, S.Y. Hong, J.B. Park, K.H. Son, D.J. Kim, Carbon nanotubes synthesized by Ni-assisted atmospheric pressure thermal chemical vapor deposition, *J. Appl. Phys.*, 91 (2002) 3847-3854.
- [48] O.A. Louchev, T. Laude, Y. Sato, H. Kanda, Diffusion-controlled kinetics of carbon nanotube forest growth by chemical vapor deposition, *J. Chem. Phys.*, 118 (2003) 7622-7634.
- [49] H.M. Cheng, F. Li, G. Su, H.Y. Pan, L.L. He, X. Sun, M.S. Dresselhaus, Large-scale and low-cost synthesis of single-walled carbon nanotubes by the catalytic pyrolysis of hydrocarbons, *Appl. Phys. Lett.*, 72 (1998) 3282-3284.
- [50] D. Ugarte, A. Chatelain, W.A. de Heer, Nanocapillarity and Chemistry in Carbon Nanotubes, *Science*, 274 (1996) 1897-1899.
- [51] Y. Chen, D.T. Shaw, L.P. Guo, Field emission of different oriented carbon nanotubes, *Appl. Phys. Lett.*, 76 (2000) 2469-2471.
- [52] F. Zhao, H.Y. Duan, W.G. Wang, J. Wang, Synthesis and characterization of magnetic Fe/CNTs composites with controllable Fe nanoparticle concentration, *Physica B: Condensed Matter*, 407 (2012) 2495-2499.
- [53] L.M. Hoyos-Palacio, A.G. Garcia, J.F. Perez-Robles, J. Gonzalez, H.V. Martinez-Tejada, Catalytic effect of Fe, Ni, Co and Mo on the CNTs production, *Iop Conf Ser-Mat Sci*, 59 (2014).
- [54] M. Junga, K.Y. Eunb, J.K. Leeb, K.R. Leeb, Y.J. Baikb, J.W. Parka, Growth of carbon nanotubes by chemical vapor deposition, *Diamond Relat. Mater.*, 10 (2001) 1235-1240.
- [55] S. Gottardi, K. Muller, L. Bignardi, J.C. Moreno-Lopez, T.A. Pham, O. Ivashenko, M. Yablonskikh, A. Barinov, J. Bjork, P. Rudolf, M. Stohr, Comparing graphene growth on Cu(111) versus oxidized Cu(111), *Nano Lett.*, 15 (2015) 917-922.
- [56] Z. Sun, Z. Yan, J. Yao, E. Beitler, Y. Zhu, J.M. Tour, Growth of graphene from solid carbon sources, *Nature*, 468 (2010) 549-552.
- [57] Z. Li, P. Wu, C. Wang, X. Fan, W. Zhang, X. Zhai, C. Zeng, Z. Li, J. Yang, J. Hou, Low-temperature growth of graphene by chemical vapor deposition using solid and liquid carbon sources, *ACS Nano*, 5 (2011) 3385-3390.
- [58] A. Kokalj, N. Bonini, S.d. Gironcoli, C. Sbraccia, G. Fratesi, S. Baroni, Methane Dehydrogenation on Rh@Cu(111): A First-Principles Study of a Model Catalyst, *J. Am. Chem. Soc.*, 128 (2006) 12448-12454.

- [59] W. Zhang, P. Wu, Z. Li, J. Yang, First-Principles Thermodynamics of Graphene Growth on Cu Surfaces, *J. Phys. Chem. C*, 115 (2011) 17782-17787.
- [60] H. Partridge, C.W. Bauschlicher, The dissociation energies of CH₄ and C₂H₂ revisited, *J. Chem. Phys.*, 103 (1995) 10589-10596.
- [61] Y. Wang, A.J. Page, Y. Nishimoto, H.J. Qian, K. Morokuma, S. Irle, Template effect in the competition between Haeckelite and graphene growth on Ni(111): quantum chemical molecular dynamics simulations, *J. Am. Chem. Soc.*, 133 (2011) 18837-18842.
- [62] G. Imamura, K. Saiki, Synthesis of Nitrogen-Doped Graphene on Pt(111) by Chemical Vapor Deposition, *J. Phys. Chem. C*, 115 (2011) 10000-10005.
- [63] G. Gajewski, C.W. Pao, Ab initio calculations of the reaction pathways for methane decomposition over the Cu (111) surface, *J. Chem. Phys.*, 135 (2011) 064707.
- [64] K. Maj, I. Kocemba, Nanostructured forms of carbon deposit obtained during cracking of methane reaction over nanocrystalline iron catalysts, *Adsorpt. Sci. Technol.*, 36 (2017) 493-507.
- [65] M. Kumar, Y. Ando, Chemical Vapor Deposition of Carbon Nanotubes: A Review on Growth Mechanism and Mass Production, *J. Nanosci. Nanotechnol.*, 10 (2010) 3739-3758.
- [66] L.M. Malard, M.A. Pimenta, G. Dresselhaus, M.S. Dresselhaus, Raman spectroscopy in graphene, *Phys. Rep.*, 473 (2009) 51-87.
- [67] A.C. Ferrari, J. Robertson, Interpretation of Raman spectra of disordered and amorphous carbon, *Phys. Rev. B*, 61 (1999) 14095-14107.
- [68] L. Tarruell, D. Greif, T. Uehlinger, G. Jotzu, T. Esslinger, Creating, moving and merging Dirac points with a Fermi gas in a tunable honeycomb lattice, *Nature*, 483 (2012) 302-305.
- [69] I.V. Antonova, Chemical vapor deposition growth of graphene on copper substrates: current trends, *Phys. Uspekhi*, 56 (2013) 1013-1020.
- [70] J. Gao, J. Zhao, F. Ding, Transition metal surface passivation induced graphene edge reconstruction, *J. Am. Chem. Soc.*, 134 (2012) 6204-6209.
- [71] J. Maultzsch, S. Reich, C. Thomsen, Double-resonant Raman scattering in graphite: Interference effects, selection rules, and phonon dispersion, *Phys. Rev. B*, 70 (2004) 155403.

- [72] M.S. Dresselhaus, A. Jorio, R. Saito, Characterizing Graphene, Graphite, and Carbon Nanotubes by Raman Spectroscopy, *Annu. Rev. Condens. Matter Phys.*, 1 (2010) 89-108.
- [73] A.C. Ferrari, D.M. Basko, Raman spectroscopy as a versatile tool for studying the properties of graphene, *Nat. Nanotechnol.*, 8 (2013) 235-246.
- [74] S. Reich, C. Thomsen, Raman spectroscopy of graphite, *Philos. Trans. R. Soc. London A*, 362 (2004) 2271-2288.
- [75] R. Beams, L. Gustavo Cancado, L. Novotny, Raman characterization of defects and dopants in graphene, *J. Phys. Condens. Matter*, 27 (2015) 083002.
- [76] E.J. Heller, Y. Yang, L. Kocia, W. Chen, S. Fang, M. Borunda, E. Kaxiras, Theory of Graphene Raman Scattering, *ACS Nano*, 10 (2016) 2803-2818.
- [77] W. Xu, N. Mao, J. Zhang, Graphene: a platform for surface-enhanced Raman spectroscopy, *Small*, 9 (2013) 1206-1224.
- [78] R. Smoluchowski, Anisotropy of the Electronic Work Function of Metals, *Phys. Rev.*, 60 (1941) 661-674.
- [79] I. Milošević, N. Kepčija, E. Dobardžić, M. Damnjanović, M. Mohr, J. Maultzsch, C. Thomsen, Kohn anomaly in graphene, *Mater. Sci. Eng., B*, 176 (2011) 510-511.
- [80] J. Kurti, V. Zolyomi, A. Gruneis, H. Kuzmany, Double resonant Raman phenomena enhanced by van Hove singularities in single-wall carbon nanotubes, *Phys. Rev. B*, 65 (2002) 165433.
- [81] J.S. Park, A. Reina, R. Saito, J. Kong, G. Dresselhaus, M.S. Dresselhaus, G' band Raman spectra of single, double and triple layer graphene, *Carbon*, 47 (2009) 1303-1310.
- [82] K.S. Hazra, J. Rafiee, M.A. Rafiee, A. Mathur, S.S. Roy, J. McLauhlin, N. Koratkar, D.S. Misra, Thinning of multilayer graphene to monolayer graphene in a plasma environment, *Nanotechnology*, 22 (2011) 025704.
- [83] Z.Y. Juang, C.Y. Wu, C.W. Lo, W.Y. Chen, C.F. Huang, J.C. Hwang, F.R. Chen, K.C. Leou, C.H. Tsai, Synthesis of graphene on silicon carbide substrates at low temperature, *Carbon*, 47 (2009) 2026-2031.
- [84] Y. Li, P. Chen, G. Zhou, J. Li, J. Wu, B.L. Gu, S.B. Zhang, W. Duan, Dirac fermions in strongly bound graphene systems, *Phys. Rev. Lett.*, 109 (2012) 206802.
- [85] D.L. Mafra, E.A. Moujaes, S.K. Doorn, H. Htoon, R.W. Nunes, M.A. Pimenta, A study of inner process double-resonance Raman scattering in bilayer graphene, *Carbon*, 49 (2011) 1511-1515.

- [86] W. Liu, H. Li, C. Xu, Y. Khatami, K. Banerjee, Synthesis of high-quality monolayer and bilayer graphene on copper using chemical vapor deposition, *Carbon*, 49 (2011) 4122-4130.
- [87] T. Schiros, D. Nordlund, L. Palova, D. Prezzi, L. Zhao, K.S. Kim, U. Wurstbauer, C. Gutierrez, D. Delongchamp, C. Jaye, D. Fischer, H. Ogasawara, L.G. Pettersson, D.R. Reichman, P. Kim, M.S. Hybertsen, A.N. Pasupathy, Connecting dopant bond type with electronic structure in N-doped graphene, *Nano Lett.*, 12 (2012) 4025-4031.
- [88] L. Lin, L. Liao, J. Yin, H. Peng, Z. Liu, Building graphene p–n junctions for next-generation photodetection, *Nano Today*, 10 (2015) 701-716.
- [89] T. Ando, The electronic properties of graphene and carbon nanotubes, *NPG Asia Mater.*, 1 (2009) 17-21.
- [90] G.W. Flynn, Perspective: The dawning of the age of graphene, *J. Chem. Phys.*, 135 (2011) 050901.
- [91] Y.F. Lu, S.T. Lo, J.C. Lin, W. Zhang, J.Y. Lu, F.H. Liu, C.M. Tseng, Y.H. Lee, C.T. Liang, L.J. Li, Nitrogen-Doped Graphene Sheets Grown by Chemical Vapor Deposition: Synthesis and Influence of Nitrogen Impurities on Carrier Transport, *ACS Nano*, 7 (2013) 6522–6532.
- [92] B. Guo, Q. Liu, E. Chen, H. Zhu, L. Fang, J.R. Gong, Controllable N-doping of graphene, *Nano Lett.*, 10 (2010) 4975-4980.
- [93] W. Chen, D. Qi, X. Gao, A.T.S. Wee, Surface transfer doping of semiconductors, *Prog. Surf. Sci.*, 84 (2009) 279-321.
- [94] X. Meng, S. Tongay, J. Kang, Z. Chen, F. Wu, S.-S. Li, J.-B. Xia, J. Li, J. Wu, Stable p- and n-type doping of few-layer graphene/graphite, *Carbon*, 57 (2013) 507-514.
- [95] Y. Hou, X. Geng, Y. Li, B. Dong, L. Liu, M. Sun, Electrical and Raman properties of p-type and n-type modified graphene by inorganic quantum dot and organic molecule modification, *Sci. China Phys. Mech.*, 54 (2011) 416-419.
- [96] C.D. Pinto, D. De, V.G. Hadjiev, H. Peng, AB-Stacked Multilayer Graphene Synthesized via Chemical Vapor Deposition: A Characterization by Hot Carrier Transport, *ACS Nano*, 6 (2012) 1142-1148.
- [97] B. Deng, Z. Pang, S. Chen, X. Li, C. Meng, J. Li, M. Liu, J. Wu, Y. Qi, W. Dang, H. Yang, Y. Zhang, J. Zhang, N. Kang, H. Xu, Q. Fu, X. Qiu, P. Gao, Y. Wei, Z. Liu, H. Peng, Wrinkle-Free Single-Crystal Graphene Wafer Grown on Strain-Engineered Substrates, *ACS Nano*, 11 (2017) 12337-12345.

- [98] S.M. Haile, Fuel cell materials and components, *Acta Mater.*, 51 (2003) 5981-6000.
- [99] F. de Bruijn, The current status of fuel cell technology for mobile and stationary applications, *Green Chem.*, 7 (2005).
- [100] M. Bron, F. Jaouen, D. Singh, J. King, U.S. Ozkan, K. Lee, N. Alonso - Vante, J. Zhang, A. Ishihara, H. Imai, K.i. Ota, E. Dy, Z. Shi, J. Pan, C. Chen, L. Zhuang, Rongzhong, J.D. Chu, Q. Li, G. Wu, W. Chu, D. Higgins, Z. Chen, R. Cai, H. Tanaka, K. Asazawa, T. Sakamoto, Non-Noble Metal Fuel Cell Catalysts, in: Z. Chen, J.P. Dodelet, J.Z. Dodelet (Eds.) *Non-Noble Metal Fuel Cell Catalysts* 2014.
- [101] S.J. Peighambardoust, S. Rowshanzamir, M. Amjadi, Review of the proton exchange membranes for fuel cell applications, *Int. J. Hydrog. Energy*, 35 (2010) 9349-9384.
- [102] K. Tomantschger, F. McClusky, L. Oporto, A. Reid, K. Kordesch, Development of low cost alkaline fuel cells, *J. Power Sources*, 18 (1986) 317-335.
- [103] N. Sammes, R. Bove, K. Stahl, Phosphoric acid fuel cells: Fundamentals and applications, *Curr. Opin. Solid State Mater. Sci.*, 8 (2004) 372-378.
- [104] R. Yadav, A. Subhash, N. Chemmenchery, B. Kandasubramanian, Graphene and Graphene Oxide for Fuel Cell Technology, *Ind. Eng. Chem. Res.*, 57 (2018) 9333-9350.
- [105] R. Lan, S. Tao, A simple high-performance matrix-free biomass molten carbonate fuel cell without CO₂ recirculation, *Science Advances*, 2 (2016) e1600772.
- [106] S.M. Haile, D.A. Boysen, C.R.I. Chisholm, R.B. Merle, Solid acids as fuel cell electrolytes, *Nature*, 410 (2001) 910-913.
- [107] N. Mahato, A. Banerjee, A. Gupta, S. Omar, K. Balani, Progress in material selection for solid oxide fuel cell technology: A review, *Prog. Mater Sci.*, 72 (2015) 141-337.
- [108] A.I. Baranov, L.A. Shuvalov, N.M. Shchagina, Super conductivity and phase transition in CsHSO₄ and CsHSeO₄ crystals, *JETP Lett.*, 36 (1982) 459-462.
- [109] A. Pawlowski, C. Pawlaczyk, B. Hilczer, Electric conductivity in crystal group Me₃H(SeO₄)₂ (Me: NH₄⁺, Rb⁺, Cs⁺), *Solid State Ionics*, 44 (1990) 17-19.
- [110] C.R.I. Chisholm, S.M. Haile, Superprotonic behavior of Cs(HSO₄)(H₂PO₄) – a new solid acid in the CsHSO₄–CsH₂PO₄ system, *Solid State Ionics*, 136-137 (2000) 229-241.

- [111] L. Kirpichnikova, M. Połomska, A. Pietraszko, B. Hilczer, L. Szczesniak, Domain Structure in $[(\text{NH}_4)_{1-x}\text{Rb}_x]_3\text{H}(\text{SO}_4)_2$ Mixed Crystals in the Vicinity of Ferroelastic-Superprotonic Transition, *Fer*, 290 (2003) 61-69.
- [112] S.M. Haile, C.R. Chisholm, K. Sasaki, D.A. Boysen, T. Uda, Solid acid proton conductors: from laboratory curiosities to fuel cell electrolytes, *Faraday Discuss.*, 134 (2007) 17-39.
- [113] G. Kim, F. Blanc, Y.-Y. Hu, C.P. Grey, Understanding the Conduction Mechanism of the Protonic Conductor CsH_2PO_4 by Solid-State NMR Spectroscopy, *J. Phys. Chem. C*, 117 (2013) 6504-6515.
- [114] T. Uda, S.M. Haile, Thin-membrane solid-acid fuel cell, *Electrochem. Solid-State Lett.*, 8 (2005) A245-A246.
- [115] Á. Varga, N.A. Brunelli, M.W. Louie, K.P. Giapis, S.M. Haile, Composite nanostructured solid-acid fuel-cell electrodes via electrospray deposition, *J. Mater. Chem.*, 20 (2010) 6309.
- [116] A. Varga, *American Journal of Nano Research and Application*, 2 (2014) 61-65.
- [117] A. Varga, M. Pfohl, N.A. Brunelli, M. Schreier, K.P. Giapis, S.M. Haile, Carbon nanotubes as electronic interconnects in solid acid fuel cell electrodes, *Phys. Chem. Chem. Phys.*, 15 (2013) 15470-15476.
- [118] F.P. Lohmann, P.S.C. Schulze, M. Wagner, O. Naumov, A. Lotnyk, B. Abel, A. Varga, The next generation solid acid fuel cell electrodes: stable, high performance with minimized catalyst loading, *J. Mater. Chem. A*, 5 (2017) 15021-15025.
- [119] T.F. Yeh, J. Cihlář, C.Y. Chang, C. Cheng, H. Teng, Roles of graphene oxide in photocatalytic water splitting, *Mater. Today*, 16 (2013) 78-84.
- [120] F. Dong, Z. Zhao, T. Xiong, Z. Ni, W. Zhang, Y. Sun, W.K. Ho, In situ construction of g-C₃N₄/g-C₃N₄ metal-free heterojunction for enhanced visible-light photocatalysis, *ACS Appl. Mater. Interfaces*, 5 (2013) 11392-11401.
- [121] M. De Volder, S. Park, S. Tawfick, A.J. Hart, Strain-engineered manufacturing of freeform carbon nanotube microstructures, *Nat. Commun.*, 5 (2014) 4512.
- [122] H. An, B.H. Tan, J.G.S. Moo, S. Liu, M. Pumera, C.D. Ohl, Graphene Nanobubbles Produced by Water Splitting, *Nano Lett.*, 17 (2017) 2833-2838.
- [123] S. Rummler, M. Steimecke, S. Schimpf, M. Hartmann, S. Forster, M. Bron, Highly Graphitic, Mesoporous Carbon Materials as Electrocatalysts for Vanadium Redox Reactions in All-Vanadium Redox-Flow Batteries, *J. Electrochem. Soc.*, 165 (2018) A2510-A2518.

- [124] M. Steimecke, S. Rummeler, N.-F. Schuhmacher, T. Lindenberg, M. Hartmann, M. Bron, A Comparative Study of Functionalized High-Purity Carbon Nanotubes towards the V(IV)/V(V) Redox Reaction Using Cyclic Voltammetry and Scanning Electrochemical Microscopy, *Electroanal.*, 29 (2017) 1056-1061.
- [125] K. Qu, Y. Zheng, Y. Jiao, X. Zhang, S. Dai, S.Z. Qiao, Polydopamine-Inspired, Dual Heteroatom-Doped Carbon Nanotubes for Highly Efficient Overall Water Splitting, *Adv. Energy Mater.*, 7 (2017).
- [126] H. Ji, L. Zhang, M.T. Pettes, H. Li, S. Chen, L. Shi, R. Piner, R.S. Ruoff, Ultrathin graphite foam: a three-dimensional conductive network for battery electrodes, *Nano Lett.*, 12 (2012) 2446-2451.
- [127] X. Zhang, X. Zhang, H. Xu, Z. Wu, H. Wang, Y. Liang, Iron-Doped Cobalt Monophosphide Nanosheet/Carbon Nanotube Hybrids as Active and Stable Electrocatalysts for Water Splitting, *Adv. Funct. Mater.*, 27 (2017) 1606635.
- [128] Y. Xu, W. Tu, B. Zhang, S. Yin, Y. Huang, M. Kraft, R. Xu, Nickel Nanoparticles Encapsulated in Few-Layer Nitrogen-Doped Graphene Derived from Metal-Organic Frameworks as Efficient Bifunctional Electrocatalysts for Overall Water Splitting, *Adv. Mater.*, 29 (2017).
- [129] G. Jia, Y. Hu, Q. Qian, Y. Yao, S. Zhang, Z. Li, Z. Zou, Formation of Hierarchical Structure Composed of (Co/Ni)Mn-LDH Nanosheets on MWCNT Backbones for Efficient Electrocatalytic Water Oxidation, *ACS Appl. Mater. Interfaces*, 8 (2016) 14527-14534.
- [130] M.I. Kairi, S. Dayou, N.I. Kairi, S.A. Bakar, B. Vigolo, A.R. Mohamed, Toward high production of graphene flakes – a review on recent developments in their synthesis methods and scalability, *J. Mater. Chem. A*, 6 (2018) 15010-15026.
- [131] D.K. James, J.M. Tour, <ar300127r.pdf>, *Acc. Chem. Res.*, 46 (2013) 2307–2318 '.
- [132] D. Chao, B. Ouyang, P. Liang, T.T.T. Huong, G. Jia, H. Huang, X. Xia, R.S. Rawat, H.J. Fan, C-Plasma of Hierarchical Graphene Survives SnS Bundles for Ultrastable and High Volumetric Na-Ion Storage, *Adv. Mater.*, 30 (2018) e1804833.
- [133] X. Zhong, R. Wang, W. Yangyang, L. Yali, Carbon nanotube and graphene multiple-thread yarns, *Nanoscale*, 5 (2013) 1183-1187.
- [134] D.R. Kauffman, A. Star, Graphene versus carbon nanotubes for chemical sensor and fuel cell applications, *Analyst*, 135 (2010) 2790-2797.

- [135] D.A.C. Brownson, G.C. Smith, C.E. Banks, Graphene oxide electrochemistry: the electrochemistry of graphene oxide modified electrodes reveals coverage dependent beneficial electrocatalysis, *R. Soc. Open Sci.*, 4 (2017) 171128-171142.
- [136] O. Naumov, S. Naumov, R. Flyunt, B. Abel, A. Varga, Fast Degradation for High Activity: Oxygen- and Nitrogen-Functionalised Carbon Nanotubes in Solid-Acid Fuel-Cell Electrodes, *ChemSusChem*, 9 (2016) 3298-3306.
- [137] Y.J. Oh, J.J. Yoo, Y.I. Kim, J.K. Yoon, H.N. Yoon, J.H. Kim, S.B. Park, Oxygen functional groups and electrochemical capacitive behavior of incompletely reduced graphene oxides as a thin-film electrode of supercapacitor, *Electrochimica Acta*, 116 (2014) 118-128.
- [138] L. Xue, Y. Li, X. Liu, Q. Liu, J. Shang, H. Duan, L. Dai, J. Shui, Zigzag carbon as efficient and stable oxygen reduction electrocatalyst for proton exchange membrane fuel cells, *Nat. Commun.*, 9 (2018) 3819.
- [139] M. Rychcik, M. Skyllas-Kazacos, Characteristics of a New All-Vanadium Redox Flow Battery, *J. Power Sources*, 22 (1988) 59-67.
- [140] K.L. Huang, X.G. Li, S.Q. Liu, N. Tan, L.Q. Chen, Research progress of vanadium redox flow battery for energy storage in China, *Renewable Energy*, 33 (2008) 186-192.
- [141] F. Rahman, M. Skyllas-Kazacos, Vanadium redox battery: Positive half-cell electrolyte studies, *J. Power Sources*, 189 (2009) 1212-1219.
- [142] K.J. Kim, M.S. Park, Y.J. Kim, J.H. Kim, S.X. Dou, M. Skyllas-Kazacos, A technology review of electrodes and reaction mechanisms in vanadium redox flow batteries, *J. Mater. Chem. A*, 3 (2015) 16913-16933.
- [143] E. Sum, M. Rychcik, M. Skyllas-Kazacos, Investigation of the V(V)/V(IV) system for use in the positive half-cell of a redox battery, *J. Power Sources*, 16 (1985) 85-95.
- [144] T.M. Tseng, R.H. Huang, C.Y. Huang, C.C. Liu, K.L. Hsueh, F.S. Shieu, Carbon Felt Coated with Titanium Dioxide/Carbon Black Composite as Negative Electrode for Vanadium Redox Flow Battery, *J. Electrochem. Soc.*, 161 (2014) A1132-A1138.
- [145] S. Wang, X. Zhao, T. Cochell, A. Manthiram, Nitrogen-Doped Carbon Nanotube/Graphite Felts as Advanced Electrode Materials for Vanadium Redox Flow Batteries, *J. Phys. Chem. Lett.*, 3 (2012) 2164-2167.
- [146] Y. Hou, X.D. Zhuang, X.L. Feng, Recent Advances in Earth-Abundant Heterogeneous Electrocatalysts for Photoelectrochemical Water Splitting, *Small Methods*, 1 (2017) 1700090

- [147] S.C. Huang, Y.Y. Meng, S.M. He, A. Goswami, Q.L. Wu, J.H. Li, S.F. Tong, T. Asefa, M.M. Wu, N-, O-, and S-Tridoped Carbon-Encapsulated Co₉S₈ Nanomaterials: Efficient Bifunctional Electrocatalysts for Overall Water Splitting, *Adv. Funct. Mater.*, 27 (2017) 1606585.
- [148] B. You, Y. Sun, Innovative Strategies for Electrocatalytic Water Splitting, *Acc. Chem. Res.*, (2018).
- [149] H. Duan, D. Li, Y. Tang, Y. He, S. Ji, R. Wang, H. Lv, P.P. Lopes, A.P. Paulikas, H. Li, S.X. Mao, C. Wang, N.M. Markovic, J. Li, V.R. Stamenkovic, Y. Li, High-Performance Rh₂P Electrocatalyst for Efficient Water Splitting, *J. Am. Chem. Soc.*, 139 (2017) 5494-5502.
- [150] Y. Zheng, Y. Jiao, Y. Zhu, L.H. Li, Y. Han, Y. Chen, A. Du, M. Jaroniec, S.Z. Qiao, Hydrogen evolution by a metal-free electrocatalyst, *Nat. Commun.*, 5 (2014) 3783.
- [151] E. Fabbri, A. Habereder, K. Waltar, R. Kotz, T.J. Schmidt, Developments and perspectives of oxide-based catalysts for the oxygen evolution reaction, *Catal. Sci. Technol.*, 4 (2014) 3800-3821.
- [152] R.R. Rao, M.J. Kolb, N.B. Halck, A.F. Pedersen, A. Mehta, H. You, K.A. Stoerzinger, Z. Feng, H.A. Hansen, H. Zhou, L. Giordano, J. Rossmeisl, T. Vegge, I. Chorkendorff, I.E.L. Stephens, Y. Shao-Horn, Towards identifying the active sites on RuO₂(110) in catalyzing oxygen evolution, *Energy Environ. Sci.*, 10 (2017) 2626-2637.
- [153] Y. Li, H. Wang, L. Xie, Y. Liang, G. Hong, H. Dai, MoS₂ nanoparticles grown on graphene: an advanced catalyst for the hydrogen evolution reaction, *J. Am. Chem. Soc.*, 133 (2011) 7296-7299.
- [154] J. Du, F. Cheng, S. Wang, T. Zhang, J. Chen, M(salen)-derived nitrogen-doped M/C (M = Fe, Co, Ni) porous nanocomposites for electrocatalytic oxygen reduction, *Sci. Rep.*, 4 (2014) 4386.
- [155] X. Lu, W.L. Yim, B.H. Suryanto, C. Zhao, Electrocatalytic oxygen evolution at surface-oxidized multiwall carbon nanotubes, *J. Am. Chem. Soc.*, 137 (2015) 2901-2907.
- [156] J.K. Nørskov, T. Bligaard, A. Logadottir, J.R. Kitchin, J.G. Chen, S. Pandelov, U. Stimming, Trends in the Exchange Current for Hydrogen Evolution, *J. Electrochem. Soc.*, 152 (2005) J23-J26.

- [157] I.C. Man, H.Y. Su, F. Calle-Vallejo, H.A. Hansen, J.I. Martinez, N.G. Inoglu, J. Kitchin, T.F. Jaramillo, J.K. Norskov, J. Rossmeisl, Universality in Oxygen Evolution Electrocatalysis on Oxide Surfaces, *Chemcatchem*, 3 (2011) 1159-1165.
- [158] Y.H. Chang, C.T. Lin, T.Y. Chen, C.L. Hsu, Y.H. Lee, W. Zhang, K.H. Wei, L.J. Li, Highly efficient electrocatalytic hydrogen production by MoS(x) grown on graphene-protected 3D Ni foams, *Adv. Mater.*, 25 (2013) 756-760.
- [159] G. Xie, K. Zhang, B. Guo, Q. Liu, L. Fang, J.R. Gong, Graphene-based materials for hydrogen generation from light-driven water splitting, *Adv. Mater.*, 25 (2013) 3820-3839.
- [160] G. Chieffi, C. Giordano, M. Antonietti, D. Esposito, FeNi nanoparticles with carbon armor as sustainable hydrogenation catalysts: towards biorefineries, *J. Mater. Chem. A*, 2 (2014) 11591-11596.
- [161] S. Wu, G. Wen, J. Wang, J. Rong, B. Zong, R. Schlögl, D.S. Su, Nitrobenzene reduction catalyzed by carbon: does the reaction really belong to carbocatalysis?, *Catal. Sci. Technol.*, 4 (2014) 4183-4187.
- [162] Z.B. Tian, C. Liu, Q.Y. Li, J.Y. Hou, Y. Li, S.Y. Ai, Nitrogen- and oxygen-functionalized carbon nanotubes supported Pt-based catalyst for the selective hydrogenation of cinnamaldehyde, *Appl. Catal., A*, 506 (2015) 134-142.

The content of this chapter has been submitted for publication in Journal of Materials Chemistry A as

Chapter 2 Contribution of Zigzag Carbon and Armchair Carbon Coupled with Functionalized Groups to Oxygen Reduction Activity for Precious Metal Free Solid Acid Fuel Cell

Xubin Lu, Xin Yang, Tariq Muhammad, Fan Li, Matthias Steimecke, Jia Li, Michael Bron, Bernd Abel and Aron Varga

Abstract

Due to the prohibitive cost associated with precious metal catalysts, in recent years, the scientific community has invested considerable time and effort into investigating whether non-precious-metals can effectively serve as catalysts. This area of research is particularly pertinent to the large-scale commercial application of low and intermediate temperature fuel cells, as the industry is currently hindered by the need for a high amount of Platinum (Pt) catalysts. In this work, we applied O₂ and N₂ plasma treatment to metal-free, edge-abundant, oxygen-functionalized, and nitrogen-doped graphene; and successfully employed it as an electrode catalyst in a solid acid fuel cell (SAFC). Scanning electron microscopy (SEM), Raman spectroscopy, and X-ray photoelectron spectroscopy (XPS) analysis of the graphene layers were used to characterize the materials' properties. Performed at cathodic conditions, AC impedance spectroscopy of the hybrid electrode, containing both the plasma-etched graphene and CsH₂PO₄ (CDP), showed remarkable catalytic activity. Thus, both O₂ and N₂ plasma treatments activated the material. While oxygen plasma was a more effective activator, it also resulted in higher degradation rates. The combination of density functional theory calculation and experimentation indicates that the zigzag (ZZ) carbon is the most active site for the oxygen reduction reaction (ORR) on both the O₂ and N₂ plasma-etched graphene. Furthermore, the armchair (AM) carbon adjacent to the surface oxygen groups and doping heteroatom is another main active site for O₂ and N₂ plasma-etched graphene, respectively. The results of this study will guide future endeavours in developing non-precious metal catalytically active and stable materials for fuel cell cathodes.

2.1 Introduction

The prohibitive cost of precious metal catalysts has recently spurred the scientific community to invest considerable time and effort into investigating whether carbon-based materials can serve as effective catalysts. This area of research is particularly pertinent to the large-scale commercial application of low- and intermediate-temperature fuel cells, because the industry is currently hindered by the need for large amounts of platinum catalysts. By virtue of its extensive versatility, graphene is considered a promising material for a wide range of technological applications. Recently, various forms of graphene, e.g., flakes, bundles, and reduced graphene oxide,^[1, 2] have served as catalytically active components in electrochemical cells, successfully promoting electrode reactions.

Of particular interest is the preparation of metal-free catalysts by introducing heteroatoms (e.g., nitrogen, sulfur, boron) on sp^2 carbon nanomaterials. Recent reports also indicated that a high concentration of edges can catalyze the oxygen reduction reaction (ORR) in both alkaline and acidic electrolytes. Because doping graphene with heteroatoms often markedly alters its electronic structure, it has been suggested that dopant heteroatoms may play an important role in promoting ORR catalytic activity in their vicinity.^[3, 4] Thus, nitrogen (N_2) plasma treatment is a promising approach to develop metal-free catalysts with abundant catalytic edge sites. Furthermore, the same holds true for oxygen-functionalized graphene, because its ORR catalytic activity can also be increased by introducing surface oxygen species ($C=O$, $C-OH$, $C-OOH$) as well as defect sites.^[5, 6] Wang et al.^[7] reported that the edge of graphite is much more conducive to the ORR than its basal plane. Density functional theory (DFT) calculations have indicated the nature of the active sites in these carbon-based catalysts; zigzag (ZZ) edge defects coupled with pentagon edge defects^[8] are possibly the most active sites for the ORR. Three-dimensional (3D) porous nanostructures are typically used as high-performance electrodes in electrochemical cells. Such structures ensure a high density of catalytically active sites, which leads to low electrode impedance. Because of their large geometrical aspect ratios, graphene flakes can form close-to-ideal interconnected 3D networks. Generally, important insights can be obtained by evaluating experimental results in combination with DFT

calculations. This process can be used as a fundamental approach to identify the most active sites in a material to develop novel solid acid fuel cells (SAFCs).

In this study, a simple two-dimensional (2D) electrode consisting of a graphene layer coated on a cesium dihydrogen phosphate (CDP) electrolyte pellet is used as a model system to study the ORR activity of graphene. Graphene is treated with oxygen (O₂) and N₂ plasma to introduce oxygen functional groups and nitrogen dopants that generate defect sites, respectively. Both types of plasma treatment generate catalytically active sites that supplement the activity of edge-rich graphene. The effects of O₂ and N₂ plasma treatment on the ORR activity of graphene sheets are investigated using DFT calculations. Our results provide important information about the effectiveness of plasma-etched graphene as a metal-free catalyst in SAFCs.

2.2 Methods

2.2.1 Preparation of 1-layer graphene

Graphene was synthesized in a commercial cold-wall reactor (Moorfield Nano-8G) using standard, low-pressure chemical vapor deposition (CVD). Copper (Cu)-foil (Alfa Aesar, stk#13382, 98 % purity, 25 μm thickness) served as the growth substrate. Prior to synthesis, the Cu-foil was cleaned and polished using the following procedure: 1) To remove any organic residue, the foil was first washed in an ultrasonic bath for 10 min in high purity acetone, and then the process was repeated using high purity ethanol; 2) To achieve a smooth surface, the Cu-foil was electropolished in an electrolyte solution at room temperature – consisting of 450 ml phosphoric acid (Alfa Aesar, 85%, stk#A18067) and 150 ml polyethylene glycol additive (Sigma Aldrich, PEG-400) – as well as a large Cu sheet counter electrode. +1.2 V was applied for 30 min during the polishing process; 3) Lastly, the foil was washed for 5 min in DI-water (Millipore) and high purity acetone.

The three-step CVD synthesis procedure is illustrated in Figure S1 and consisted of: 1) A 30 min annealing phase that took place at 1000 °C, in an environment characterized by < 5 mTorr of pressure, and an Ar and H₂ flow rate of 192 and 8 sccm respectively; 2) A 2 min growth phase at 1000 °C, which occurred under 10 mTorr of pressure, and an Ar, H₂, and CH₄ flow rate of 168, 8 and 24 sccm respectively; and 3)

A cool down phase, in which the system passively cooled down under conditions of <5 mTorr of pressure and an Ar and H₂ flow rate of 192 and 8 sccm respectively, reaching less than 200 °C in ~45 min.

2.2.1 Transfer of 1-layer Graphene

Following the synthesis of graphene, it next needed to be transferred onto an electrolyte pellet and a SiO₂/Si wafer for physical and electrochemical characterization. A great challenge lies in the water solubility of CDP electrolyte. First, the synthesized graphene-Cu substrate was coated with 10 ml of a 4 % Poly (methyl methacrylate) (PMMA) solution (Sigma Aldrich, stk#445746-25G M_w~350.000) in Anisole (Alfa Aesar, stk#A12997) film. The coating was applied for 90 s with a spin-rate of 2000 rpm, and then the solvent was evaporated at 90 °C. The process was repeated twice more, with lower spin rates of 1000 and 300 rpm, to obtain a smooth and continuous PMMA film. The PMMA-graphene film was then removed using an electrochemical method, in which the Cu-foil-graphene-PMMA composite served as the working electrode, a 1 cm² piece of Pt foil functioned as the counter electrode, and a 0.5 % NaOH (Sigma Aldrich, stk#S5881) solution acted as the electrolyte. 5 V was applied and maintained for 5-10 min, causing the graphene-PMMA composite to delaminate while hydrogen gas formed at the Cu-foil interface. The free-floating graphene-PMMA foil was gently scooped up with a home-made square-frame tool, washed three times in DI-water, and dried at ambient conditions, as shown in Figures S 2a and b. For Raman and XPS characterization, the graphene film was then transferred onto the SiO₂/Si substrate, and the PMMA film was removed by an acetone wash.

2.2.2 Modification of 1-layer graphene

A low-pressure microwave plasma system (Diener femto, 40 kHz RF), operating at a frequency of 40 kHz and a forward power of 20 W, was used to apply the oxygen plasma treatment to the graphene layers situated on top of the CDP and SiO₂/Si. A 45 sccm pure oxygen flow rate was maintained for 10, 20, 30, and 40 s. Nitrogen plasma treatment was applied to the graphene layers situated on the top of CDP and SiO₂/Si via a low-pressure microwave plasma system (Sentech Etchlab 200 RF) using nitrogen-argon plasma at 13.56 MHz. A forward power of 25 W was maintained for 2, 4, 6, and 10 min with a total flow rate of 30 sccm and an N₂: Ar ratio of 9:1.

2.2.3 Electrochemical half-cell

Electrochemical asymmetric cells (composite electrode|CDP) were assembled using the following procedure: CsCO₃ (35.43 g, 99.99 %, Alfa Aesar) was dissolved in MeOH (technical grade, Carl Roth) under 1000 rpm stirring with a magnetic stir bar. H₃PO₄ (25.07 g, 85 %, Carl Roth) was mixed with 77 mL MeOH (technical grade, Carl Roth). The solution of CsCO₃-MeOH was poured into the solution of H₃PO₄-MeOH under 1500 rpm stirring with a magnetic stir bar. The solution immediately turned white, indicating the formation of the CDP. The precipitates were removed and swashed thoroughly with more MeOH to remove H₂O and dried for 24 h under 80 °C [9, 10]. The hydraulic press (Atlas Auto 15T, Specac Ltd.) was used to construct the CDP pellet (10 mm diameter, 0.5 mm thickness) from the dry, sieved powder (0.25 g, 75 μm final mesh size). The graphene film was then transferred onto one side of a prefabricated CDP electrolyte pellet using the same transfer process as described above. In a final step, the PMMA film was removed by an acetone wash and the graphene layer was dried to obtain CPD|graphene pellet. The counter electrode powder mixture was made from commercially available Pt black nanoparticles (fuel cell grade, Sigma Aldrich), Pt supported on carbon (40 mass % Pt, Alfa Aesar) and CDP micro-particles in a 3 : 1 : 3 mass ratio. The asymmetric cell was fabricated by using the hydraulic press to expose the electrode powder mixture and CDP|graphene to uniaxial pressing at 200 MPa for 20 min. Carbon paper (Toray TGP-H-120) served as the current collector contacting the Pt-composite electrode and the graphene electrode on either side of the electrochemical cell, Figure S3.

2.2.4 Electrochemical characterization

Electrochemical characterization was performed in a single gas (H₂ or O₂) chamber configuration, at SAFC operating conditions: T_G = 240 °C, p_{H₂O} = 0.4 atm, and an oxygen flow rate = 30 sccm. AC impedance spectroscopy was carried out with a Biologic VSP-300 impedance analyzer using a sinusoidal voltage perturbation with 10 mV amplitude and a frequency range from 10 mHz to 7 MHz. During heating and cooling of the cell, at temperatures below 150 °C, condensation was avoided by using a dry Ar purge. The polarization curves were derived from cyclic voltammetry curves, in a potential range of -0.5 to 0.5 V, at a scan rate of 10 mV s⁻¹.

2.2.5 Physical characterization

SEM (Carl Zeiss SMT, Ultra 55) was employed to characterize the surface morphology of the Cu-foil before and after electropolishing, the graphene layer after CVD growth and after transfer onto the SiO₂/Si wafer, and the CDP pellet. X-ray diffraction (XRD) was carried out on a D8 advanced X-ray diffractometer, from Bruker AXS, using Cu K α radiation ($\lambda = 1.5406 \text{ \AA}$) and a step size of 0.013° . Raman spectra were collected using a HORIBA (Jobin Yvon iHR320, synapse CCD) RAMAN spectrometer equipped with an Olympus IX71 microscope for confocal sampling, and using an Nd:YAG at 5 mW (Coherent, Verdi, $\lambda=532 \text{ nm}$). Raman mapping experiments were performed using an x–y stage (Prior, 100 nm resolution) in 500 nm steps, scanning areas of $10 \times 10 \mu\text{m}^2$. X-ray photoelectron spectra were collected using monochromatic AlK α radiation (Kratos, Axis Ultra). Atomic force microscopy (AFM) measurements were performed using NanoWizard 4 from JPK instruments. NSC 15 cantilevers of spring constant $k = 40 \text{ N m}^{-1}$ and resonance frequency $\omega_0 = 325 \text{ kHz}$ purchased from Mikromasch were used. Measurements were done in the net-repulsive regime of intermittent contact mode at a frequency $\omega < \omega_0$ and free amplitude of 1.6 V. Gwyddion software were used to edit and analyze the AFM images.

2.2.6 Computational details

All spin-polarized calculations were performed within the framework of density functional theory, as implemented in the Vienna ab initio simulation package (VASP) [11, 12]. The projected augmented wave (PAW) potential [13] and generalized gradient approximation (GGA) with the Perdew–Burke–Ernzerhof (PBE) functional [14] were used to describe the electron-ion interactions and exchange-correlation energy, respectively. The cutoff energy of 400 eV for plane-wave basis set was employed. The DFT+D3 scheme developed by Grimme [15] was used to consider the non-local Van der Waals (vdW) interaction. The 6×6 supercells of graphene and 1×1 were used in our calculations. The $3 \times 3 \times 1$ and $4 \times 1 \times 1$ gamma centred Monkhorst-Pack k-point sampling in the Brillouin zone was used for graphene sheets and graphene sheets with edges, respectively. The vacuum distance was larger than 15 \AA to eliminate spurious interactions between the periodically repeated images. All atoms were fully relaxed by conjugated gradient (CG) algorithm with the criterion of convergence of

0.01 eV Å⁻¹. The zero-point corrected energies (ZPE) and Gibbs free energies of all ORR intermediates at 298.15K were shown in Table S1.

2.3 Results and Discussion

2.3.1 Characterisation of monolayer graphene

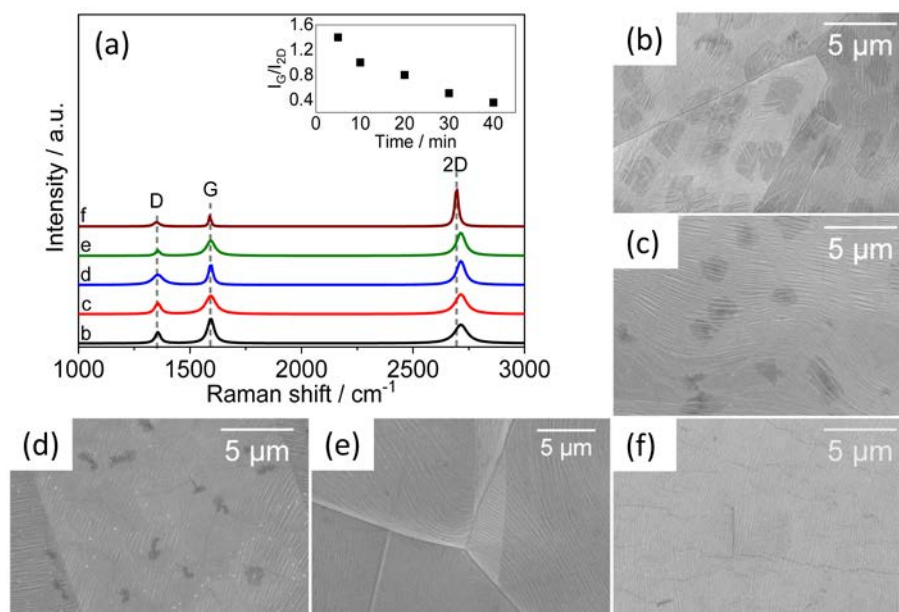


Figure 1. (a) Representative Raman spectra of graphene on SiO₂/Si wafer, showing the effect of electropolishing pretreatment of the copper foil substrate. The G: 2D band intensity ratio (I_G/I_{2D}), shown in the inset, indicates monolayer graphene for polishing times longer than 20 min. Scanning electron micrographs of as-grown graphene on copper foil substrates showing the effect of electropolishing pretreatment with increasing electropolishing time (b) 5 min, (c) 10 min, (d) 20 min, (e) 30 min, and (f) 40 min. With a low magnification of (f). Darker regions are most likely multilayer graphene.

High-quality monolayer graphene was successfully synthesized as detailed in section 2-Materials and Methods. SEM, AFM, Raman spectroscopy, Raman mapping, XRD, and XPS were used to characterize the graphene on an electropolished Cu-foil, a SiO₂/Si wafer, and a CDP pellet. Raman spectroscopy is commonly used to assess the structural properties of sp² carbon materials. The intensity ratio of the G band at 1580 cm⁻¹ and 2-D band at 2680 cm⁻¹ (I_G/I_{2D}) is generally considered a qualitative indicator for decreasing defect density in the graphene layer [16], and single layers will

depict values that are < 0.5 [17, 18]. Figure 1a is the distinctive Raman spectroscopy that exposes a reduction of I_G/I_{2D} as a function of increased polishing time, shown in the inset, indicates monolayer graphene for polishing times longer than 20 min. The SEM images shown in Figure 1(b-f), there is remarkably a decreasing fraction of multi-layer graphene areas (dark patches) as a function of increased polishing time combined with the Raman spectra in Figure 1a. A smooth Cu surface has been shown to significantly improve the quality of the graphene. However, while at polishing time of 40 min, the over-polishing starts to present to the Cu edge. As shown in Figure 1e and Figure S4, to ensure the prepared monolayers were all of the same quality, a 30 min polishing time was selected for all further experiments.

2.3.2 Characterisation of the graphene-based electrode

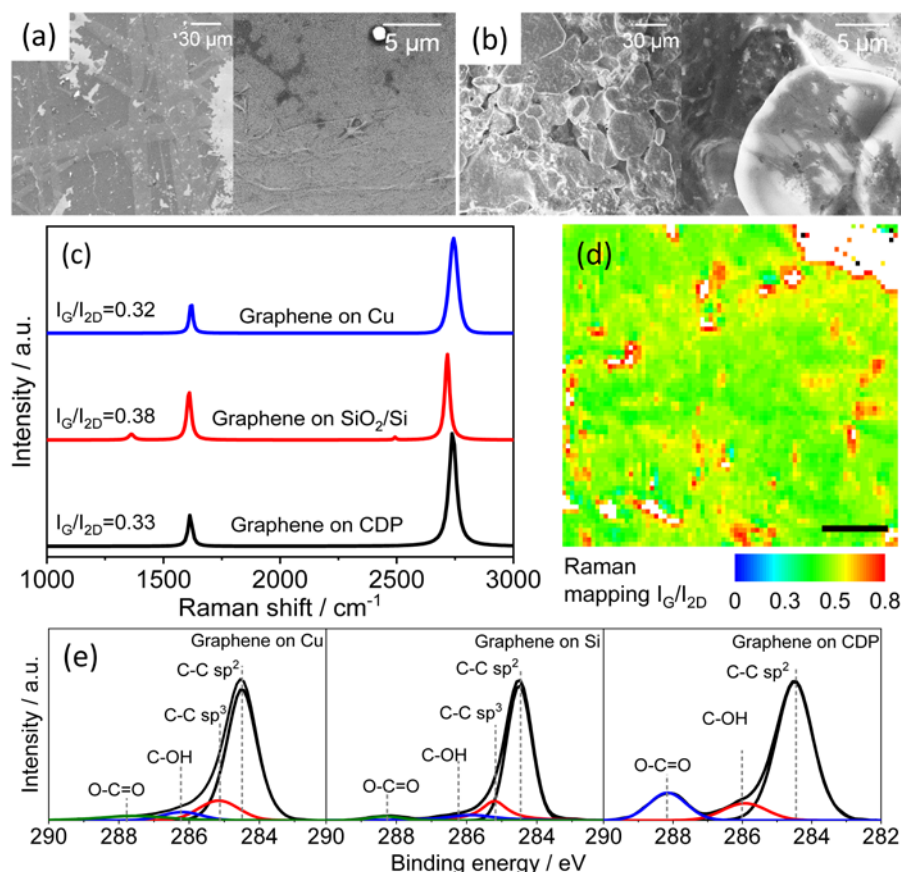


Figure 2. (a) Scanning electron micrographs at low and high magnification of graphene on (a) SiO_2/Si wafer and (b) CDP substrate. (c) Fitted Raman spectra of graphene on Cu foil, SiO_2/Si wafer, and CDP substrate. (d) Raman mapping of as-transferred graphene on the SiO_2/Si substrate extracted from Figure S 5. Scale bar = 20 μm . (e)

The XPS spectra of pristine graphene on the copper, as-transferred on SiO₂/Si wafer and CDP substrate.

To facilitate the further analysis and achievement of optimizing parameter, the monolayer graphene, as mentioned above, was simultaneously transferred onto both the SiO₂/Si and CDP substrates. The SEM images in Figures 2a and b show a significant amount of wrinkling in the graphene layers. Furthermore, graphene free regions are observed on both the SiO₂/Si and CDP substrate, a result of the aforementioned wrinkles. The distinctive ripples from graphene synthesis are due to the Cu atoms moving underneath the graphene layer during growth [19, 20]. To date, there is no known technique for preventing wrinkle formation during the growth process on the Cu-foil and elimination of these intrinsic wrinkles is also impossible during transfer to other substrates [21]. In addition, the micromorphology of the CDP substrate is extremely rough when compared to that of the SiO₂/Si support, which ultimately fraction of intact graphene is much higher than that of the graphene free regions, and is therefore more dominant in the electrochemical measurements.

The values of I_G/I_{2D} remained <0.38 after the transfer onto the SiO₂/Si wafer and the CDP pellet in Figure 2c. Furthermore, the I_G/I_{2D} intensity ratio of Raman mapping shown in Figure 2d extracted from Figure S5 is mainly less than 0.5. Based on these results, we tentatively assume the graphene is monolayer and will select the same batch of one for further study. XPS analysis of C1s was performed on synthesized graphene atop an electropolished Cu-foil, a SiO₂/Si wafer, and a CDP pellet. The high-resolution spectrum of C1s in Figure 2e shows that there are three distinctive carbon groups in the pristine graphene: C=C at 284.5eV, C-O or C-C at 285.5eV, and C=O peak at 287.5 eV [22]. Note the high contribution of the C=C peak after the graphene was transferred onto the CDP. That peak was nearly as pronounced in the graphene on the Cu-foil or on the SiO₂/Si substrate. For the composite graphene and CDP electrode, the XPS survey spectra in Figure S6 a contained the distinctive Cs 3d peak at ~723.6 eV, O1s peak at 530.2 eV, C1s peak at 284.5 eV, and P 2p peak at 132.8 eV [9, 23]. The evident diffraction peak at ~27.2 ° shown in Figure S4 b can be attributed to carbon (002) [24] and distinguished from representative diffraction peaks of CDP.

2.3.3 Plasma-etched graphene

In Childres's study disorder of graphene was introduced by oxygen plasma, indicating an evolution from a graphene lattice to a more amorphous carbon phase [25], which

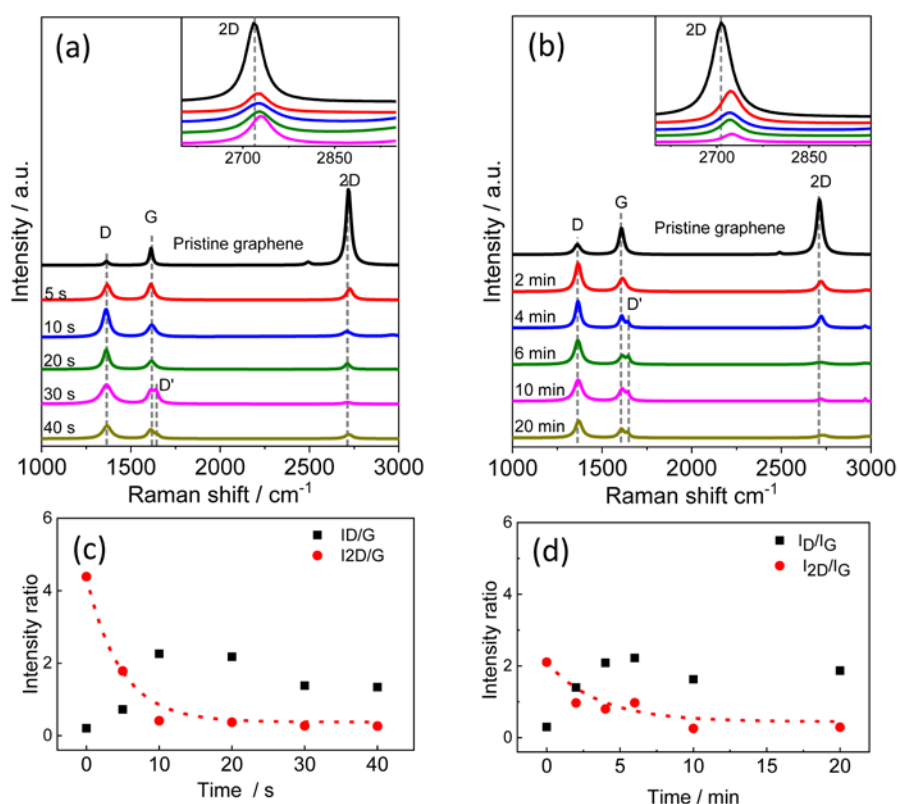


Figure 3. Raman spectra of graphene on SiO₂/Si wafer as a function of (a) oxygen and (b) nitrogen plasma treatment time. (c) and (d) Band intensity ratios taken from Raman spectra of graphene, as a function of (a) O₂ and (b) N₂.

suggest that plasma modification could cause the disorder of graphene as well as the defective site. The same holds true in our experimental results, Figures 3a and b show that exposure to an O₂ plasma and N₂ plasma resulted in an increase of defect density from low to high. The decrease of intensity ratio I_{2D}/I_G and the upshifts of 2D frequencies, shown in the inset, indicate that the doping heteroatom or the presence of charged impurities [26]. Figures 3c and d show that the intensity ratios I_D/I_G and I_{2D}/I_G as a function of plasma treatment time for an O₂ and N₂ plasma, respectively. Dramatic changes in the intensity ratio are observed in the initial phase of the plasma treatment when the treatment time was maintained for 10 s and 10 min for the former and the latter, respectively. With the subsequent decrease of I_D/I_G, the evolution of edge-abundant can be accomplished via O₂ and N₂ plasma treatment. It is apparent, the O₂ plasma treatment is seemingly more aggressive than N₂ plasma treatment, and it

requires much short exposure, which can be attributed to the different approaches as well as the difference between various precursor gases. Thus we restrict ourselves to a qualitative discussion of this difference.

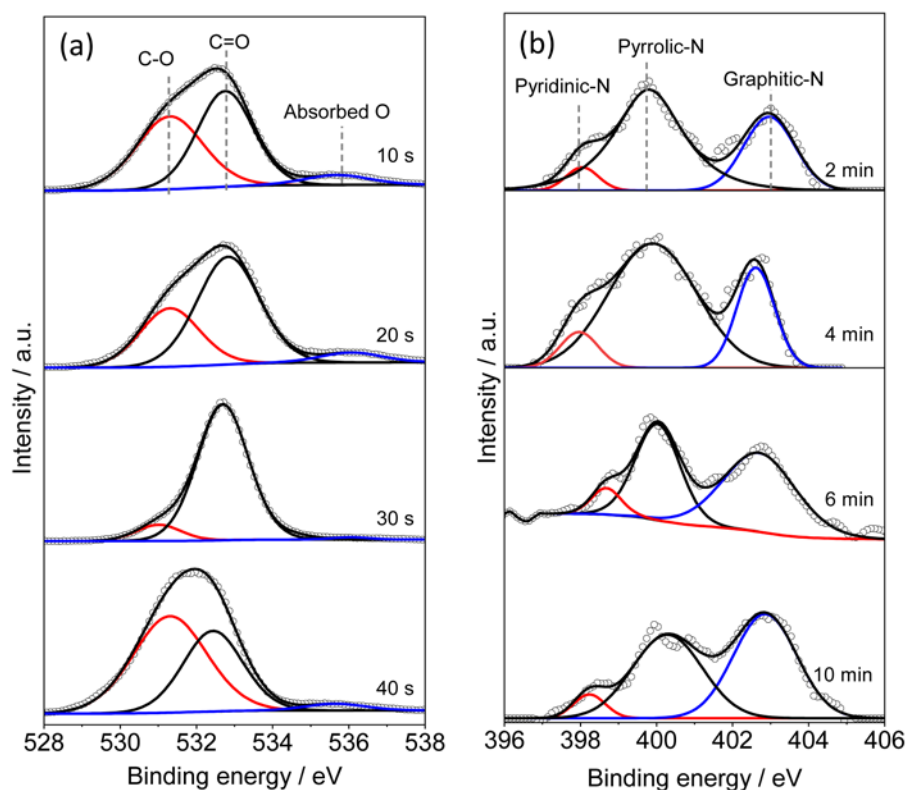


Figure 4

Figure 4. XPS spectra of graphene on SiO₂/Si wafer as a function of oxygen plasma treatment at different times: (a) O 1 s spectra (b) N 1 s spectra.

On the other hand, the surface oxygen species and doping heteroatoms can also be introduced by plasma technology [5, 8]. The corresponding XPS high-resolution O 1 s and N 1 s spectra are shown in Figure 4. The O 1 s spectra can be fitted with three peaks at 531.3, 532.7, and 536 eV, which are assigned to O-C, C=O, and chemisorbed oxygen [27]. Approximated content of C 1s, O1s, and N 1s for the graphene on SiO₂/Si and CDP are summarized in Table S2 compared with pristine graphene on the Cu substrate. In general, the pristine graphene has no nitrogen content and low amounts of oxygen. The sample has c.a. 0.8 % nitrogen content and > 30 % oxygen content, which is commonly acknowledged that the contribution of substrates. Table S3 and Table S4 show that there is remarkably an increase of total oxygen content and decrease of total carbon content as a function of treatment time. This suggests that

further modifications result in a decrease in the total carbon content of graphene-based electrode.

2.3.4 Electrochemical results

In the case of SAFC, alternating current impedance spectroscopy often uses to evaluate the properties of the electrolyte-electrode interface over a frequency range of 1 Hz to 3 MHz [28]. The width of the impedance arc represents the sum of the ORR impedances from the Pt/C/CDP composite and the graphene electrode. Since the impedance from the 3-dimensional, high-performance Pt/C/CDP composite electrode, on the order of $1 \Omega \text{ cm}^2$ [29, 30], is much lower than that of the 2-dimensional pristine graphene electrode, the contribution from the former can be disregarded. The ORR impedance in the Nyquist representation shown in Figure S7 is significantly reduced from $2500 \text{ k}\Omega \cdot \text{cm}^2$ to $400 \text{ k}\Omega \cdot \text{cm}^2$ once the pristine monolayer replaced the graphene free in the cathode electrode. Obviously, there is plenty of cracks and intrinsic defects for the pristine graphene-based electrode combining the results in Figures 2a and b, which potentially facilitates the reaction of ORR. In this study, the impedance of $400 \text{ k}\Omega \cdot \text{cm}^2$ will tentatively be served as a reference for further modifications. Figures 5a and b show that both O_2 and N_2 plasma treatment had a dramatic effect on the electrode impedance. In the case of the O_2 plasma treatment, the values of impedance towards the cathode ORR are respectively 73, 1.3, 0.7 and $50 \text{ k}\Omega \cdot \text{cm}^2$ when the exposure time (t_E) was set to 10, 20, 30 and 40 s. The overpotential (η) at higher current densities shown in Figure 5c follows the trend in activity measured in impedance is $\eta_{30 \text{ s}} < \eta_{20 \text{ s}} < \eta_{40 \text{ s}} < \eta_{10 \text{ s}}$. There was the lowest impedance and overpotential when the modification was maintained for the 30 s. This is an excellent agreement with the results from characterisation, where the total carbon content was about 25.3 at %, the surface function species, C=O, also displayed dramatic coverage on the graphene compared with others. It hints that the plentifully defective site has been achieved but no overtreatment (Table S3). However, further treatment will aggravate the descent of total carbon content, as well as a decreasing percentage of C=O group resulting in an increase of impedance when t_E was set to 40 s. The increase of impedance potentially originates from the decrease of C=O species. This indicates that electrochemical performance is relational for the total carbon content as well as the concentration of surface oxygen groups. Therefore, the contribution of ORR activity

can be ascribed to the defective site, surface oxygen species. Alternatively, with coaction of the defective site and surface oxygen groups could be the most reason towards the reaction of ORR in SAFC.

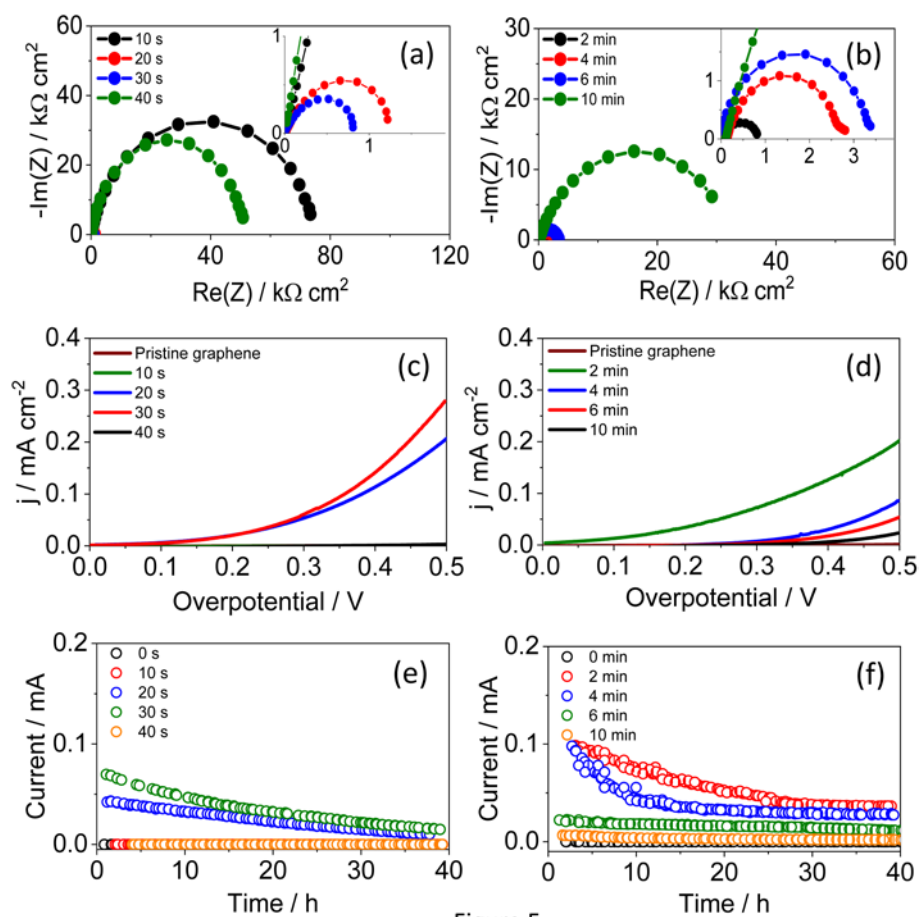


Figure 5

Figure 5. Measurements performed at 240 °C under humidified O₂ gases (pH₂O = 0.4 atm) at a flow rate of 30 sccm oxygen environment in a single chamber setup for graphene|CDP|Pt/C/CDP electrochemical cells with the graphene side subject to O₂ and N₂ plasma treatment. (a) (b) Electrochemical impedance spectroscopy data of the electrochemical cells. (c) (d) The polarization curve obtained with linear sweep cyclic voltammetry at 5 mV s⁻¹. (e, f) Long-term stability test carried out with a DC bias of +500 mV.

The impedance in the case of N₂ plasma treatment shown in Figure 5b were 0.8, 2.8, 3.4, and 29 kΩ·cm² when the treatment time was 2, 4, 6, and 10 min, respectively. Figure 5d demonstrates the trend of overpotential is $\eta_{2 \text{ min}} < \eta_{4 \text{ min}} < \eta_{6 \text{ min}} < \eta_{10 \text{ min}}$ on the electrode. However, Table S4 shows that there is a surprising anti-correlation between

the concentration of dopant as well as the value of I_D/I_G and electrode impedance. It is most likely that it has been brought the total carbon content to a lower value than that of O_2 plasma-etched graphene at $t_E = 40$ s, which expels the effect of both surface function group and doping heteroatom on the promotion of impedance.

There was the lowest impedance and overpotential when the exposure time was set to 2 min. Additional plasma treatment does not have a clear impact on electrode performance and overpotential. However, the impedance still possesses a lower value in the dopants content range from c.a. 1.3 to 1.4 at % (Table S4), which could be ascribed to strong electron withdrawing effect of doping nitrogen towards the reaction of ORR in SAFC. On the other hand, the total carbon content plays a significant role in resulting in a comparable impedance to the lowest value.

While at an exposure time of $t_E = 10$ min the percentage of doping nitrogen is about 1.7 at %, the total carbon content decreases to 17.3 at %. We speculate that damaging effects on the graphene layer become significant and cancel out any possible enhancements. Likewise, it is abundant proof that the enhancements of both heteroatoms and defective site towards the mentioned reaction in SAFC.

Moreover, the corrosion occurs simultaneously at the cathode via a reaction of electrochemical carbon oxidation in the presence of water [31], resulting in the contribution of carbon oxide species and the release of protons and electrons. This degeneration is accordingly the main mode of inactivating the catalyst under the operating temperature of 240 °C in this study. Figures 5e and f show the results of polarization measurements with a 500 mV DC bias, and depict rapid degradation of oxygen and nitrogen plasma treated graphene electrodes over a 40 h time period. For the nitrogen plasma treated layers, a stable plateau is reached, indicating some stability. This is consistent with the corroborated findings based on the nitrogen-doped CNTs towards the ORR, namely that the protonation of the nitrogen doping site results in the degradation coupled with the ORR [32]. Given the strong electron-withdrawing effect of oxygen and nitrogen, we speculate that the same holds true for oxygen-functional groups. Further investigation of the degradation procedure was beyond the scope of this paper.

2.3.5 Mechanism

In the SAFC, kinetics are mainly limited by the cathode reaction, as dictated by the sluggish, four-electron transfer kinetics for the ORR pathway in acidic media [33]. The first reaction begins with the adsorption of the O^{2-} anion and an electron at the catalyst site to form an $*OOH$ species with a proton ($*$ being the adsorption site). Next, H^+ is transmitted with the $*OOH$ species, and an electron is adsorbed to produce H_2O and $*O$. This pathway is followed by the reaction of an H^+ with an $*O$ atom and an electron to form an $*OH$ species, which is then superseded with additional H^+ cationics, leading to the formation of the adsorption site and H_2O . The system then undergoes the desorption of water to reduce O_2 .

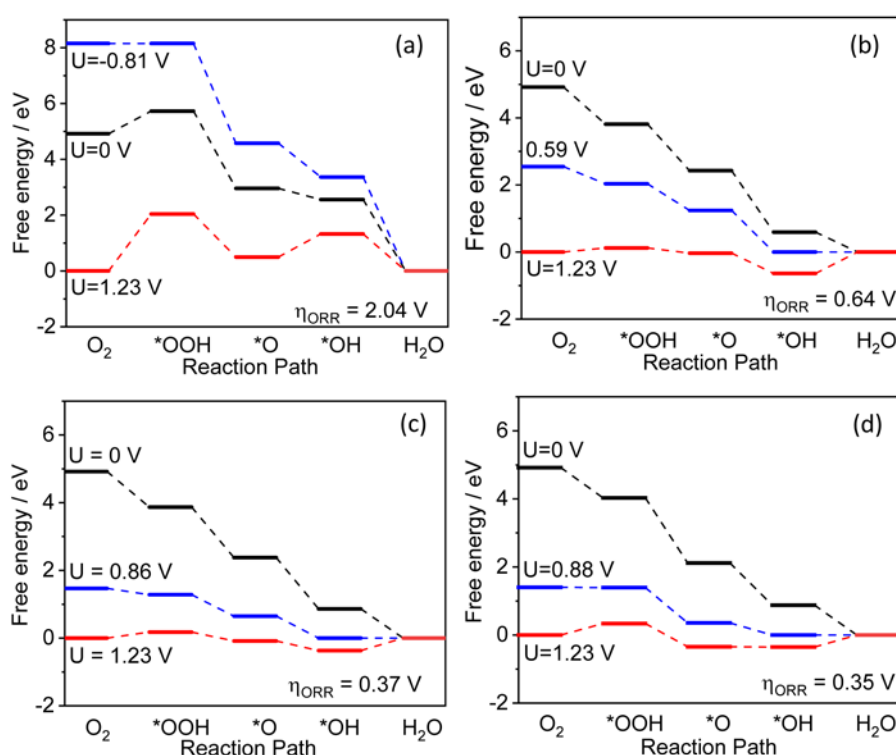


Figure 6

Figure 6. Free energy diagrams of ORR on (a) the pristine basal-plane of graphene zigzag. (b) Edge etched with O_2 plasma and N_2 plasma. (c) $C=O$ armchair edge of a graphene sheet. (d) N -doped armchair edge of graphene sheets. Red circle represent the most active sites, which were plotted according to Table S5.

DFT calculations were performed to further investigate the effect of plasma treatment on ORR activities for graphene sheets. A series of graphene sheet models with different doping sites were constructed (Figure S8 and the corresponding theoretical activities were evaluated (Table S5) under the framework established by Norskov et

al. [34, 35]. Due to the too weak adsorption strength of key ORR intermediates, as shown in Figure 6a, pristine graphene exhibited rather poor ORR catalytic performance, which is in excellent agreement with the result shown in Figure S7 ($400 \text{ k}\Omega\cdot\text{cm}^2$). However, the electrochemical activity of graphene can be improved by plasma treatment, as demonstrated the results in the above. The improvement of catalytic activity induced by plasma treatment could be attributed to two beneficial consequences. The first consequence is to break the graphene sheets and create more edge sites. Figure 6b depicts the free energy diagram of ORR on the zigzag edge site of graphene sheet introduced by the O_2 plasma or N_2 plasma, showing high ORR activity with the overpotential of 0.64 V, which is constant with experimental results, which shows that the enhancement is part due to the defective site introduced by O_2 and N_2 plasma. All the reaction steps proceed simultaneously at $U = 0 \text{ V}$ referenced to a reversible hydrogen electrode (RHE). And when the applied potential increased to 0.59 V, the last step, namely the desorption of $^*\text{OH}$ reached equilibrium, being the potential determining step (PDS) in the overall reaction. It is illustrated that the binding strength between adsorbate and the active site was considerably enhanced compared to pristine graphene, which was even excessively strong, leading to promoted ORR activity.

In addition to edge effect, the second consequence of plasma treatment is to functionalize the edge sites of graphene or dope heteroatoms into the basal plane of graphene sheets, which substantially altered the electronic structure of the active carbon sites via electron-withdrawing effect.[36-39].

In the case of O_2 plasma-etched graphene, we first considered graphene sheets with C=O and C–OH functional groups listed in Table S6 according to the evidenced signals of C=O and C–OH in Figure 4a. The AM edge of graphene sheets with C=O groups exhibited a low overpotential of 0.37 V, as shown in Figure 6c. This is in good agreement with experimental results. The further treatment will facilitate the decrease of total carbon content and percentage of C=O, excepting the corrosion of carbon. The enhancement effect will thus vanish with exposure time. Consequently, the O_2 plasma-etched graphene activity can be attributed to the C=O surface functional group in conjunction with the AM defect and individual carbons of the ZZ edge.

In the case of N₂ plasma-treated graphene, the electrochemical activity was improved by incorporating heteroatoms into the basal plane of graphene sheets, which substantially altered the electronic structure of the carbon active sites via the electron-withdrawing effect. The relevant models with defects were also constructed to identify their synergistic effects in Table S7. The ORR free energy diagram on the N-doped AM edge is shown in Figure 6d, and clearly demonstrates the significant enhancement of ORR activity induced by the heteroatom doping. The PDS at U = 0 vs. RHE remains the last step yet with the lower overpotential of 0.35 V, almost locating at the peak of activity volcano plot [35]. This much boosted ORR activity indicates that the edge effect and heteroatom doping could together optimize the adsorption strength of ORR key intermediates, thus leading to the outstanding catalytic performance demonstrated in our experiment. Likewise, this indicates that the enhancement mostly comes from the coaction of AM-edge and graphitic nitrogen.

2.4 Conclusions

Graphene was synthesized via a standard CVD method and transferred onto a solid acid half-cell consisting of a high-performance Pt-composite electrode, and a CDP electrolyte. Surface functionalization, via oxygen and nitrogen plasma treatment, led to a dramatic, 5000-fold decrease in the electrode impedance; however high activity is also paired with low stability. Interestingly, beyond the step-change of the electrode performance between pristine and plasma treated graphene, there is no clear trend observed with increasing plasma treatment. The improvement of catalytic activity induced by plasma treatment could be attributed to two beneficial consequences. The first consequence is to break the graphene sheets and create more edge sites. The second consequence is to dope heteroatoms and introduce surface functional groups into the basal plane of graphene sheets. In a word, in situ construction of defective sites, surface functional groups, and heteroatoms using O₂ and N₂ plasma treatment, which could tailor the contribution from the pristine graphene and produce edge/defect-rich graphene, has been successfully achieved. Nitrogen-functionalization is observed to be more stable than oxygen functionalization, with the current reaching a steady-state value after 40 h. We did not focus on studying the effect of both oxygen-functionalized species and doping nitrogen on the degradation

of graphene. Therefore, further work investigating potentially more stable dopants, such as sulfur, boron are underway.

2.5 Reference

- [1] A. Varga, M. Pfohl, N.A. Brunelli, M. Schreier, K.P. Giapis, S.M. Haile, Carbon nanotubes as electronic interconnects in solid acid fuel cell electrodes, *Phys. Chem. Chem. Phys.*, 15 (2013) 15470-15476.
- [2] G. Gorgolis, C. Galiotis, Graphene aerogels: a review, *2D Mater.*, 4 (2017) 032001.
- [3] L.P. Zhang, Z.H. Xia, Mechanisms of Oxygen Reduction Reaction on Nitrogen-Doped Graphene for Fuel Cells, *J. Phys. Chem. C*, 115 (2011) 11170-11176.
- [4] J. Deng, P.J. Ren, D.H. Deng, L. Yu, F. Yang, X.H. Bao, Highly active and durable non-precious-metal catalysts encapsulated in carbon nanotubes for hydrogen evolution reaction, *Energy Environ. Sci.*, 7 (2014) 1919-1923.
- [5] Z. Liu, Z. Zhao, Y. Wang, S. Dou, D. Yan, D. Liu, Z. Xia, S. Wang, In Situ Exfoliated, Edge-Rich, Oxygen-Functionalized Graphene from Carbon Fibers for Oxygen Electrocatalysis, *Adv. Mater.*, 29 (2017) 1606207.
- [6] L.Q. Li, J. Yang, H.B. Yang, L.P. Zhang, J.J. Shao, W. Huang, B. Liu, X.C. Dong, Anchoring Mn_3O_4 Nanoparticles on Oxygen Functionalized Carbon Nanotubes as Bifunctional Catalyst for Rechargeable Zinc-Air Battery, *ACS Appl. Energy Mater.*, 1 (2018) 963-969.
- [7] A. Shen, Y. Zou, Q. Wang, R.A. Dryfe, X. Huang, S. Dou, L. Dai, S. Wang, Oxygen reduction reaction in a droplet on graphite: direct evidence that the edge is more active than the basal plane, *Angew. Chem. Int. Ed.*, 53 (2014) 10804-10808.
- [8] Y.F. Jiang, L.J. Yang, T. Sun, J. Zhao, Z.Y. Lyu, O. Zhuo, X.Z. Wang, Q. Wu, J. Ma, Z. Hu, Significant Contribution of Intrinsic Carbon Defects to Oxygen Reduction Activity, *ACS Catal.*, 5 (2015) 6707-6712.
- [9] R.C. Suryaprakash, F.P. Lohmann, M. Wagner, B. Abel, A. Varga, Spray drying as a novel and scalable fabrication method for nanostructured CsH_2PO_4 , Pt-thin-film composite electrodes for solid acid fuel cells, *RSC Adv.*, 4 (2014) 60429-60436.
- [10] F.P. Lohmann, P.S.C. Schulze, M. Wagner, O. Naumov, A. Lotnyk, B. Abel, A. Varga, The next generation solid acid fuel cell electrodes: stable, high performance with minimized catalyst loading, *J. Mater. Chem. A*, 5 (2017) 15021-15025.

- [11] G. Kresse, J. Furthmuller, Efficiency of ab-initio total energy calculations for metals and semiconductors using a plane-wave basis set, *Comp. Mater. Sci.*, 6 (1996) 15-50.
- [12] G. Kresse, J. Furthmuller, Efficient iterative schemes for ab initio total-energy calculations using a plane-wave basis set, *Phys. Rev. B*, 54 (1996) 11169-11186.
- [13] P.E. Blöchl, Projector augmented-wave method, *Phys. Rev. B*, 50 (1994) 17953-17979.
- [14] J.P. Perdew, K. Burke, M. Ernzerhof, Generalized gradient approximation made simple, *Phys. Rev. Lett.*, 77 (1996) 3865-3868.
- [15] S. Grimme, J. Antony, S. Ehrlich, H. Krieg, A consistent and accurate ab initio parametrization of density functional dispersion correction (DFT-D) for the 94 elements H-Pu, *J. Chem. Phys.*, 132 (2010) 154104.
- [16] L.M. Malard, M.A. Pimenta, G. Dresselhaus, M.S. Dresselhaus, Raman spectroscopy in graphene, *Phys. Rep.*, 473 (2009) 51-87.
- [17] Y.H. Kahng, S. Lee, M. Choe, G. Jo, W. Park, J. Yoon, W.K. Hong, C.H. Cho, B.H. Lee, T. Lee, A study of graphene films synthesized on nickel substrates: existence and origin of small-base-area peaks, *Nanotechnology*, 22 (2011) 045706.
- [18] X. Li, W. Cai, J. An, S. Kim, J. Nah, D. Yang, R. Piner, A. Velamakanni, I. Jung, E. Tutuc, S.K. Banerjee, L. Colombo, R.S. Ruoff, Large-area synthesis of high-quality and uniform graphene films on copper foils, *Science*, 324 (2009) 1312-1314.
- [19] J.M. Wofford, S. Nie, K.F. McCarty, N.C. Bartelt, O.D. Dubon, Graphene Islands on Cu foils: the interplay between shape, orientation, and defects, *Nano Lett.*, 10 (2010) 4890-4896.
- [20] K. Hayashi, S. Sato, N. Yokoyama, Anisotropic graphene growth accompanied by step bunching on a dynamic copper surface, *Nanotechnology*, 24 (2013) 025603.
- [21] B. Deng, Z. Pang, S. Chen, X. Li, C. Meng, J. Li, M. Liu, J. Wu, Y. Qi, W. Dang, H. Yang, Y. Zhang, J. Zhang, N. Kang, H. Xu, Q. Fu, X. Qiu, P. Gao, Y. Wei, Z. Liu, H. Peng, Wrinkle-Free Single-Crystal Graphene Wafer Grown on Strain-Engineered Substrates, *ACS Nano*, 11 (2017) 12337-12345.
- [22] C. Deetum, C. Samthong, S. Thongyai, P. Praserttham, A. Somwangthanaroj, Synthesis of well dispersed graphene in conjugated poly(3,4-ethylenedioxythiophene):polystyrene sulfonate via click chemistry, *Compos. Sci. Technol.*, 93 (2014) 1-8.

- [23] J.H. Leal, H. Martinez, I. Martinez, A.D. Price, A.G. Goos, C.E. Botez, Stability of the superprotonic conduction of $(1-x)\text{CsH}_2\text{PO}_4/x\text{SiO}_2$ ($0 \leq x \leq 0.3$) composites under dry and humid environments, *Mater. Today Commun.*, 15 (2018) 11-17.
- [24] F.T. Johra, J.W. Lee, W.G. Jung, Facile and safe graphene preparation on solution based platform, *J. Ind. Eng. Chem.*, 20 (2014) 2883-2887.
- [25] I. Childres, L.A. Jauregui, J.F. Tian, Y.P. Chen, Effect of oxygen plasma etching on graphene studied using Raman spectroscopy and electronic transport measurements, *New J. Phys.*, 13 (2011) 1-12.
- [26] R. Sharma, J.H. Baik, C.J. Perera, M.S. Strano, Anomalously large reactivity of single graphene layers and edges toward electron transfer chemistries, *Nano Lett.*, 10 (2010) 398-405.
- [27] M.C. Ortega-Liebana, N.X. Chung, R. Limpens, L. Gomez, J.L. Hueso, J. Santamaria, T. Gregorkiewicz, Uniform luminescent carbon nanodots prepared by rapid pyrolysis of organic precursors confined within nanoporous templating structures, *Carbon*, 117 (2017) 437-446.
- [28] J.-H. Park, Possible origin of the proton conduction mechanism of CsH_2PO_4 crystals at high temperatures, *Phys. Rev. B*, 69 (2004) 054104.
- [29] T. Uda, S.M. Haile, Thin-membrane solid-acid fuel cell, *Electrochem. Solid-State Lett.*, 8 (2005) A245-A246.
- [30] S.M. Haile, C.R. Chisholm, K. Sasaki, D.A. Boysen, T. Uda, Solid acid proton conductors: from laboratory curiosities to fuel cell electrolytes, *Faraday Discuss.*, 134 (2007) 17-39.
- [31] F.P. Lohmann-Richters, B. Abel, A. Varga, In situ determination of the electrochemically active platinum surface area: key to improvement of solid acid fuel cells, *J. Mater. Chem. A*, 6 (2018) 2700-2707.
- [32] O. Naumov, S. Naumov, B. Abel, A. Varga, The stability limits of highly active nitrogen doped carbon ORR nano-catalysts: a mechanistic study of degradation reactions, *Nanoscale*, 10 (2018) 6724-6733.
- [33] J. Zhang, Z. Zhao, Z. Xia, L. Dai, A metal-free bifunctional electrocatalyst for oxygen reduction and oxygen evolution reactions, *Nat. Nanotechnol.*, 10 (2015) 444-452.

- [34] J.K. Nørskov, T. Bligaard, A. Logadottir, J.R. Kitchin, J.G. Chen, S. Pandelov, U. Stimming, Trends in the Exchange Current for Hydrogen Evolution, *J. Electrochem. Soc.*, 152 (2005) J23-J26.
- [35] J.K. Nørskov, J. Rossmeisl, A. Logadottir, L. Lindqvist, J.R. Kitchin, T. Bligaard, H. Jonsson, Origin of the overpotential for oxygen reduction at a fuel-cell cathode, *J. Phys. Chem. B*, 108 (2004) 17886-17892.
- [36] H. Kim, K. Lee, S.I. Woo, Y. Jung, On the mechanism of enhanced oxygen reduction reaction in nitrogen-doped graphene nanoribbons, *Phys. Chem. Chem. Phys.*, 13 (2011) 17505-17510.
- [37] B.S. Yeo, A.T. Bell, Enhanced activity of gold-supported cobalt oxide for the electrochemical evolution of oxygen, *J. Am. Chem. Soc.*, 133 (2011) 5587-5593.
- [38] Y. Zhao, R. Nakamura, K. Kamiya, S. Nakanishi, K. Hashimoto, Nitrogen-doped carbon nanomaterials as non-metal electrocatalysts for water oxidation, *Nat. Commun.*, 4 (2013) 2390.
- [39] L. Xue, Y. Li, X. Liu, Q. Liu, J. Shang, H. Duan, L. Dai, J. Shui, Zigzag carbon as efficient and stable oxygen reduction electrocatalyst for proton exchange membrane fuel cells, *Nat. Commun.*, 9 (2018) 3819.

2.6 Supporting information

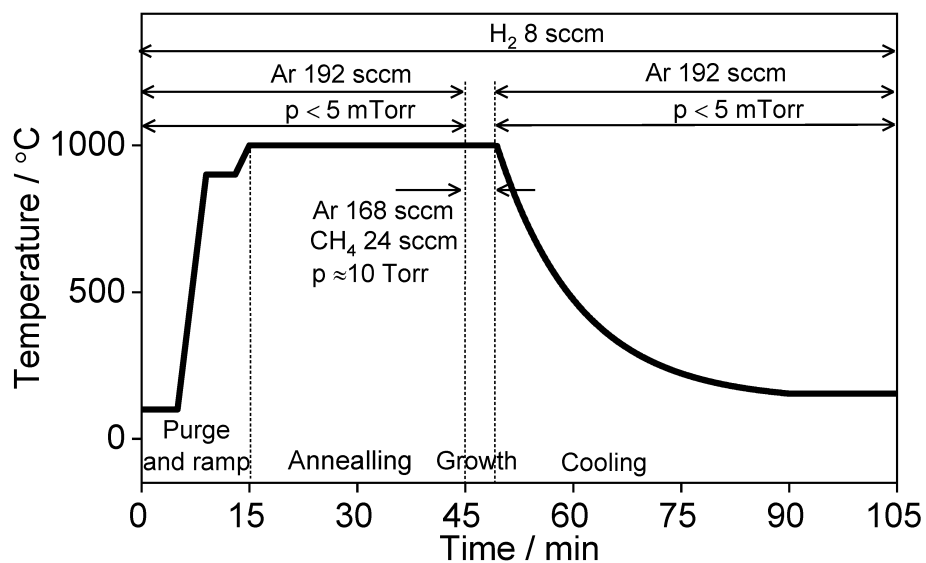


Figure S1. Synthesis parameters for chemical vapor deposition (CVD) of graphene, on the copper foil as the growth substrate.

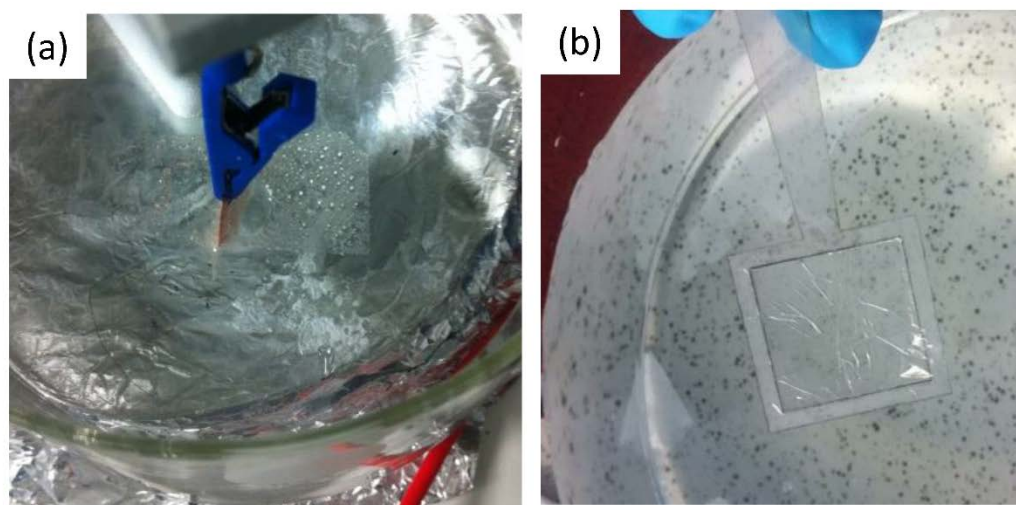


Figure S2. Delamination of graphene from copper foil with an electrochemical method and insulated graphene@PMMA film.

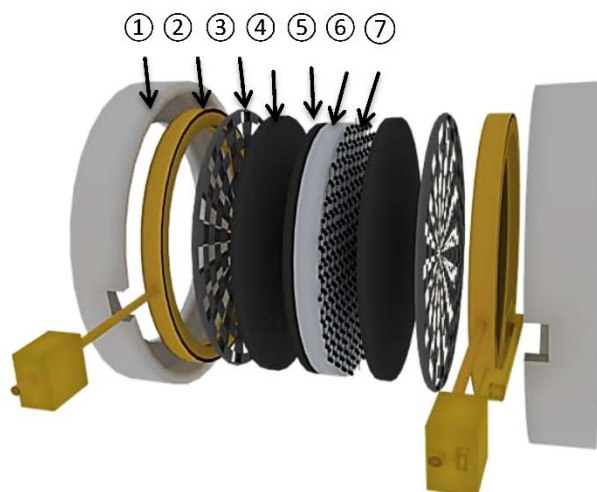


Figure S3. Simple schematic drawing of an asymmetric electrochemical cell (Graphene|CDP|Pt/C/CDP) as a side view. (1) PTFE frame, (2) Conducting ring, (3) gas diffusion layer, (4) Carbon paper, (5) Pt/C/CDP, (6) CDP, and (7) Graphene.

	*OH	*O	*OOH	H ₂ O	H ₂
ZPE	0.36	0.07	0.40	0.56	0.27
TS	~	~	~	0.67	0.41

Table S1. ZPE and entropic corrections at T = 298.15 K

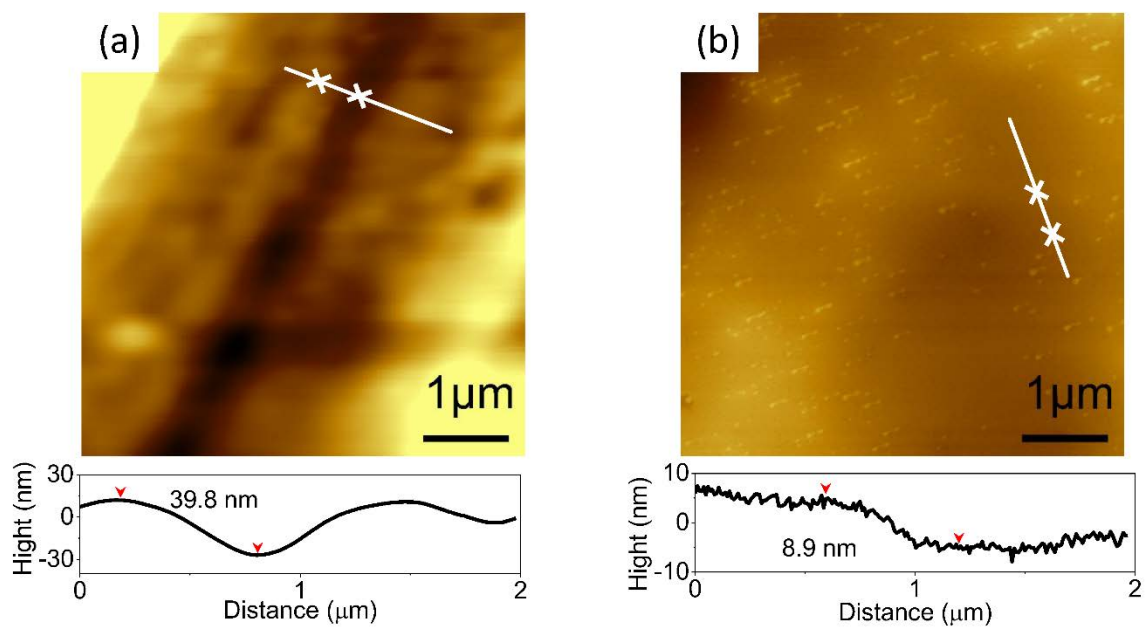


Figure S4. AFM height image of (a) pristine copper foil and (b) as-polished copper foil. Color scale: 0-150 nm.

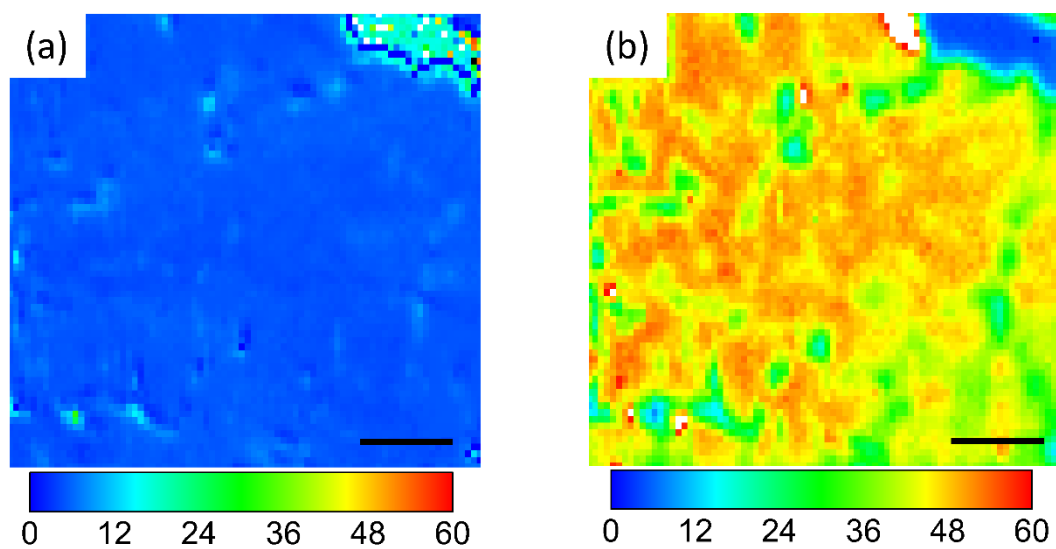


Figure S5. The Raman mapping of as-transferred graphene on the SiO₂/Si substrate (a) G band, (b) 2D band. Scale bar = 20 μm.

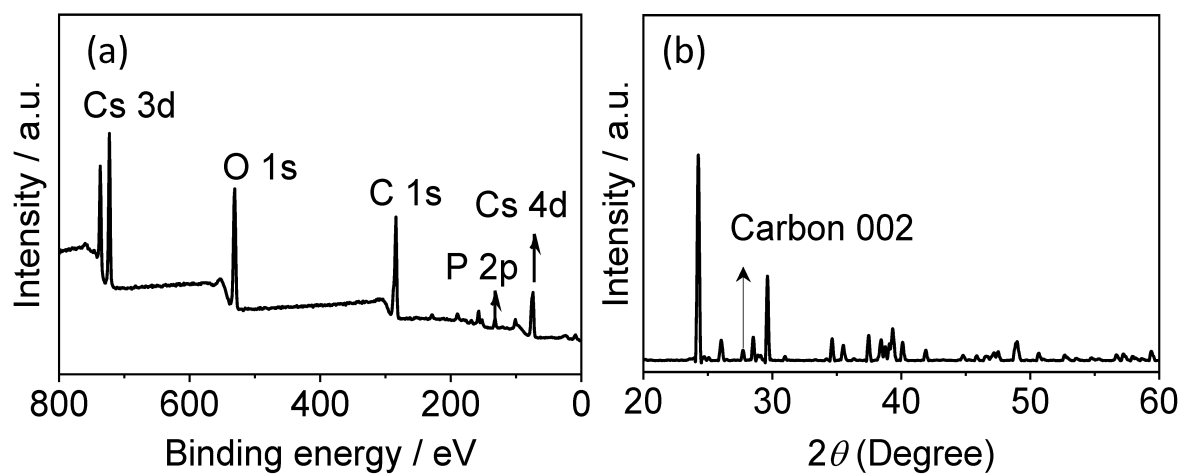


Figure S6. (a) The XPS survey spectra of graphene on CDP substrate. (b) The XRD of graphene on the CDP substrate.

Table S2. Integrated atomic concentrations of graphene on Cu, SiO₂/Si, and CDP substrates from XPS characterization.

Binding energy			
	Total	Total	Total
	284.5	398.2	530.6
	C 1 s / %	N 1 s / %	O 1 s / %
Graphene on Cu	53.8	0	2.7
Graphene on SiO ₂ /Si	60.4	0.8	38.8
Graphene on CDP	57.8	0	30.7

Table S3. Integrated atomic concentrations of graphene on SiO₂/Si substrate with increasing treatment time of O₂ plasma from XPS characterization.

Binding energy				
	Total	Total	Total	
	284.5 eV	398.2 eV	530.6 eV	532.6 eV
	C 1 s / %	N 1 s / %	O 1 s / %	C=O / %
10 s	46.8	0.6	52.0	21.9
20 s	53.0	0.7	46.3	27.1
30 s	25.3	0.6	73.3	68.1
40 s	23.0	0.8	76.1	30.2

Table S4. Integrated atomic concentrations of graphene on SiO₂/Si substrate with increasing treatment time of N₂ plasma from XPS characterization.

	Binding energy			
	Total 284.5 eV C 1 s / %	Total 398.2 eV N 1 s / %	Total 530.6 eV O 1 s / %	Total 402.8 eV g-N / %
2 min	21.1	1.3	77.6	0.4
4 min	19.6	1.1	79.3	0.3
6 min	20.0	1.4	78.6	0.6
10 min	17.3	1.7	81.0	0.9

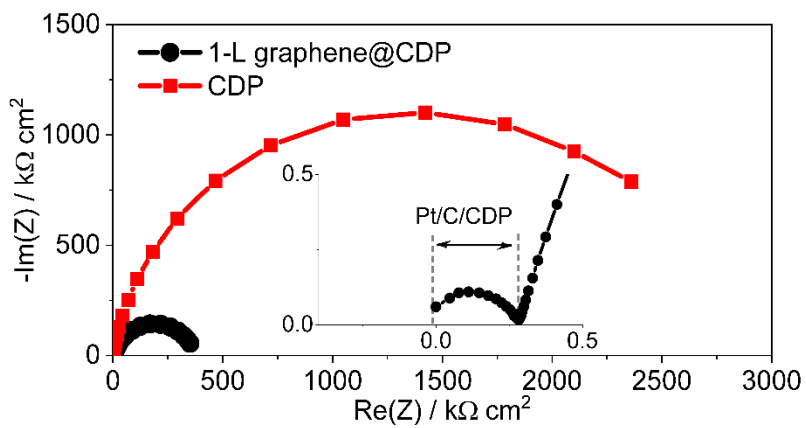


Figure S7. Impedance spectra shown in the Nyquist representation for graphene|CDP|Pt/C/CDP and CDP electrochemical cells with the graphene side subject to pristine graphene. The measurements were performed at 240°C under a humidified oxygen environment in a single chamber setup.

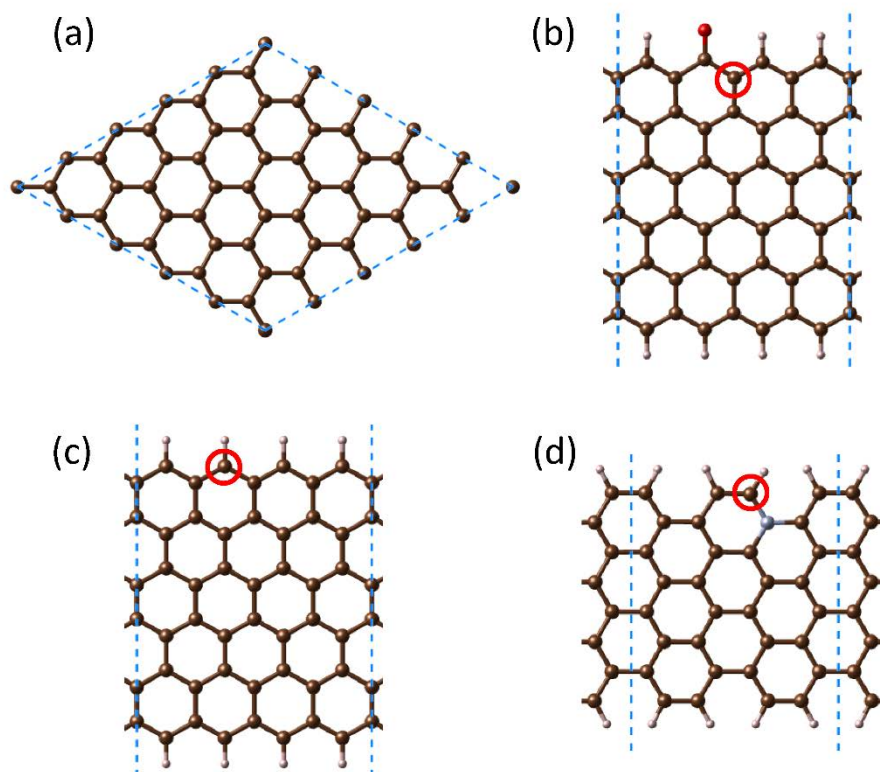


Figure S8. Atomic models and corresponding reaction site (red circle) of (a) pristine graphene, (b) O-functionalized graphene, (c) zigzag edge of graphene, and (d) N-doped armchair edge of graphene.

Table S5. Adsorption free energies of *OH, *O and *OOH.

Model	ΔG^{*OOH}	ΔG^{*O}	ΔG^{*OH}
Pristine	5.729	2.959	2.556
ZZ-edge	3.768	2.427	0.593
C=O-AM	3.870	2.376	0.863
Pyridinic-N-AM	4.903	2.603	1.731
Graphitic-AM	4.029	2.116	0.879

Table S 6. ORR overpotential of DFT theoretical studies on oxygen plasma treatment graphene. Armchair: AM. Zigzag: ZZ (NA indicates failure of O₂ adsorptions).

Models	ORR overpotentials (V)
ZZ-edge	0.64
AM-edge	NA
C=O-ZZ	NA
C=O-AM	0.37
C-OH-ZZ	NA
C-OH-AM	NA

Table S 7. ORR overpotential of DFT theoretical studies on nitrogen plasma treatment graphene. Armchair: AM. Zigzag: ZZ (NA indicates failure of O₂ adsorptions).

Models	ORR overpotentials (V)
ZZ-edge	0.64
AM-edge	NA
Pyridinic-N-bulk	NA
Pyridinic-N-AM	1.2
Pyridinic-N-ZZ	NA
Pyrrolic-N-AM	NA
Pyrrolic-N-ZZ	NA
Graphitic-bulk	0.84
Graphitic-N-AM	0.35
Graphitic-N-ZZ	NA

*The content of this chapter has been submitted for publication in Electrochimica Acta
as*

Chapter 3 Novel and High-efficient Three-Dimensional Hybrid Electrodes for Vanadium Redox Flow Battery Applications

Xubin Lu, Fan Li, Matthias Steimecke, Muhammad Tariq and Michael Bron

Abstract

Titanium, either in form of a Ti foil or in form of a Ti mesh, was used as a novel substrate to grow nitrogen-doped carbon nanotubes (NCNTs) by chemical vapour deposition (CVD) at moderate temperatures over electrodeposited iron particles. The thus-prepared high-surface-area electrodes were characterized using scanning electron microscopy (SEM), Raman spectroscopy, and X-ray photoelectron spectroscopy (XPS). The electrochemical performance towards the V(IV)/V(V) redox couple was investigated using cyclic voltammetry. The parameters for iron particle electrodeposition were adjusted towards high and uniform substrate coverage. Nanotube growth from acetonitrile at moderate temperatures (600 °C) led to N-containing CNTs with a high amount of graphitic nitrogen. NCNTs grown over Ti substrates provide promising performances towards the V(IV)/V(V) as well as the V(III)/V(IV) redox pair. Furthermore, Ti as an inert substrate towards the mentioned reaction enables to study the performance of the deposited catalyst materials themselves.

3.1 Introduction

The all-vanadium redox flow battery (VRFB) is considered one of the most promising solutions for stationary storage of fluctuating renewable energy, which is based on its advantageous characteristics including high and flexible capacity, high energy efficiency, and long cycle life ^[1, 2]. The energy in VRFBs is stored using redox reactions of dissolved species, and the respective redox pair in the positive electrolyte solution is $\text{VO}^{2+}/\text{VO}_2^+$ and in the negative one $\text{V}^{2+}/\text{V}^{3+}$ ^[3, 4], respectively. Unlike other types of redox flow batteries, the VRFBs only involves redox reactions with one single metal

with various valence states, which prevents a fast electrolyte degradation from cross-contamination of the solutions of both half cells.

It is obvious that the electrodes play a crucial role in catalysing redox reactions involved in electrochemical energy conversion [5, 6]. For VRFBs, carbon-based electrodes based on graphite felts [7] meet most requirements including high electrical conductivity (at least under compression), availability and price [8, 9]. However, it was also shown that the standard electrode material, carbon felt/carbon nonwoven, has to be activated in order to provide an acceptable catalytic activity for vanadium ion redox conversion [10], and even in this case further improvement is desired. Thus, recent research focusses on the investigation of catalytically active carbon material, such as carbon fibers [11], carbon nanotubes [12-14] mesoporous carbon [2, 15], carbon nanospheres [16], and more.

Besides the active electrode material itself, the substrate electrode onto which this material is deposited also requires attention. In particular, long term stability, appropriate flow-through properties as well as high conductivity are desired. One aim of this study is therefore to extend the possible substrates for the deposition of active material for possible application in VRFB and other electrochemical devices. In particular, titanium, which is electrochemically stable under the strong corrosive environment of a VRFB and provides very good electrical conductivity, has been used as substrate for nitrogen-doped carbon nanotubes (NCNTs). To provide good electrical contact and adhesion of the NCNTs, they were directly grown onto the substrate using chemical vapour deposition (CVD) yielding high-surface-area composite electrodes with tuneable properties [17, 18].

In particular, two different substrates were chosen, i.e. Ti foil and Ti mesh. NCNTs were grown over electrochemically deposited iron particles in a low-temperature (600 °C) CVD step. The thus obtained composite electrodes demonstrate good activity for vanadium ion redox reactions.

3.2 Methods

3.2.1 Synthesis of nitrogen-doped carbon nanotubes on the titanium substrate

Electrodeposition of Fe particles was carried out in a plating bath containing $\text{FeSO}_4 \cdot 7\text{H}_2\text{O}$ (0.01 M), Na_2SO_4 (0.1 M), and L-(+)-Ascorbic acid (0.3 M), in a three-electrode setup using pristine annealed Ti foil (Alfa) or Ti mesh (99.8%, pore diameter: 180 μm , wire diameter: 100 μm , OFOLAN, China) with a size of $1 \times 1 \text{ cm}^2$ as the working electrode (WE). A saturated calomel (SCE) was used as reference electrode (RE) and a Pt mesh as counter electrode (CE) at $25 \pm 3 \text{ }^\circ\text{C}$. Initially, iron deposition was attempted by double pulse deposition, as reported in [19]. However, it turned out that this approach did not yield satisfactory results, probably due to the nature of the Ti substrate, which seems to be covered by a small oxidic layer (see below). Thus, a potential program as shown in Figure 1a was established in a series of experiments, and justified by the fact that beneficial results were obtained. After Fe deposition, the Ti support decorated with Fe particles was placed into an APCVD (atmospheric pressure CVD) reactor and the quartz reactor tube (outer diameter, ca. 33.5 mm) inserted in an oven (Carbolite, Neuhausen, Germany) was purged with argon (Ar) flowing at 50 sccm for about 30 min. Further, the temperature of the growth chamber was ramped up to $600 \text{ }^\circ\text{C}$ under a gas flow rate of $\text{Ar}:\text{H}_2 = 50 \text{ sccm}:50 \text{ sccm}$ and kept there for 30 min. During the following growth step, the gas was saturated with acetonitrile (ACN) using a bubbler at $30 \text{ }^\circ\text{C}$. Finally, the system was cooled down under 50 sccm Ar after the specified growth time as detailed below.

3.2.2 Electrochemical performance

The electrochemical performance of the prepared NCNTs@Ti composite electrodes toward the positive redox reaction of the vanadium RFB (i.e., the $\text{VO}^{2+}/\text{VO}_2^+$ redox couple) was studied by cyclic voltammetry (CV). CV was carried out in a standard three-electrode cell containing 50 mL of 0.1M vanadium (IV) solution in a 3 M sulfuric acid using an Autolab potentiostat/galvanostat PGstat 302 (Eco Chemie Netherlands). CVs were obtained with a sweep rate of 50 mV s^{-1} at room temperature. The NCNTs@Ti composite served as the WE, and the area of both NCNTs@Ti foil and NCNTs@Ti mesh were defined to be $1 \times 1 \text{ cm}^2$. The CE was a Pt mesh, and the RE was a saturated mercury sulfate electrode ($\text{Hg}|\text{HgSO}_4|\text{K}_2\text{SO}_4(\text{sat.})$, MSE).

3.2.3 Physical characterization

Raman spectra were recorded on a Renishaw InVia instrument using a Cobolt CW DPPS laser (532 nm excitation wavelength), a Peltier cooled charge coupled device detector (CCD) with a grating of 1800 l mm^{-1} and a microscope (Leica, x100 objective). To evaluate homogeneity of the samples, a Raman mapping experiment was performed using a x-y stage (Prior, 100 nm resolution) in 500 nm steps scanning areas of $10 \times 10 \text{ }\mu\text{m}^2$.

X-ray photoelectron spectroscopy (XPS) was performed using monochromatic Al K α radiation as the excitation source. Survey spectra in a wide binding energy range were gained with a step size of 1 eV, while high-resolution spectra for C 1s, N 1s, and O 1s were attained with a step size of 0.1 eV and a dwell time of 50 ms, where the scan times were increased (50 scans) to achieve a reasonable signal-to-noise ratio. To compensate charging effects, all spectra were calibrated with respect to the C 1s peak at 284.9 eV. Spectra were fitted with the Casa XPS program.

The morphology of electrodeposited Fe particles as well as of NCNTs@Ti was investigated via scanning electron microscopy (SEM) using an ESEM XI 30 FEG (PHILIPS, Germany). The energy-dispersive X-ray spectroscopy (EDX) measurements were performed using an Octane elite plus detector. The measurement conditions were 5 kV accelerating voltage and 50 s measurement time (live time).

3.3 Results and Discussion

3.3.1 Iron electrodeposition

Iron particles were potentiostatically deposited onto both Ti substrates using a potential sequence as shown in Figure 1(a). The classical double pulse deposition approach using a short nucleation pulse to form nuclei on the substrate surface and a longer growth pulse to grow the nuclei into clusters did not yield uniform and homogeneous coverage of the Ti surfaces, thus a considerably long initial polarisation ($t_1 = 60 - 120 \text{ s}$) to a rather negative potential was necessary. We tentatively attribute this to the presence of a thin oxide layer covering the Ti substrate. After optimising the deposition times, dense coverage of the Ti substrate was obtained, as shown in Figure 1. Further optimisation of the deposition procedure (e.g., also varying the deposition potential etc.) was beyond the scope of this paper. The images obtained with SEM

shown in Figures 1 (b–d) for Ti foil and (e–g) for Ti mesh demonstrate the effect of varying t_1 on the dispersion and size of the Fe particles

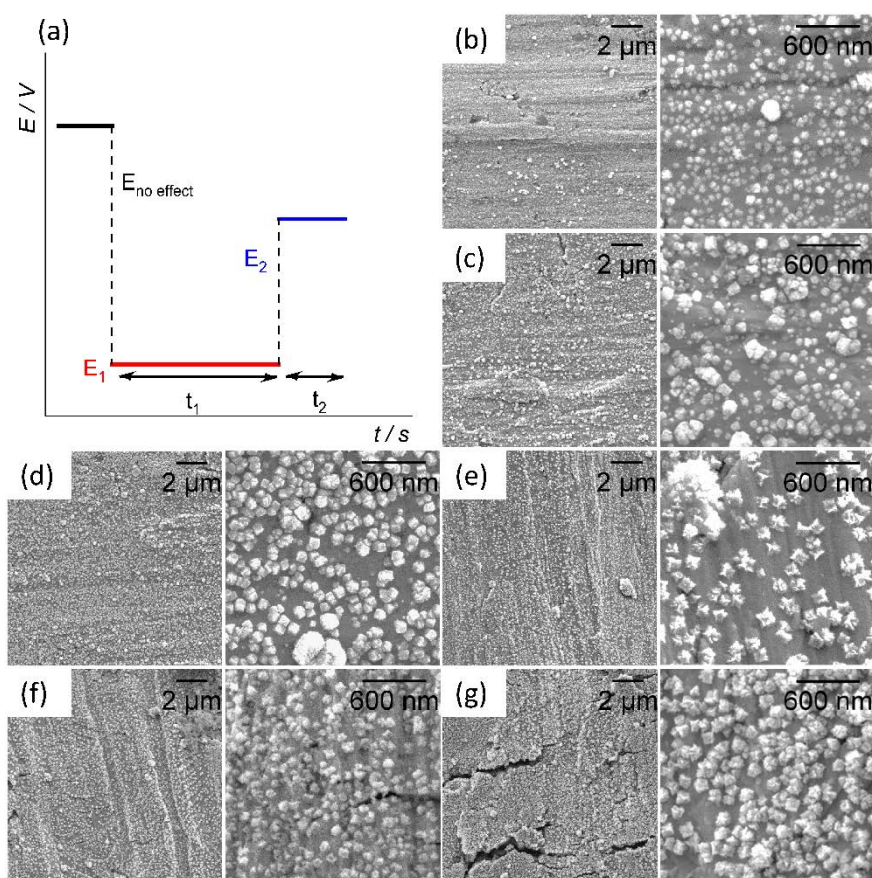


Figure 1. Electrodeposition process and morphological changes of Fe particles on Ti substrates. (a) Schematic representation of the electrodeposition potential profile. $E_1 = -3\ \text{V}$, $E_2 = -0.7\ \text{V}$, t_1 : nucleation time, t_2 : growth time. SEM images of as-deposited Fe particles on: (b–d) Ti foil, and (e–g) Ti mesh, showing the effect of t_1 , (b,e) 60 s, (c,f) 90 s and (d,g) 120 s, $t_2 = 10\ \text{s}$.

when t_2 was set to 10 s. Increasing coverage as well as particle sizes are observed with increasing deposition time. When the t_1 is maintained for 60 s, still incomplete coverage may be observed in particular in case of the Ti mesh (Figure 1e), while at deposition times of $t_1 = 120\ \text{s}$ the individual particles start to coalesce to larger ones (Figures 1d and 1g). Homogeneous and rather uniform as well as individual Fe particles are detected at $t_1 = 90\ \text{s}$ in both cases.

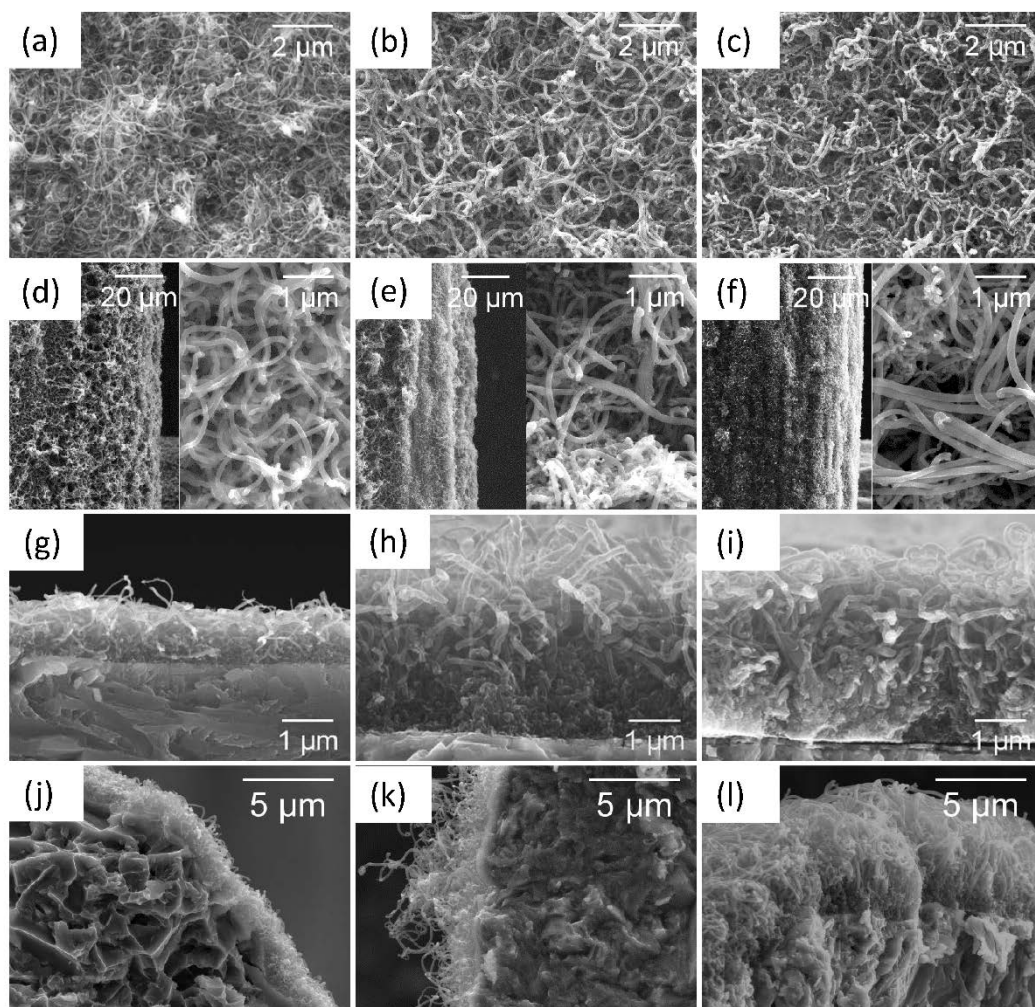


Figure 2. SEM micrographs of NCNTs on: (a–c) Ti foil, and (d–f) Ti mesh showing the effect of t_1 . (a,d) $t_1 = 60$ s, (b,e) $t_1 = 90$ s, and (c,f) $t_1 = 120$ s, $t_2 = 10$ s. The growth time (t_G) is 90 min, the substrate temperature is 600°C. SEM micrographs of NCNTs on: (g–i) Ti foil, and (j–l) Ti mesh showing the effect of t_G . (g,j) $t_G = 60$ min, (h, k) $t_G = 90$ min, and (i, l) $t_G = 120$ min (Fe electrodeposition in all cases with $t_1 = 90$ s and $t_2 = 10$ s).

3.3.2 NCNT characterisation

NCNTs were grown over electrodeposited iron particles as detailed in the experimental section and were characterized with SEM/EDX, Raman spectroscopy and XPS. SEM images of the grown NCNTs under variation of electrodeposition and growth time are shown in Figure 2. From Figures 2a–c (Ti foil) and Figures 2d–f (Ti mesh), one can see that dense NCNT layers are grown over the samples prepared with varying deposition time. However, comparing the inset of Figure 2d with those of Figures 2e and f, it

appears that after $t_1 = 60$ s the NCNT layer is still rather open and full and dense coverage is only obtained after $t_1 = 90$ s, indicating that the coverage with Fe particles is insufficient at the $t_1 = 60$ s, in agreement with Figures 1(e). Both Ti foil and Ti mesh are completely covered with the NCNTs when t_1 is increased to 90 s, while the NCNTs layer seems to be even more dense and inhomogeneous when the electrodeposition time is increased to 120 s. Combining the results from Figure 1 and Figure 2, $t_1 = 90$ s has been chosen as deposition time for further experiments, as the homogeneous Fe deposition leads to a homogeneous but still open 3-dimensional NCNTs layer. To further tune the properties of the 3D-NCNTs layers on the Ti substrates, the growth time (t_G) has been varied, using 60, 90 and 120 min. Results NCNTs grown over Ti foil are shown in Figures 2 (g–i), while those for the Ti mesh are displayed in Figures 2 (j–l). As expected, the thickness of the layers increases with growth time on both substrates. When carbon nanomaterials are grown on Cu [20, 21], Ni [22], or Fe [23] by CVD, a metal-C layer is commonly detected which is attributed to the dissolution of C into these metals leading to the formation of a new thin interface layer under various temperatures. To gain more insight into the interface between NCNT layer and substrate, detailed SEM/energy-dispersive X-ray spectroscopy (EDX) measurements were carried out. The backscattered electrons (BSE) cross-view SEM images of the interface between Ti mesh and NCNTs are shown in Figure 3a. EDX measured on the Ti mesh (black), the interface (blue) and the NCNTs (red) is displayed as in Figure 3b with the investigated areas marked in the figure with the same colors. The spectra show peaks corresponding to carbon at 0.27 keV, nitrogen at 0.38 keV, Ti at 0.39 and 0.45 keV, and oxygen at 0.52 keV. Iron (at 0.66 keV) however is below the limit of detection. Obviously, the Ti mesh essentially consists of Ti and a small amount of O, while the interface seems to consist mainly of TiO_2 as concluded from the intense oxygen signal. The NCNT layer demonstrates the expected signals of C and N, while also O can be found (see also below, XPS analysis).

To evaluate the structural properties of carbon materials, often Raman spectroscopy is the method of choice. Typically, the D, G, and 2D bands at ca. 1341, 1588, and 2682 cm^{-1} [19,20] are analyzed and the intensity ratio of the D to G band (I_D/I_G) is commonly used as an estimate of the quality of sp^2 carbon material, e.g. NCNTs. The respective Raman spectra shown in Figure 4a indicate that the quality/amount of defects in NCNTs grown on Ti-foil and Ti-mesh, respectively, is comparable, with only

a minor influence of the substrate on their properties. Furthermore, to evaluate the homogeneity of the grown NCNT layer, Raman mappings have been performed. Figure 4b visualizes a statistical evaluation of the Raman mapping experiment with mean value as solid line and standard deviation as grey shadow from 178 single spectra. The mean I_D/I_G intensity is about 0.86 ± 0.02 for NCNTs grown on a Ti foil ($t_1 = 90$ s and $t_G = 90$ min) with very low standard

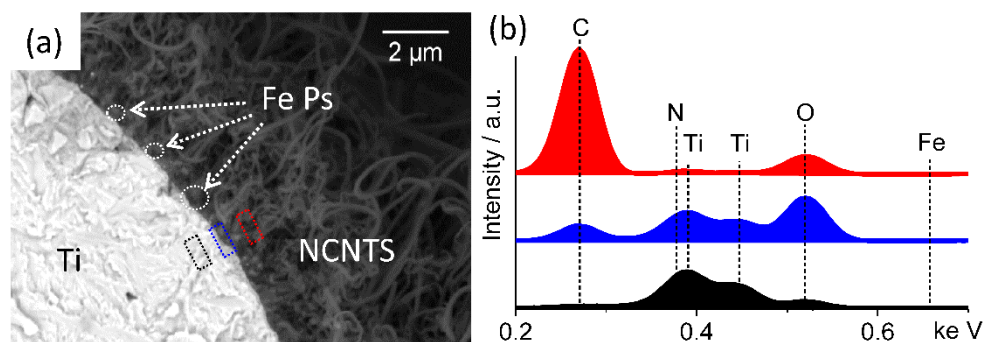


Figure 3. SEM-BSE micrographs of: (a) As-grown NCNTs on Ti mesh. (b) EDX analysis along area marked in black, blue, and red in Figure 3a. $t_1 = 90$ s, $t_2 = 10$ s. $t_G = 90$ min, $T_S = 600$ °C.

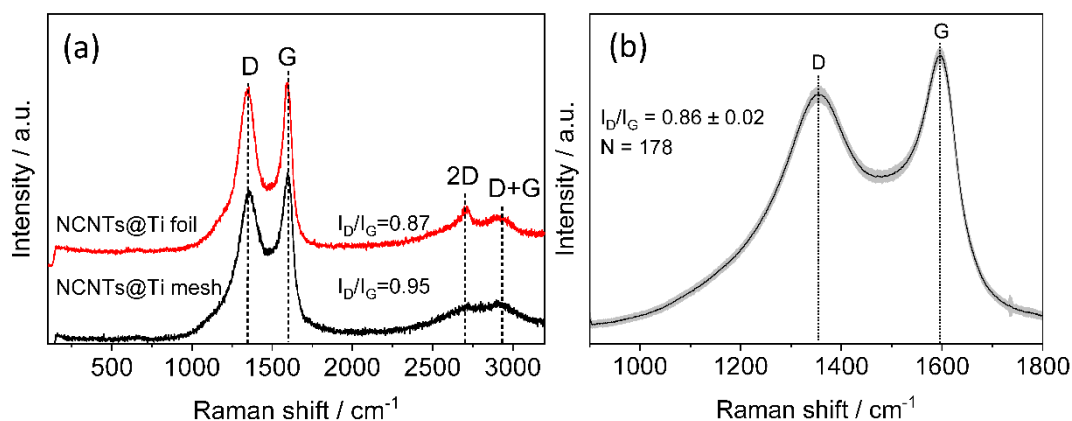


Figure 4. (a) Raman spectra of NCNTs on Ti foil and Ti mesh after testing electrochemical performance. (b) Statistical evaluation of the Raman mapping experiment with mean value and standard deviation (grey shadow) from 178 single spectra of NCNTs on Ti foil. $t_1 = 90$ s, $t_2 = 10$ s. $t_G = 90$ min, $T_S = 600$ °C.

deviation, implying that the NCNTs are grown rather homogeneously on the Ti foil. Furthermore, in the Raman spectra of Figure 4a the characteristic radial breathing

model (RBM) at ca. 160–290 cm^{-1} [21,22] is not visible, indicating that the NCNTs indeed are multi-walled, as expected.

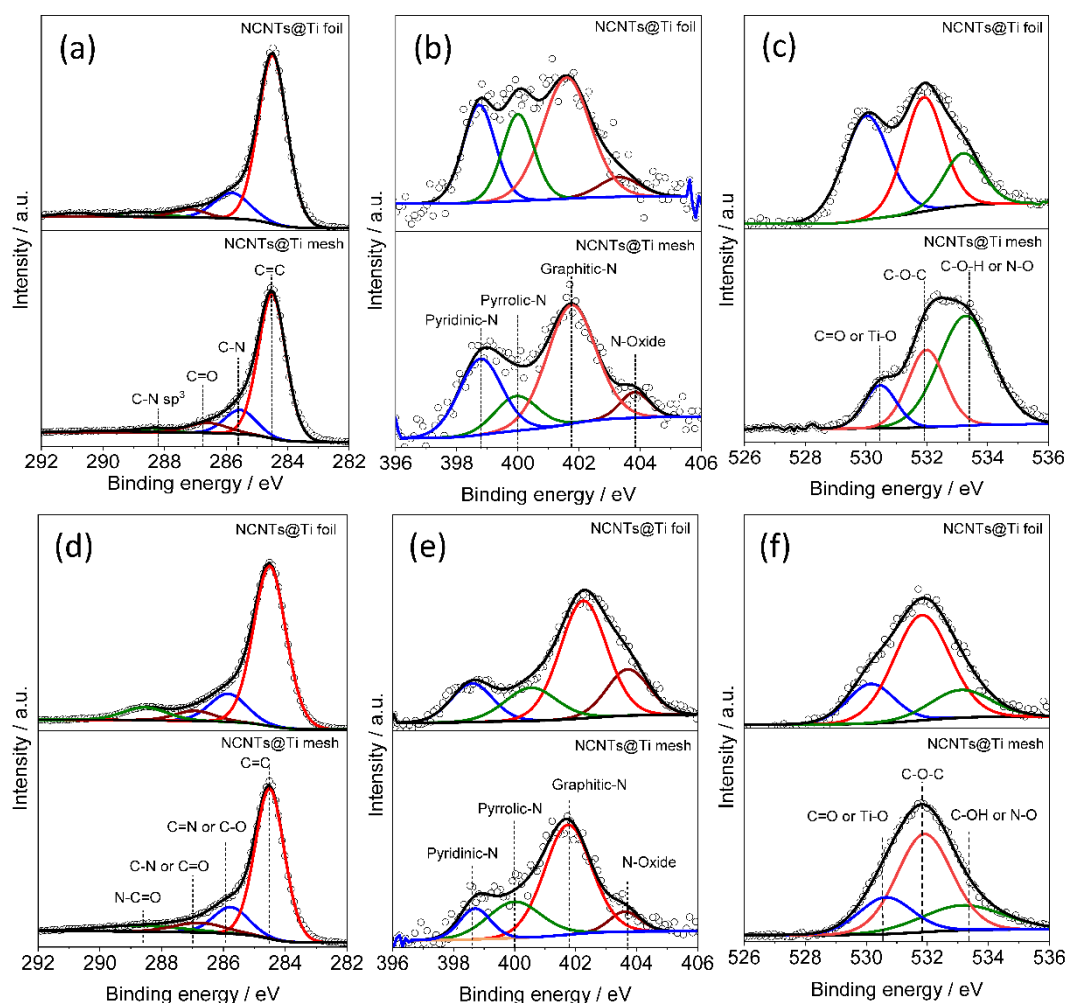


Figure 5. XPS high-resolution spectra of NCNTs on Ti foil and Ti mesh. (a) C 1 s, (b) N 1 s, and (c) O 1 s before testing electrochemical performance. (d) C 1 s, (e) N 1 s, and (f) O 1 s after testing electrochemical performance. The $t_1 = 90$ s, $t_2 = 10$ s, $t_G = 90$ min, $T_S = 600$ °C.

X-ray photoelectron spectroscopy has been used to analyze the chemical composition of the NCNTs grown over Ti foil and Ti mesh. The XP survey spectra show the C 1s peak at 285 eV, the O 1s peak at 532 eV, the N 1s peak at 402 eV, and Ti 2p peak at 459 eV, as summarized in Table 1. As Fe was not detected we assume that the electrodeposited particles are covered by the NCNTs on the Ti substrate.

The corresponding XPS high-resolution C 1s, N 1s, and O 1s spectra are shown in Figure 5. The C 1s spectra can be fitted with four peaks at 284.5 eV, 285.9 eV, 286.9 eV, and 288.5 eV, which can be assigned to C=C, C=N or C–O, C=O or C–N, and N–C=O species [2]. The four peaks observed in the N 1s spectra at 398.7, 400.5, 402.3, and 404.4 eV are commonly ascribed to pyridinic N, pyrrolic N, graphitic N (g-N), and oxide N [24, 25], respectively, while the high-resolution spectrum of O 1s with peaks at 530.9 eV, 533.1 eV, and 534.5 eV indicate the presence C=O or Ti–O [26], C–O–C, and C–O–H or N–O species [27, 28]. Since no oxygen is present during NCNT synthesis, it may be assumed that oxygen functional groups form post synthesis during handling of the NCNTs composites in air. It is worth noting that a relatively high amount of graphitic N can be found in the synthesised NCNTs over Ti substrates, which may be attributed to the low synthesis temperature of 600 °C.

In general, the structural characterization in this chapter proves the successful and homogeneous growth of dense layers of NCNTs over Fe particles electrodeposited on Ti foil and Ti mesh.

Sample	C 1s (at%)	O 1s (at%)	N 1s (at%)	Ti 2p (at%)	Fe (at%)
Ti foil	94.1	2.1	3.8	< LOD	< LOD
Ti foil_CV	68.6	25.1	4.9	1.4	< LOD*
Ti mesh	93.6	3.0	3.4	< LOD	< LOD
Ti mesh_CV	85.6	11.3	3.1	< LOD	< LOD*

Table 1. Surface atomic composition of the NCNTs derived from XPS for characteristic binding energies of C 1s (285 eV), O 1s (532 eV), N 1s (402 eV), Ti 2p (459 eV) and Fe 2p (714 eV) before and after testing CV measurements (* LOD – limit of detection, here ~0.5 at).

3.3.3 Electrochemical results

The electrochemical behaviour of NCNTs@Ti towards the V(IV)/V(V) redox pair, which is one relevant reaction in a VRFB, was analysed by cyclic voltammetry. Figure 6 compares the voltammograms of both NCNTs@Ti foil and NCNTs@Ti mesh for different deposition times of iron as well as different NCNTs growth times. The anodic peaks at about 0.5 V correspond to the oxidation VO_2^+ , while the cathodic peaks at about 0.3 V can be assigned to the reduction of VO_2^+ . The redox peaks at ca. 0.03 V and -0.1 V shown in Figures 6 (b) and (d), respectively, correspond to the V(III)/V(IV) redox couple [12, 29]. This redox couple is not of relevance in a running VRFB and will not be discussed further in this study. However, a pronounced V(III)/V(IV) redox activity might be helpful for the initial pre-charging process when applying commercial electrolytes typically containing a V(III):V(IV) ratio of 1:1 as vanadium source in the VRFB.

Peak current density (j_{pa} and j_{pc}), peak potential difference (ΔE_p), as well as the redox onset potentials are a common measure to estimate the catalytic activity of electrode materials [13, 30]. However, on the other hand it has recently been shown, that at least in case of porous electrodes, these values may not necessarily reflect activity, but may also be influenced by porosity, surface area, double layer capacity, etc. [2, 31]. To overcome this challenge, we have recently developed an SECM (scanning electrochemical microscope) procedure [14], which however is difficult to apply to the present 3-dimensional samples. Thus we restrict ourselves to a qualitative discussion of the electrochemical results. First of all, from Figure 6 it is obviously neither Ti foil nor Ti mesh provides significant redox activity towards the V(IV)/V(V) redox pair, making them suitable substrates for the investigation of carbon-based materials towards the given reaction. Moreover, in the case of NCNTs@Ti foil, the values of ΔE_p at 50 mV s^{-1} are 0.16, 0.13 and 0.19 V when t_1 was set to 60, 90, and 120 s, respectively, while in the case of NCNTs@Ti mesh, the values of ΔE_p are 0.28, 0.20, and 0.33 V, demonstrating that the prepared electrodes provide good redox activity. A slight influence of the iron deposition time is observed with 90 s in both cases as shown in Figures 6 (a) and (b), providing the highest current densities and the lowest peak potential differences. This is in agreement with the results from characterisation, where these samples showed dense coverage with NCNTs but no overgrowth. We assume that the fact that the peak separation in case of Ti foil is smaller does not indicate higher catalytic activity but is due to the highly porous nature of the Ti mesh, thus

diffusion within the porous network becomes relevant for CV shape. Accordingly, owing to the three-dimensional structure of the Ti mesh, a ten-fold current density (related to geometrical surface area) was achieved compared to the Ti foil.

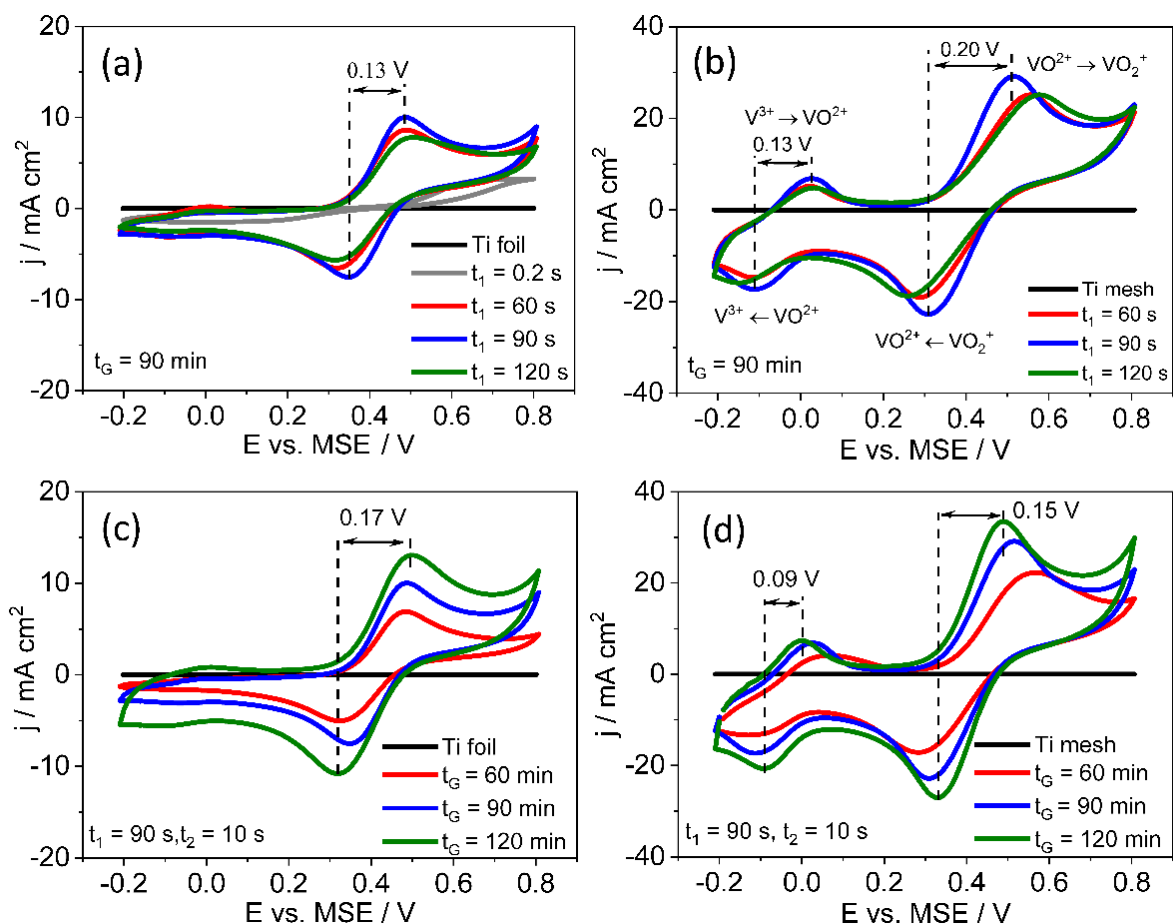


Figure 6. Electrochemical properties of NCNTs on Ti foil and Ti mesh with a scan rate of 50 mV s^{-1} . The fifth cycle is recorded (a) Ti foil and (b) Ti mesh substrates showing the effect of various nucleation times, $t_2 = 10 \text{ s}$, $t_G = 90 \text{ min}$. (c) Ti foil and (d) Ti mesh substrates showing the effect of t_G , $T_s = 600 \text{ }^\circ\text{C}$, $t_1 = 90 \text{ s}$, $t_2 = 10 \text{ s}$.

In Figures 6c and 6d, the cyclic voltammograms of the various samples prepared at different CVD growth times are summarised, exhibiting an increase in peak current densities with growth time and, in case of the Ti mesh, a decrease in the ΔE_p value. The enhancement in current densities is attributed to the increase in the thickness of NCNTs layers on the Ti surface, as shown in Figure 2(g–i) and (j–l). The best performance was obtained on NCNTs@Ti mesh at t_G of 120 min, with the highest j_{pa}

and j_{pc} , the lowest ΔE_p value (0.15 V), indicating promising activity toward the $[VO]^{2+}/[VO_2]^+$ redox couple of VRFB.

Recently, there has been a debate as to which surface structural features in carbon materials form the active sites for redox ion conversion. We have shown that oxygen functional groups seem not to be directly involved but the increased hydrophilicity introduced by them leads to increased wetting and thus to enhanced accessibility of the surface for vanadium redox species [2, 32]. Accordingly, nitrogen doping may influence the surface properties of the 3-dimensional electrodes leading to complete wetting and good activity.

3.4 Conclusion

In this study, Ti foil and Ti mesh were investigated as composite electrodes for VRFB. The catalyst was grown on these materials via the atmospheric pressure chemical vapor deposition. The time-dependent processing parameter was employed scrupulously to tailor the coverage of iron particles and to enhance the number of active sites as well. Furthermore, the peak current density of redox reaction was remarkably improved to about 35 mA cm^{-1} with the lowest ΔE_p value (0.15 V) for NCNTs@Ti-mesh composite compared to the original Ti-foil. The effect of isolated NCNTs on the electrochemical activity of the $[VO]^{2+}/[VO_2]^+$ couple of VRFB was first investigated. By the electron-withdrawing effect of doping nitrogen atom in NCNTs, the stable group of g-N could be the significant active centre to facilitate the redox reaction in strong acidic electrolyte. Finally, it proposes a feasible method to study the catalytic performance of isolated catalyst and composite material catalyst for energy storage systems.

3.5 Reference

- [1] P. Leung, X. Li, C. Ponce de León, L. Berlouis, C.T.J. Low, F.C. Walsh, Progress in redox flow batteries, remaining challenges and their applications in energy storage, RSC Adv., 2 (2012) 10125-10156.
- [2] S. Rummler, M. Steimecke, S. Schimpf, M. Hartmann, S. Forster, M. Bron, Highly Graphitic, Mesoporous Carbon Materials as Electrocatalysts for Vanadium Redox Reactions in All-Vanadium Redox-Flow Batteries, J. Electrochem. Soc., 165 (2018) A2510-A2518.

- [3] M. Rychcik, M. Skyllas-Kazacos, Characteristics of a New All-Vanadium Redox Flow Battery, *J. Power Sources*, 22 (1988) 59-67.
- [4] F. Rahman, M. Skyllas-Kazacos, Vanadium redox battery: Positive half-cell electrolyte studies, *J. Power Sources*, 189 (2009) 1212-1219.
- [5] C. Ding, H. Zhang, X. Li, T. Liu, F. Xing, Vanadium flow battery for energy storage: prospects and challenges, *J. Phys. Chem. Lett.*, 4 (2013) 1281-1294.
- [6] M. Park, J. Ryu, J. Cho, Nanostructured electrocatalysts for all-vanadium redox flow batteries, *Chem. Asian J.*, 10 (2015) 2096-2110.
- [7] T.M. Tseng, R.H. Huang, C.Y. Huang, C.C. Liu, K.L. Hsueh, F.S. Shieu, Carbon Felt Coated with Titanium Dioxide/Carbon Black Composite as Negative Electrode for Vanadium Redox Flow Battery, *J. Electrochem. Soc.*, 161 (2014) A1132-A1138.
- [8] K.J. Kim, M.S. Park, Y.J. Kim, J.H. Kim, S.X. Dou, M. Skyllas-Kazacos, A technology review of electrodes and reaction mechanisms in vanadium redox flow batteries, *J. Mater. Chem. A*, 3 (2015) 16913-16933.
- [9] Z. González, C. Botas, C. Blanco, R. Santamaría, M. Granda, P. Álvarez, R. Menéndez, Thermally reduced graphite and graphene oxides in VRFBs, *Nano Energy*, 2 (2013) 1322-1328.
- [10] Y. Kim, Y.Y. Choi, N. Yun, M. Yang, Y. Jeon, K.J. Kim, J.-I. Choi, Activity gradient carbon felt electrodes for vanadium redox flow batteries, *J. Power Sources*, 408 (2018) 128-135.
- [11] W. Li, Z. Zhang, Y. Tang, H. Bian, T.W. Ng, W. Zhang, C.S. Lee, Graphene-nanowall-decorated carbon felt with excellent electrochemical activity toward $\text{VO}^{2+}/\text{VO}_2^+$ couple for all vanadium redox flow battery, *Adv. Sci.*, 3 (2016) 1500276-1500283.
- [12] M. Steimecke, S. Rümmler, N.-F. Schuhmacher, T. Lindenberg, M. Hartmann, M. Bron, A Comparative Study of Functionalized High-Purity Carbon Nanotubes towards the V(IV)/V(V) Redox Reaction Using Cyclic Voltammetry and Scanning Electrochemical Microscopy, *Electroanal.*, 29 (2017) 1056-1061.
- [13] C. Noh, S. Moon, Y. Chung, Y. Kwon, Chelating functional group attached to carbon nanotubes prepared for performance enhancement of vanadium redox flow battery, *J. Mater. Chem. A*, 5 (2017) 21334-21342.
- [14] M. Steimecke, S. Rümmler, M. Kühhirt, M. Bron, A Linear Sweep Voltammetric Procedure Applied to Scanning Electrochemical Microscopy for the Characterization of Carbon Materials towards the Vanadium(IV)/(V) Redox System, *ChemElectroChem*, 3 (2016) 318-322.

- [15] J. Melke, P. Jakes, J. Langner, L. Riekehr, U. Kunz, Z. Zhao Karger, A. Nefedov, H. Sezen, C. Wöll, H. Ehrenberg, C. Roth, Carbon materials for the positive electrode in all-vanadium redox flow batteries, *Carbon*, 78 (2014) 220-230.
- [16] L. Wu, Y. Shen, L. Yu, J. Xi, X. Qiu, Boosting vanadium flow battery performance by Nitrogen-doped carbon nanospheres electrocatalyst, *Nano Energy*, 28 (2016) 19-28.
- [17] P. Wang, T. Kottakkat, M. Bron, Pt supported on Nanostructured NCNTs/RGO Composite Electrodes for Methanol Electrooxidation, *ChemElectroChem*, 2 (2015) 1396-1402.
- [18] S. Kundu, T.C. Nagaiah, X. Chen, W. Xia, M. Bron, W. Schuhmann, M. Muhler, Synthesis of an improved hierarchical carbon-fiber composite as a catalyst support for platinum and its application in electrocatalysis, *Carbon*, 50 (2012) 4534-4542.
- [19] M. Uedaa, H. Dietz, A. Anders, H. Knepe, A. Meixner, W. Plieth, Double-pulse technique as an electrochemical tool for controlling the preparation of metallic nanoparticles, *Electrochimica Acta*, 48 (2002) 377-386.
- [20] X. Li, W. Cai, J. An, S. Kim, J. Nah, D. Yang, R. Piner, A. Velamakanni, I. Jung, E. Tutuc, S.K. Banerjee, L. Colombo, R.S. Ruoff, Large-area synthesis of high-quality and uniform graphene films on copper foils, *Science*, 324 (2009) 1312-1314.
- [21] I. Vlassioux, S. Smirnov, M. Regmi, S.P. Surwade, N. Srivastava, R. Feenstra, G. Eres, C. Parish, N. Lavrik, P. Datskos, S. Dai, P. Fulvio, Graphene nucleation density on copper: fundamental role of background pressure, *J. Phys. Chem. C*, 117 (2013) 18919-18926.
- [22] L.L. Patera, F. Bianchini, C. Africh, C. Dri, G. Soldano, M.M. Mariscal, M. Peressi, G. Comelli, Real-time imaging of adatom-promoted graphene growth on nickel, *Science*, 359 (2018) 1243-1246.
- [23] Y. Xue, B. Wu, Y. Guo, L. Huang, L. Jiang, J. Chen, D. Geng, Y. Liu, W. Hu, G. Yu, Synthesis of large-area, few-layer graphene on iron foil by chemical vapor deposition, *Nano Res.*, 4 (2011) 1208-1214.
- [24] Y. Zhong, M. Jaidann, Y. Zhang, G. Zhang, H. Liu, M. Ioan Ionescu, R. Li, X. Sun, H. Abou Rachid, L.S. Lussier, Synthesis of high nitrogen doping of carbon nanotubes and modeling the stabilization of filled DAATO@CNTs (10,10) for nanoenergetic materials, *J. Phys. Chem. Solids*, 71 (2010) 134-139.
- [25] Z. Chen, D. Higgins, Z. Chen, Nitrogen doped carbon nanotubes and their impact on the oxygen reduction reaction in fuel cells, *Carbon*, 48 (2010) 3057-3065.

- [26] C.H. Kim, B.-H. Kim, K.S. Yang, TiO₂ nanoparticles loaded on graphene/carbon composite nanofibers by electrospinning for increased photocatalysis, *Carbon*, 50 (2012) 2472-2481.
- [27] Y.K. Kim, H. Park, Light-harvesting multi-walled carbon nanotubes and CdS hybrids: Application to photocatalytic hydrogen production from water, *Energy Environ. Sci.*, 4 (2011) 685-694.
- [28] S. Wu, G. Wen, J. Wang, J. Rong, B. Zong, R. Schlögl, D.S. Su, Nitrobenzene reduction catalyzed by carbon: does the reaction really belong to carbocatalysis?, *Catal. Sci. Technol.*, 4 (2014) 4183-4187.
- [29] H.-S. Kim, Electrochemical Properties of Graphite-based Electrodes for Redox Flow Batteries, *Bull. Korean Chem. Soc.*, 32 (2011) 571-575.
- [30] L. Eifert, Z. Jusys, R. Banerjee, R.J. Behm, R. Zeis, Differential electrochemical mass spectrometry of carbon felt electrodes for vanadium redox flow batteries, *ACS Appl. Energy Mater.*, 1 (2018) 6714-6718.
- [31] M. Steimecke, S. Rümmler, M. Bron, The effect of rapid functionalization on the structural and electrochemical properties of high-purity carbon nanotubes, *Electrochimica Acta*, 163 (2015) 1-8.
- [32] W. Zhang, J. Xi, Z. Li, H. Zhou, L. Liu, Z. Wu, X. Qiu, Electrochemical activation of graphite felt electrode for VO₂⁺/VO₂⁺ redox couple application, *Electrochimica Acta*, 89 (2013) 429-435.

The content of this chapter has been submitted for publication in Electrochemistry Communications as

Chapter 4 Nanocrystal Graphene, Graphene, and Nitrogen-doped Graphene Hybrid Electrode for Vanadium Redox Flow Battery Applications

Xubin Lu, Fan Li, Tariq Muhammad and Michael Bron

Abstract

The performances of nanocrystalline graphene, graphene, and nitrogen-doped graphene synthesized by atmospheric-pressure chemical vapour deposition are assessed for working electrodes in combination with titanium (Ti) towards the V(IV)/V(V) redox couple of a vanadium redox flow battery (VRFB). Raman spectroscopy, X-ray photoelectron spectroscopy, and Raman mapping analysis of the sp² carbon atoms provide insight into the physical features of these electrodes. Irreversible cyclic voltammetry of these electrode hybrids reveals remarkable electrochemical activity towards the V(IV)/V(V) redox pair compared with that of the bare Ti support. Furthermore, the electrochemical performance of individual two-dimensional (2D) sp² carbon nanomaterials could be effectively obtained with the hybrid electrodes herein owing to the fact that bare Ti is inert towards the V(IV)/V(V) redox couple reaction. Therefore, this represents a considerable basic study on two-dimensional carbon nanomaterials in VRFB.

4.1 Introduction

The VRFB is applied extensively in large-scale electrochemical energy storage systems since its chemistry is entirely based on vanadium ions at different valence states, and thus are free from cross-contamination problems [1, 2]. Indeed, VRFB has attracted increasing attention for its significant advantages, including long cycle life, simple yet flexible design, high capacity, high-energy efficiency, resistance to overloading, and low maintenance cost, which make it a promising large-scale power storage system [3]. The main energy conversion reactions in both half-cells of VRFB, a positive one $[\text{VO}]^{2+}/[\text{VO}_2]^+$ and a negative one $[\text{V}]^{2+}/[\text{V}]^{3+}$, occur mainly on the electrode surface, which plays a significant role in providing active sites for redox

reaction occurring in VRFB. Consequently, the current density and reaction efficiency strongly depend on the type, structure, and composition of electrode materials [4].

Numerous carbon materials, such as, graphite felts [5], carbon nanotubes [6] mesoporous carbon [7], and nitrogen-doped carbon nanotubes [8] have been used as catalytically active ingredients in VRFB. However, to date, the electrochemical activity of isolated sp^2 carbon nanomaterials have rarely been appropriately evaluated. This is mostly because of the presence of strongly acidic electrolytes excludes the application of less expensive materials. The previous report investigated the growth of nano-sized graphene islands on the cobalt (Co)(0001)_{hcp} surface [9]. Noteworthy, the transition temperature of crystalline titanium (Ti) from (α -Ti)_{hcp} to (β -Ti)_{bcc} [10] is 882 °C. It is therefore probably the control temperature to accomplish the synthesis of nano-sized graphene on the (α -Ti)_{hcp} support. Thus, it is interesting to evaluate a combination of high-activity sp^2 carbons with high-stable Ti substrate as a novel hybrid electrode for VRFB. Moreover, the electrochemical performance of isolated sp^2 carbon nanomaterial was identified in this study.

4.2 Methods

Electropolished copper foil (thickness 25 μm , 2 \times 8 cm^2) and Ti foil (Alfa aesar) (1 \times 2 cm^2) were annealed for 30 min under Ar and H₂ (20 sccm) before the next steps. For growth of graphene, the Cu foil was exposed to H₂ and CH₄ (H₂ : CH₄ = 20 sccm : 60 sccm) for 50 min when growth temperature was set at 1080°C. NG was carried out with a mixture of H₂ + Ar + acetonitrile (Roth, +99%) and maintained for 50 min (H₂ : Ar = 50 sccm : 50 sccm) under 800 °C. Synthesis of NCG, the Ti foil was exposed to H₂ + Ar + cyclohexane (Roth) (H₂ : Ar = 50 sccm : 50 sccm) under 800 °C. Finally, the substrate was cooled down room temperature under Ar (20 sccm). PMMA (4%) dissolved in anisole (Alfa Aesar) was used for transferring graphene or NG onto the Ti substrate [11].

Electrochemical performance was performed in a standard three-electrode cell containing 50 mL of 0.1 M [VO]²⁺/[VO₂]⁺ using an Autolab potentiostat/galvanostat PGstat 302 (Eco Chemie Netherlands) with a scan rate of 50 mV s⁻¹. The 1 \times 1 cm^2 G@Ti, NCG@Ti, and NG@Ti composites served as the WE, respectively. The CE

was a Pt mesh, and the RE was a saturated mercury sulfate electrode (Hg|HgSO₄|K₂SO₄(sat.), MSE).

Raman spectra were obtained on a Renishaw InVia instrument using Cobolt CW DPPS laser (532 nm excitation wavelength) and a Peltier cooled charge coupled device detector (CCD) with a grating of 1800 l mm⁻¹ and a microscope (Leica, x100 objective). X-ray diffraction (XRD) was carried out on a D8 advanced X-ray diffractometer from Bruker AXS using Cu K α radiation ($\lambda = 1.5406 \text{ \AA}$) and a step size of 0.013°. X-ray photoelectron spectroscopy (XPS) was carried out using an X-ray photoelectron spectrometer with monochromatic Al K α radiation (Kratos, Axis Ultra) and Omicron DAR 400 X-ray source with Al K α line (15 kV) and an EA 125X Hemispherical energy analyzer (Omicron).

4.3 Results and Discussion

Raman spectroscopy is a high-efficient approach to analyse the structural properties of two-dimensional (2D) sp² carbon materials. Typically, the D, G, and 2D bands at ca. 1360, 1600, and 2710 cm⁻¹ are analysed. A decreasing intensity ratio of the G to 2D band intensities (I_G/I_{2D}) is commonly considered a qualitative indicator for decreasing defect concentration of graphene. The representative Raman spectra of pristine graphene, NG, and NCG are shown in Figure 1a, which identify the quality of these samples. It is clear that the value of I_G/I_{2D} for the pristine graphene sample is less than 0.5 with a weak D band, which is a significant indicator for monolayer graphene^[12]. In the NG sample spectrum, the D' band (~1625 cm⁻¹) is the main characteristic peak of the NG spectrum, which is adjacent to the G band (~1600cm⁻¹). In the NCG sample spectrum, the D band is broadened compared with that of the NG sample, which is the result of the Ti peak at 1116 cm⁻¹ merging with the D band at 1360 cm⁻¹. With its large amount of edges, the NCG exhibits an insensitive defect band at 1360 cm⁻¹ as well as the G band at 1600 cm⁻¹.

Figure 1 b shows the Raman spectra of NCG as a function of various growth durations. The ratio of the D to G band intensities (I_D/I_G) decreases from 1.01 to 0.86 with increasing growth duration as the amorphous carbon transitions into NCG. With increasing NCG growth duration from 30 to 60 min, the I_D/I_G decreases to 0.72 and the intensities of the Ti peaks at 554 and 620 cm⁻¹^[13] decrease gradually. These

results indicate that graphite becomes dominant with further growth. Furthermore, the Raman mapping of I_D/I_G values on an area of the NCG sample grown for 30 min is shown in the inset of Figure 1b, where the I_D/I_G value primarily is ca. 0.96. This result implies that the graphene nanocrystalline size is about 20 nm for the NCG samples used in this study [14].

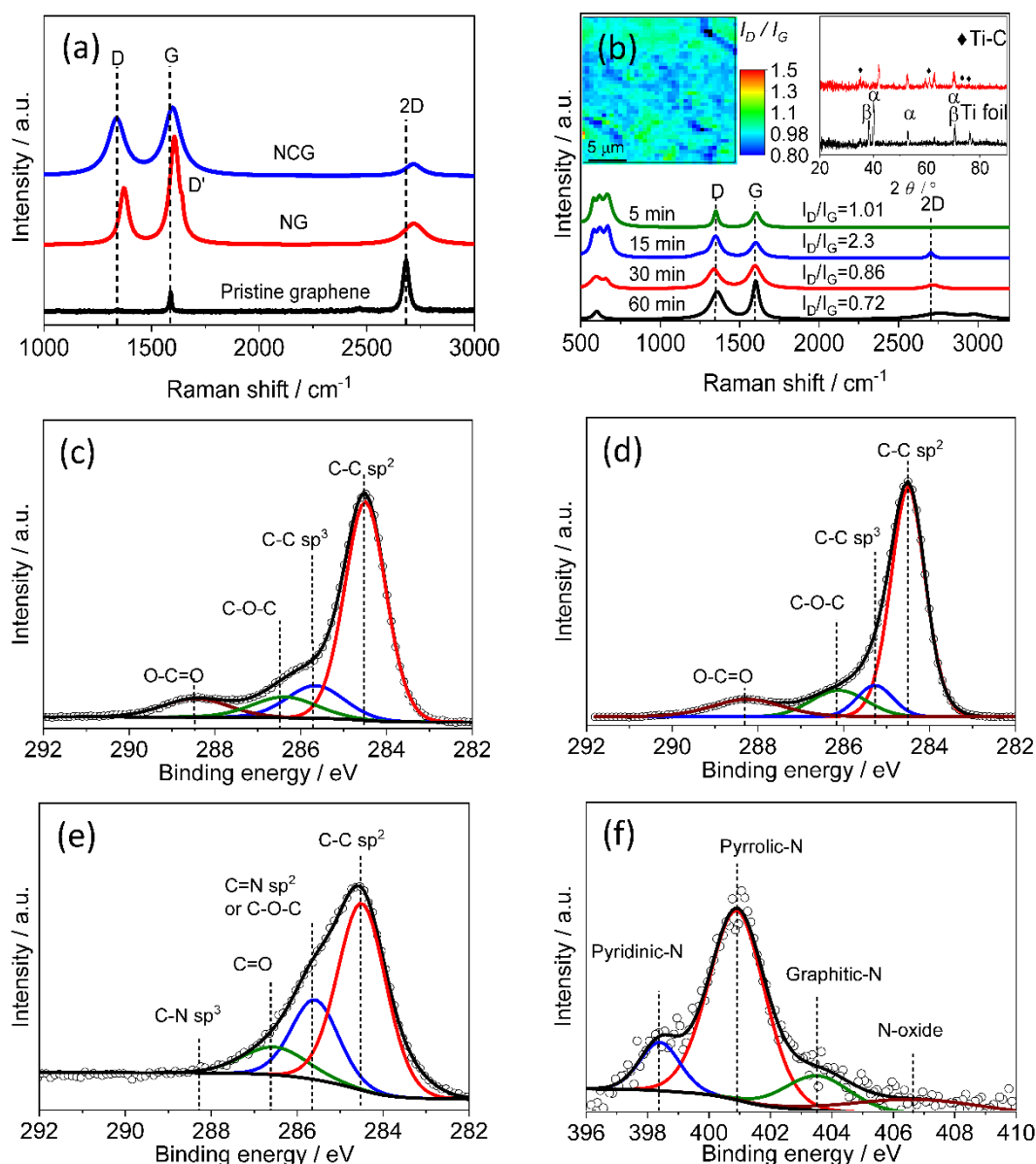


Figure 1. (a) Raman spectra of as-transferred pristine graphene on Ti foil, as-grown NG on Cu foil, and NCG on Ti sheet. (b) Raman spectra of NCG films grown for various durations. (c) Raman mapping of the D- and G-band peak intensity ratio (I_D/I_G) of NCG film on Ti substrate. (d) XRD pattern of NCG and Ti foil. XPS spectra of sp^2 carbon

materials. (c–e) High-resolution C 1s spectra of (c) NCG, (d) pristine graphene, and (e) NG. (f) High-resolution N 1s spectra of NG.

The XRD pattern of the NCG sample shown in the inset of Figure 1b exhibits the distinctive diffraction peaks corresponding to the Ti-C phase at 2θ values of 35.2° , 60.6° , 73.2° , and 76.9° , which are respectively attributed to the (110), (220), (311), and (222) diffraction planes. This XRD pattern can be contrasted with that of the Ti foil [15].

Figures 1c–e show the high-resolution C 1s XPS results for the NCG, graphene, and NG samples. The C 1s peaks of NCG and pristine graphene at 284.5, 285.5, 287.5, and 288.1 eV can be ascribed to the C=C (sp^2), C–C (sp^3), C–O–C, and O–C=O species, respectively. The C 1s peaks of NG (4.27 at%) at 285.6, 286.6, and 288.5 eV are respectively assigned to the C=N (sp^2), C=O, and C–N (sp^3) species. The broad N1s XPS peak of NG shown in Figure 1f can be fitted with four peaks at 398.7, 400.6, 401.8, and >403.6 eV, which are respectively assigned to the pyridinic-N, pyrrolic-N, and graphitic-N species and nitrogen oxide [7].

Figure 2 plots the voltammograms of the NCG@Ti, Graphene@Ti, and NG@Ti electrodes at $-0.2 - 1.5$ V. The anodic peaks at about 0.9 V can be ascribed to the oxidation of VO^{2+} to VO_2^+ [16]. However, the anodic electrochemical response on these 2D sp^2 carbon materials is an irreversible process, which suggests a relatively poor electrochemical activity of these samples towards the V(IV)/V(V) redox repair [17]. This finding is an excellent agreement with that reported regarding the irreversible electron transfer (ET) of graphite towards the aforementioned reaction [18].

Figure 2a indicates that there is a noticeable enhancement of the peak current density in the case of NCG@Ti electrode compared with the Ti electrode, which provides further proof that the NCG was grown directly on the Ti substrate. However, the electrochemical response of NCG is sluggish towards the V(IV)/V(V) redox repair, which can be mostly ascribed to the high defect density of NCG. This is consistent with the above characterisation. With high defect density, the scattering of the electrons results in a low conductivity, [19] and thus leading to lower ET of the VO^{2+} to VO_2^+ oxidation reaction. Additionally, the low conductivity mostly results from the low total sp^2 carbon content of NCG [20].

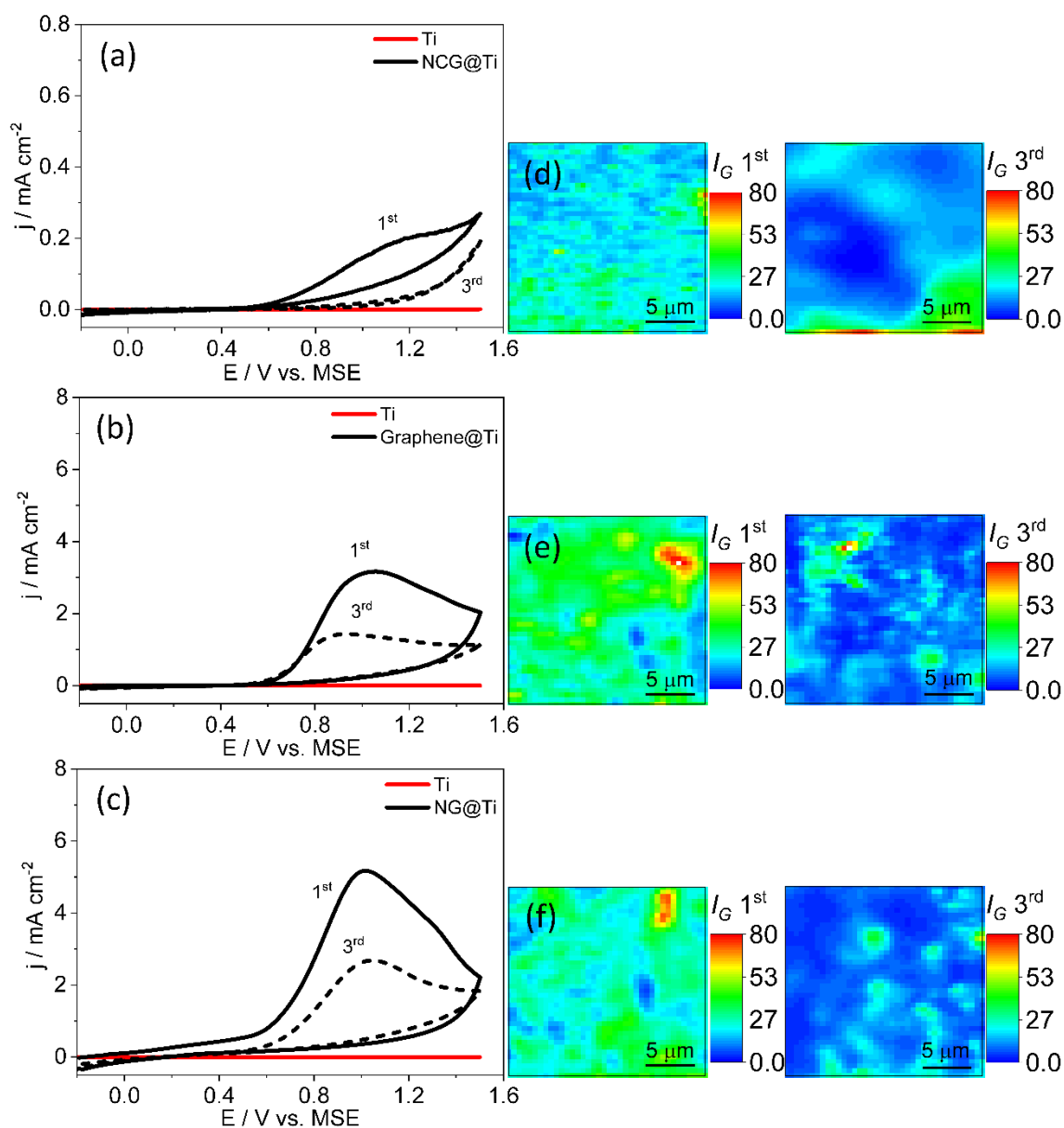


Figure 2. Electrochemical properties of electrode hybrids of (a) NCG@Ti, (b) graphene@Ti, and (c) NG@Ti electrode. Raman mapping of the G-band peak intensity (I_G) of (d) NCG, (e) graphene, and (f) NG on Ti substrate for the first (1st) and third (3rd) scanning.

The voltammograms of the Graphene@Ti and NG@Ti electrodes, shown in Figures 2b and 2c, exhibit their remarkable anodic peak current density of 3.5 and 5.2 mA cm⁻¹, respectively. These current density values are much greater than that of the NCG@Ti electrode, and are likely owing to a sufficient total quantity of sp² carbons present on the Graphene@Ti and NG@Ti electrodes. The high sp² carbon content and homogenous graphene domain shown in Figures 2e and 2f not only provide plentiful

adsorption sites but also enhance the conductivity of the VO^{2+} to VO_2^+ oxidation reaction [17, 20]. In particular, adsorption is commonly considered the rate-determining step among all catalytic processes [21]. Among these, abundant adsorption and high ET are dynamic prerequisites for subsequent processes that facilitate the $\text{VO}^{2+}/\text{VO}_2^+$ redox couple. The NG@Ti electrode possesses excellent electrochemical performance among these electrodes, which can be attributed to the strong electron-withdrawing effect of the heteroatom [22]. Raman mapping of the G-band intensity for sp^2 NCG, graphene, and NG on Ti substrate indicate that the decrease of sp^2 carbon content on the Ti surface after suffering the third scanning. It is reasonable that repeated sweeping would cause the oxidation peaks to drop severely with increasing cycle number for various electrodes.

4.4 Conclusion

In this study, Ti foil was investigated as a hybrid and supporting electrode for VRFB. Two-dimensional sp^2 carbon materials were employed to estimate their activity toward the $\text{VO}^{2+}/\text{VO}_2^+$ redox couple. The anodic current density exhibited remarkable three- to five-fold improvement for G@Ti, and NG@Ti electrodes, respectively, compared with the original Ti electrode. This investigation reveals the effect of NCG, pristine graphene, and NG on the electrochemical performance towards the $\text{VO}^{2+}/\text{VO}_2^+$ redox couple, which recommends an ingenious method to develop novel, stable, and highly-efficient electrodes for large-scale energy storage systems.

4.5 Reference

- [1] M. Rychcik, M. Skyllas-Kazacos, Characteristics of a New All-Vanadium Redox Flow Battery, *J. Power Sources*, 22 (1988) 59-67.
- [2] K.L. Huang, X.G. Li, S.Q. Liu, N. Tan, L.Q. Chen, Research progress of vanadium redox flow battery for energy storage in China, *Renewable Energy*, 33 (2008) 186-192.
- [3] P. Trogadas, O.O. Taiwo, B. Tjaden, T.P. Neville, S. Yun, J. Parrondo, V. Ramani, M.O. Coppens, D.J.L. Brett, P.R. Shearing, X-ray micro-tomography as a diagnostic tool for the electrode degradation in vanadium redox flow batteries, *Electrochem. Commun.*, 48 (2014) 155-159.

- [4] K.J. Kim, M.S. Park, Y.J. Kim, J.H. Kim, S.X. Dou, M. Skyllas-Kazacos, A technology review of electrodes and reaction mechanisms in vanadium redox flow batteries, *J. Mater. Chem. A*, 3 (2015) 16913-16933.
- [5] T.M. Tseng, R.H. Huang, C.Y. Huang, C.C. Liu, K.L. Hsueh, F.S. Shieu, Carbon Felt Coated with Titanium Dioxide/Carbon Black Composite as Negative Electrode for Vanadium Redox Flow Battery, *J. Electrochem. Soc.*, 161 (2014) A1132-A1138.
- [6] M. Steimecke, S. Rummler, N.-F. Schuhmacher, T. Lindenberg, M. Hartmann, M. Bron, A Comparative Study of Functionalized High-Purity Carbon Nanotubes towards the V(IV)/V(V) Redox Reaction Using Cyclic Voltammetry and Scanning Electrochemical Microscopy, *Electroanal.*, 29 (2017) 1056-1061.
- [7] S. Rummler, M. Steimecke, S. Schimpf, M. Hartmann, S. Forster, M. Bron, Highly Graphitic, Mesoporous Carbon Materials as Electrocatalysts for Vanadium Redox Reactions in All-Vanadium Redox-Flow Batteries, *J. Electrochem. Soc.*, 165 (2018) A2510-A2518.
- [8] S. Wang, X. Zhao, T. Cochell, A. Manthiram, Nitrogen-Doped Carbon Nanotube/Graphite Felts as Advanced Electrode Materials for Vanadium Redox Flow Batteries, *J. Phys. Chem. Lett.*, 3 (2012) 2164-2167.
- [9] D. Prezzi, D. Eom, K.T. Rim, H. Zhou, S. Xiao, C. Nuckolls, T.F. Heinz, G.W. Flynn, M.S. Hybertsen, Edge structures for nanoscale graphene islands on Co(0001) surfaces, *ACS Nano*, 8 (2014) 5765-5773.
- [10] S.F. Corbin, D. Cluff, Determining the rate of (β -Ti) decay and its influence on the sintering behavior of NiTi, *J. Alloys Compd.*, 487 (2009) 179-186.
- [11] C.D. Pinto, D. De, V.G. Hadjiev, H. Peng, AB-Stacked Multilayer Graphene Synthesized via Chemical Vapor Deposition: A Characterization by Hot Carrier Transport, *ACS Nano*, 6 (2012) 1142-1148.
- [12] Y.H. Kahng, S. Lee, M. Choe, G. Jo, W. Park, J. Yoon, W.K. Hong, C.H. Cho, B.H. Lee, T. Lee, A study of graphene films synthesized on nickel substrates: existence and origin of small-base-area peaks, *Nanotechnology*, 22 (2011) 045706.
- [13] K. Ullah, W.C. Oh, Fabrication of large size graphene and Ti- MWCNTs/ large size graphene composites: their photocatalytic properties and potential application, *Sci. Rep.*, 5 (2015) 14242.
- [14] A. Turchanin, D. Weber, M. Buenfeld, C. Kisielowski, M.V. Fistul, K.B. Efetov, T. Weimann, R. Stosch, J. Mayer, A. Golzhauser, Conversion of Self-Assembled

Monolayers into Nanocrystalline Graphene: Structure and Electric Transport, *ACS Nano*, 5 (2011) 3896-3904.

[15] J. Li, G. Wang, H. Geng, H. Zhu, M. Zhang, Z. Di, X. Liu, P.K. Chu, X. Wang, CVD Growth of Graphene on NiTi Alloy for Enhanced Biological Activity, *ACS Appl. Mater. Interfaces*, 7 (2015) 19876-19881.

[16] H. Liu, T. Cai, Q. Song, L. Yang, Q. Xu, C. Yan, Electrochemical Behavior of the Titanium Plate with Carbon Films in a Vanadium Sulfate Solution, *Int. J. Electrochem. Sci.*, 8 (2013) 2515-2523.

[17] Z.J. Jia, B.G. Wang, S.Q. Song, X. Chen, Effect of Polyhydroxy-Alcohol on the Electrochemical Behavior of the Positive Electrolyte for Vanadium Redox Flow Batteries, *J. Electrochem. Soc.*, 159 (2012) A843-A847.

[18] A. Habekost, Vanadium Redox Flow Batteries with Different Electrodes and Membranes, *J. Chem. Educ.*, 6 (2018) 8-13.

[19] J.H. Zhong, J. Zhang, X. Jin, J.Y. Liu, Q. Li, M.H. Li, W. Cai, D.Y. Wu, D. Zhan, B. Ren, Quantitative correlation between defect density and heterogeneous electron transfer rate of single layer graphene, *J. Am. Chem. Soc.*, 136 (2014) 16609-16617.

[20] J. Melke, P. Jakes, J. Langner, L. Riekehr, U. Kunz, Z. Zhao Karger, A. Nefedov, H. Sezen, C. Wöll, H. Ehrenberg, C. Roth, Carbon materials for the positive electrode in all-vanadium redox flow batteries, *Carbon*, 78 (2014) 220-230.

[21] J. Jin, X. Fu, Q. Liu, Y. Liu, Z. Wei, K. Niu, J. Zhang, Identifying the active site in nitrogen-doped graphene for the VO^{2+}/VO_2^+ redox reaction, *ACS Nano*, 7 (2013) 4764-4773.

[22] Y. Zhao, R. Nakamura, K. Kamiya, S. Nakanishi, K. Hashimoto, Nitrogen-doped carbon nanomaterials as non-metal electrocatalysts for water oxidation, *Nat. Commun.*, 4 (2013) 2390.

The content of this chapter has been submitted for publication in Nanoscale as

Chapter 5 Synthesis of N-doped Carbon Nanotubes with Abundant Graphitic Nitrogen as an Electrocatalyst for Water Splitting in Alkaline Solution

Xubin Lu, Xin Yang, Haojie Zhang, Ralf B. Wehrspohn, Jia Li and Michael Bron

Abstract

Carbon-based materials, such as carbon nanotubes (CNTs), have been extensively developed and utilized in the renewable energy industry as energy storage and conversion materials. They are also potentially applicable to the water-splitting method, which requires electrocatalysts with high stability and low overpotential. Here, we report that N-doped CNTs (NCNTs), a highly abundant graphitic nitrogen and an extremely effective electrocatalyst, can be directly synthesized over Ni foam (NiF) at a low temperature (600°C) via atmospheric pressure chemical vapor deposition (APCVD). Scanning electron microscopy (SEM), transmission electron microscopy (TEM), X-ray photoelectron microscopy (XPS), X-ray diffraction (XRD), and Raman spectroscopy allowed insight into the characteristics of the hybrid electrode of NiF and NCNTs. The electrochemical activity of both the hydrogen evolution reaction (HER) and oxygen evolution reaction (OER) was performed by linear scanning voltammetry (LSV). The density functional theory (DFT) calculation paired with experimentation shows the contribution of both the metal substrate and heteroatom doping to facilitate the HER performance and produce renewable energy via electrolytic water splitting. Furthermore, these results provide a sufficient basis for the DFT calculation, which indicates that NCNTs with abundant g-N is a promising electrocatalyst for water splitting.

5.1 Introduction

The decomposition of water into separate hydrogen and oxygen components, also known as “water splitting”, has been regularly evaluated as a potential and promising clean and renewable energy solution to the global energy crisis^[1, 2]. The water splitting reaction consists of a HER and OER, two half-reactions that demonstrate sluggish kinetics. As state-of-the-art catalysts for water electrolysis, precious-metal-group

materials, like platinum and noble metal oxides, have played an important role in catalyzing the HER and OER kinetics (e.g., Pt for HER^[3, 4], RuO₂ for OER^[5]). However, large-scale application is impractical due to the high cost and limited availability of the catalyzing agents ^[6-9]. Consequently, tremendous effort has been invested into finding effective and economical alternatives. Notably, carbon-based materials like graphene^[10], Nitrogen-doped (N-Doped) graphene^[11], CNTs^[12], and NCNTs^[13] have been extensively investigated owing to their low cost, excellent mechanical properties, good electrical conductivity, and high activity towards the HER and OER.

Two primary strategies are employed to improve catalytic activity: 1) increasing the number of active sites by increasing catalyst loading; and 2) modifying their electronic structures to enlarge the active surface area or enhancing the intrinsic activity of the catalysts^[14]. Various research studies have attempted to implement the first strategy by combining transition-metals that exhibit remarkable catalytic activity with graphene or CNTs, such as MoS₂/graphene^[6], MoS_x/graphene ^[10], and N-doped TiO₂@CNTs ^[7, 11]. The addition of graphene and CNTs effectively increases the catalyst loading, which subsequently increases the electrocatalytic HER efficiency ^[6, 10, 15].

While it has been demonstrated that carbon-based materials effectively promote electrocatalysis, as the fundamental unit for most carbon allotropes, pristine graphene is not characterized by exceptional HER or OER activities ^[16, 17]. It has been broadly recognized that graphene, when combined with various nonmetal dopants, can significantly optimize the adsorption strength of certain key intermediates in the HER and OER. Thus, a number of studies have focused on modifying the electronic structure of graphene or CNTs by doping a heteroatom ^[13, 18] or adding functional groups ^[8], in order to improve catalytic performance. Xia et al.^[19] and Chen et al.^[20] characterized the nature of active sites in these carbon-based catalysts and reported that in N-doped graphene, the g-N is the actual active site for the oxygen reduction reaction. It has been demonstrated that the carbon atoms adjacent to the nitrogen dopant atoms are positively charged, owing to the electron-withdrawing effect of the nitrogen atom, thus facilitating the formation of an O-H bond and promoting overall catalytic activity^[21, 22].

Although there have been numerous investigations into enhancing the intrinsic activity of graphene or CNTs using chemical doping, very few studies have focused on

improving catalytic activity by coating graphene or CNTs on metal substrates. This method plays an important role both in graphene film synthesis and the subsequent application of graphene on electrodes [23, 24]. In this study, the HER catalytic performance of metal-supported and graphene doped methods were meticulously investigated using DFT calculations. Of the various models evaluated, nitrogen-doped graphene coating the Ni (111) surface exhibited superior HER catalytic performance, comparable to state-of-the-art platinum. The improvement of HER activity is attributed to elimination of planar distortion in the graphene sheets, which were caused by hydrogen adsorption. Motivated by these findings, we successfully synthesized Ni supported NCNTs, in which the concentration of nitrogen dopant was precisely customized, using vaporizing acetonitrile (ACN), to optimize catalytic performance. The HER activity of the synthesized sample was slightly lower than Pt, but higher than Ni, reaching a current density of -20 mA cm^{-2} at an overpotential of 128 mV and a Tafel slope of $121.04 \text{ mV dec}^{-1}$. Furthermore, the OER activity was also investigated. The results showed high activity with an overpotential of 250 mV, at 20 mA cm^{-2} , indicating these materials can also serve as the cathode in water splitting reactions. Subsequent DFT calculations revealed that the OER activity of NCNTs actually stems from nitrogen doping. These findings can aid in accelerating the rational design of carbon-based catalysts and offer a new opportunity for improving HER and OER activity.

5.2 Methods

5.2.1 Synthesis of graphene and ultrathin graphite

Pristine NiF was cut into $1 \text{ cm} \times 2 \text{ cm}$ strips and placed into an APCVD reactor, as shown in Fig. S1. Next, the cut foam was purged under a mixture of Ar and H_2 (Ar: $\text{H}_2 = 80:20 \text{ sccm}$) for ~ 30 minutes. Following this treatment, the growth chamber temperature was raised to 1080°C , where it remained for 30 min. The NiF was then exposed to H_2 and CH_4 (ratio $\text{H}_2:\text{CH}_4 = 20:60 \text{ sccm}$) for 20 min (graphene) or 50 min (UGr) to stimulate the growth of the graphene and UGr. Subsequently, the strips were cooled to room temperature under H_2 and Ar atmospheric conditions.

5.2.2 Synthesis of NCNTs and N-doped graphite

In order to grow NCNTs via APCVD, Fe nanoparticles (Fe NPs) were deposited using the Double-Pulse-Deposition (DPD) method, as shown in Figure S2. The NCNTs were grown in a commercial warm-wall CVD reactor, using a mixture of H₂, Ar, and ACN (Alfa Aesar, >99%) as the precursor gases. The gas delivery system and growth chamber were first purged with Ar and H₂ (Ar: H₂ = 25:10 sccm) for ~30 min. Next, the growth chamber temperature was raised to 600°C and maintained for 30 min. The gas flow rate was kept stable at 50 sccm and humidified using an ACN bubbler at room temperature. Following the 30 min growth window, the system was cooled down for 300 min with 25 sccm of Ar. N-doped graphite was obtained using the same gas ratio and temperature with the only difference being the absence of Fe NPs when the growth time was set of 10 min and substrate temperature was 750°C.

5.2.3 Electrochemical characterization

All electrochemical analyses were performed at room temperature (25 ± 3°C), using an Eco Chemie Autolab potentiostat/galvanostat PGstat 302 on 100 mL of electrolyte solution in a standard glass vessel equipped with a three-electrode system. Pt mesh and Hg|HgO electrodes were used as the counter electrode and reference electrode, respectively. NiF combined with carbon material was directly used as the working electrode. To determine the performance of the HER and OER, polarization curves were recorded by LSV after scanning five times from -1.8 V to 1.0 V at a scan rate of 10 mV s⁻¹ and plotted against Hg|HgO at a rate of 10 mV s⁻¹ in 1 M KOH. For the overall water splitting reaction, the prepared electrodes were directly used as the cathode and anode in a two-electrode system composed of 1 M KOH at room temperature. The polarization curves were recorded by LSV from 1.2 V to 2.0 V and plotted against the counter electrode voltage at a scan rate of 10 mV s⁻¹. Chronopotentiometric and chronoamperometric measurements were carried out under a constant overpotential of 0.28 V and 1.58 V, both of which were plotted against the reversible hydrogen electrode (RHE) and 1.58 (vs. RHE) without compensating for the IR drop.

5.2.4 IR correction

The electrolyte solution, wiring, NiF, and NiF with carbon material possess natural resistance. All these resistances collectively constitute the series resistance (R_s),

which can be indirectly obtained by fitting the EIS Nyquist plot to an equivalent circuit diagram or directly obtained from an EIS Nyquist plot as the first intercept of the main arc with the real axis. To obtain relatively appropriate electrochemical behavior of various catalysts, the main polarization curves were corrected for IR compensation as follows: $E_{\text{Corrected}} = E_{\text{Raw}} - IR_s$.

5.2.5 Calibration of the reference electrode

The Hg|HgO electrode was calibrated before the HER and OER measurements. The calibration was performed in a standard three-electrode system, where the Hg|HgO electrode was used as the reference electrode, and two Pt meshes were used as the working electrode and counter electrode. This relationship is expressed as: $E_{\text{RHE}} = E_{\text{Hg|HgO}} + 0.925 \text{ V} (0.099 + 0.059 \times \text{pH})$.

5.2.6 Electrochemically active surface area

The electrochemically active surface area (ECSA) of the samples was estimated by double-layer capacitance (C_{dl}) measurements using the cyclic voltammetry method without Faradic reaction. The currents were measured in a narrow window, using the method reported by Alshareef ^[25]. In this case, the currents can be primarily attributed to the charging of a double layer; and is expected to be linearly proportional to the active surface area. The double-layer capacitance is obtained by averaging the absolute value of anodic and cathodic slopes of linear fits as follows:

$$C_{\text{dl}} = \frac{|\text{Slope}(\text{anode})| + |\text{Slope}(\text{cathode})|}{2}$$

In this study, a NiF was used as the substrate and considered the standard. The ECSA of each catalyst is therefore calculated as follows:

$$A_{\text{ECSA}} = \frac{C_{\text{dl}} \text{ catalyst (mF cm}^{-2}\text{)}}{C_{\text{dl}} \text{ Ni foam (mF cm}^{-2}\text{) per cm}^2}$$

5.2.7 Physical Characterization

Raman spectra were measured using a Renishaw InVia spectrometer with 532 nm excitation wavelength and a Cobalt CW DPSS laser. In addition, a HORIBA, Jobin

Yvon iHR320, synapse CCD Raman spectrometer was also employed. This Raman spectrometer was equipped with an Olympus IX71 microscope for confocal sampling using an Nd:YAG, coherent, Verdi laser at 5 mW ($\lambda = 532$ nm). X-ray photoelectric spectra were recorded with a Kratos Axis Ultra X-ray photoelectron spectrometer using monochromatic Al $K\alpha$ radiation, an Omicron DAR 400 X-ray source with Al $K\alpha$ line (15 kV), and an Omicron EA 125X Hemispherical Energy Analyzer. The structural properties and morphology of CNTs were characterized via SEM using a PHILIPS ESEM XI 30 FEG instrument. XRD was carried out with a Bruker AXS D8 advanced X-ray diffractometer using Cu $K\alpha$ radiation ($\lambda = 1.5406$ Å) and a step size of 0.013° .

5.2.8 Computational details

All the first-principles calculations were performed using spin polarization within the DFT framework, as implemented in the VASP code [26, 27]. The projected augmented wave (PAW) pseudopotential [28] was used to describe the ionic cores. The plane wave basis, with a 400 eV kinetic energy cutoff, was employed after several convergence tests. The exchange-correlation energy is described via the Perdew-Burke-Ernzerhof (PBE) functional within the generalized gradient approximation [29]. Gaussian smearing of 0.05 eV is adapted to the partial orbital occupation during geometry optimization and a tetrahedron method with Blöchl corrections [30] is used to accurately calculate the electronic structures. For unsupported models, all atoms are free to move by conjugate gradient (CG) algorithm until the force on each atom is less than 0.02 eV Å⁻¹. For metal-supported models, atoms in the two bottom metal layers are fixed to their corresponding bulk positions, while atoms in the top layer of the metal and graphene sheets are able to relax until reaching the force convergence criteria. A gamma centred k-points sampling scheme of at least (12 x 12 x 1) per graphene unit cell was used for geometry optimization, and a denser k-points sample scheme (24 x 24 x 1) was used for the electronic structure calculations.

Considering the deficiency of DFT in describing van der Waals interactions, a suitable van der Waals functional optB88 [31] was selected to accurately simulate the interaction between hydrogen, graphene, and metals. A set of tests were conducted to reproduce the experimental results [23, 24] of the adsorption structures and the graphene sheet height above Ni (111) (Figure S3). The original PBE, optB88, and SCAN plus rvv10 [32,

^{33]} functionals gave reasonable results with respect to graphene sheet height - with the lowest binding energy around 2.1 Å; while the D3 ^[34] and TS ^[35] severely deviate from this value. Although PBE has reproduced the binding distances, the binding to Ni (111) is predicted to be endothermic, which is contrary to experimental evidence. In consideration of the high computational cost of SCAN, optB88 was selected as the van der Waals functional in our calculations.

5.3 Results and Discussion

5.3.1 NCNTs Characterization

Various hybrid electrodes of NiF and sp² carbon nanomaterials were synthesised as detailed in the experimental section and characterized with SEM/EDX, TEM, Raman spectroscopy, XRD and XPS. The SEM images shown in Figures 1a–c displayed that the morphologies and yield of NCNTs on Ni-F largely depends on the nucleation time (t_1). There was obviously no growth of NCNTs on the Ni-F using a short nucleation pulse to form nuclei on the substrate surface. Accordingly, a comparatively long initial polarisation (30 s) was necessary to a constant growth pulse and negative potential. NCNTs were homogeneously coated on the Ni-F as t_1 was set to 70 s, indicating an optimal nucleation time for growing NCNTs. However, after nucleating for more than 70 s, cluster-like NCNTs emerged on the Ni-F. The likely explanation for this clustering is that the Fe NPs escaped from the substrate into the gas stream and reabsorbed on the sites along the gas flow direction.^[36] Because Ni has a high carbon solubility (>0.1 at%),^[37] the carbon species can dissolve into the Ni and form a new thin layer of carbon consisting of the grown carbon interface, a carbon-Ni layer, and intrinsic Ni layer.^[38] The NCNTs grew on the manufactured carbon-Ni interface of the Ni-F and thus, cluster-like NCNTs could be detected.

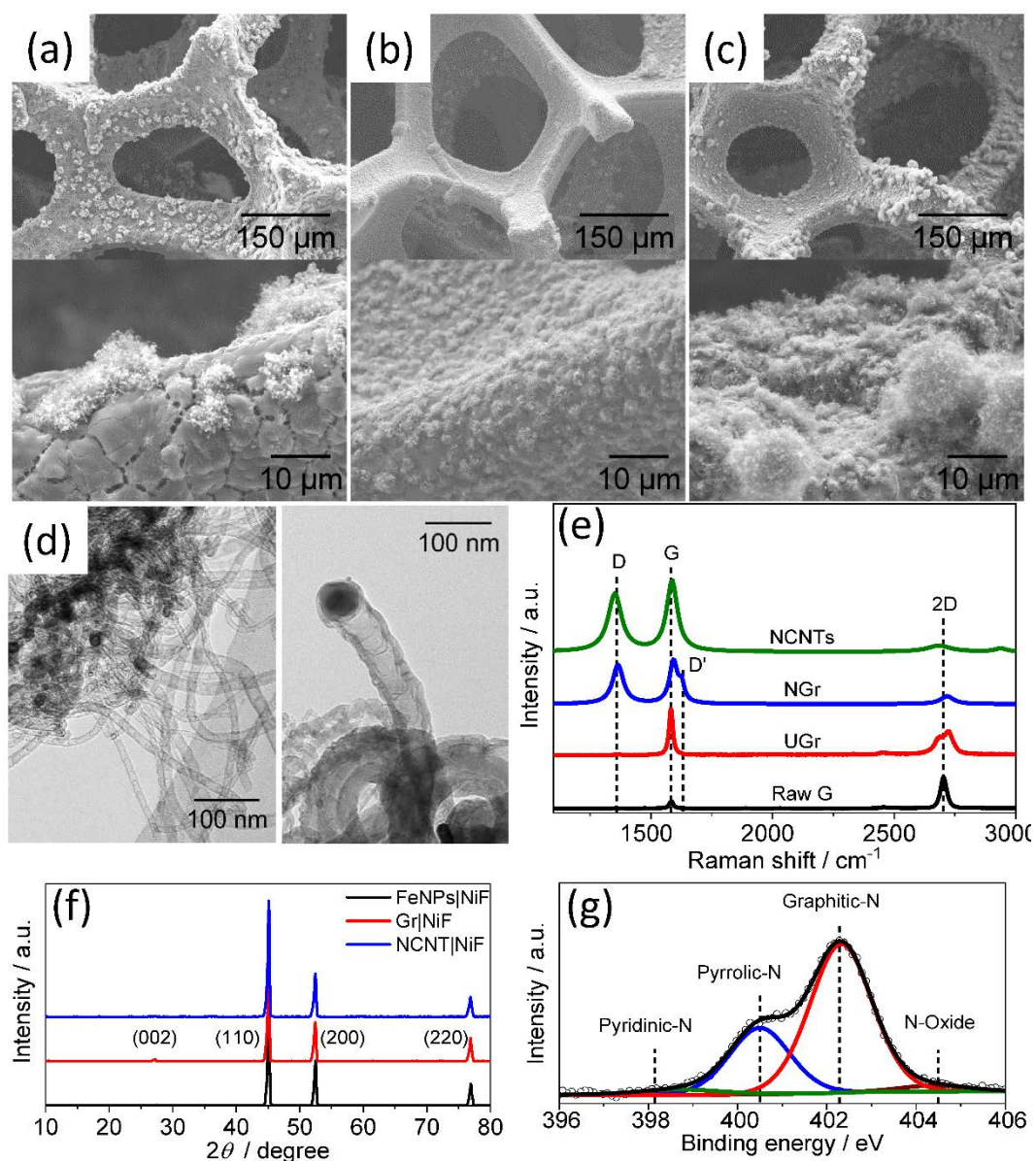


Figure 1. Structural characterization of the NCNTs@Ni-F. (a–c) ESEM images of as-grown NCNTs on the Ni-F substrates showing the effect of dispersion with increasing nucleation time: 30s, 70s and 90s. With high magnification micrographs. (d) The TEM image of NCNTs. (e) Representative Raman spectra of graphene, ultrathin graphite (UGr), N-doped graphite (NGr), and N-doped CNTs (NCNTs) on Ni foam. (f) XRD pattern of carbon materials on the NiF substrate. (g) N1s spectra of NCNTs at 600 $^{\circ}\text{C}$.

The TEM images showed that the microstructure of NCNTs, which were synthesized at 600 $^{\circ}\text{C}$ via APCVD, exhibited bamboo-like construction. This shape revealed the growth mechanism of NCNTs to be a nanotube catalyzed by a single iron particle.^[39] When the movement of the catalytic particle is slower than the growth rate of the

nanotube, a bamboo joint forms on the wall of the NCNTs. This growth mechanism is identical to that reported by Jung et al. and Tetana et al. concerning a mixture of N_2+H_2 in an ACN environment,^[40, 41] and will inevitably introduce some defects into the NCNTs, as shown in Figure 1d.

Comparison of Raman spectra with D, G, and 2D bands in pristine graphene, UGr@Ni-F, NGr@Ni-F, and NCNTs@Ni-F are shown in Figure 1f. UGr can be feasibly differentiated from pristine graphene by the intensive G model at $\sim 1580\text{ cm}^{-1}$ and the broad 2D model at $\sim 2720\text{ cm}^{-1}$.^[42] The 2D band of UGr is slightly blue-shifted due to the compressional strain from the large number of layers. Besides the distinct models of D, G and 2D, the D' model is detected in nitrogen-doped graphite (NGr). The introduction of heteroatoms results in the width and intensity of both the D and G peaks increasing, as well as a 2D peak blue shift when compared with graphene. In contrast, the weak 2D peak of NCNTs is slightly red-shifted when compared with the 2D peak of UGr and NGr and even raw graphene. The strong and broad D peak suggests that the NCNTs in this study are multiwall ^[43, 44].

The XRD pattern shown in Figure 1g exhibits only three stronger diffraction peaks of Ni-F with Fe NPs at ca. 45.0° , 52.5° , and 77.0° ^[45]. Stronger carbon peaks of Ni-F with Fe NPs at 27.2° were detected on both UGr@Ni-F and NCNTs@Ni-F.

Figure 1h and S8 show the representative XPS analysis of the UGr@Ni-F, NGr@Ni-F, and NCNTs@Ni-F. The total percentage of nitrogen for NCNTs is c.a. 4.97 at%. The broad N1s XPS peak of NCNTs can be fitted with four separate peaks, observed at 398.7 eV, 400.5 eV, 402.3 eV, and 404.4 eV. The peaks correlate with pyridinic-N (2.9%), pyrrolic-N (28.4%), g-N (65.5%), and oxidized pyridinic-N (3.2%), respectively ^[46, 47]. There are four distinct carbon groups in NGr and NCNTs: C=C of sp^2 (C1: 284.5 eV), C=N or C-O-C (C2: 285.8 eV), O-C=O or C-N (C3: 288.1 eV), and N-C=O (C4: 291.1 eV)^[11, 41]. The C1s XPS peak of both graphene and UGr can be fitted with the same four peaks specified above without the nitrogen groups. It worth noting that the ratio of C-C sp^2 and C-C sp^3 (C=N in NGr or NCNTs) remains a large value, which implies that pristine graphene contains perfect graphene networks.

5.3.2 Hydrogen evolution reaction performance

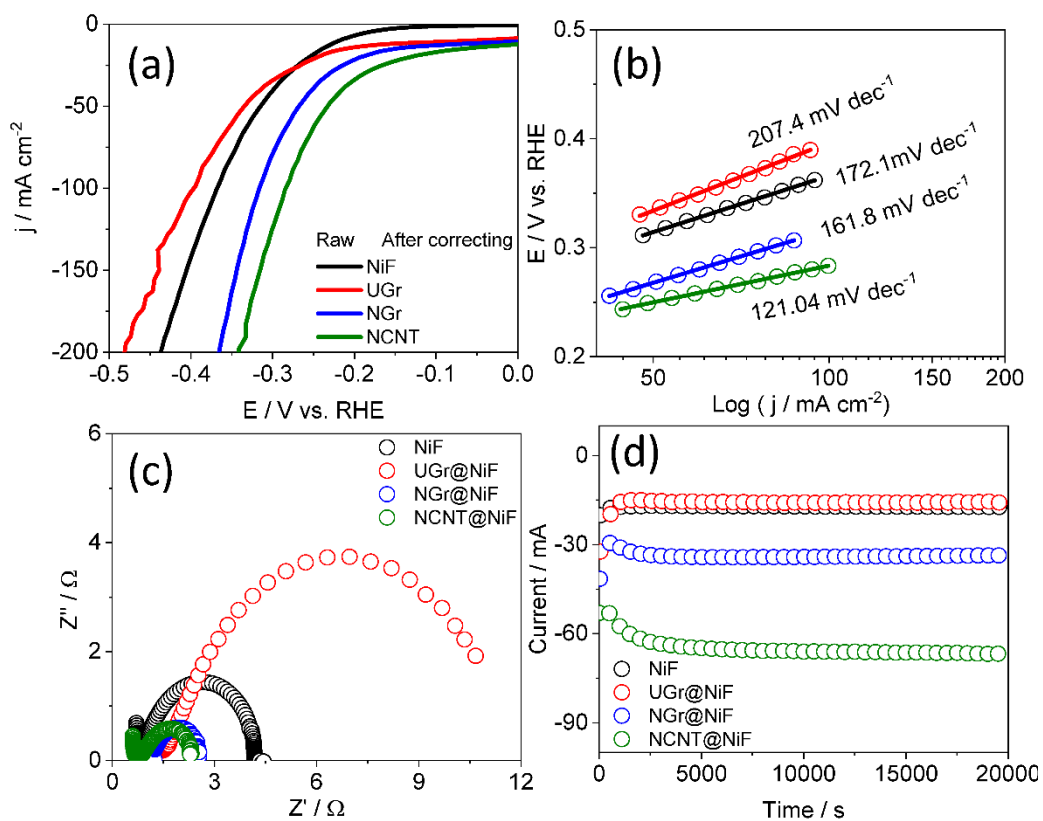


Figure 2. Electrocatalytic properties of NCNTs@Ni-F and other samples for hydrogen evolution reaction electrocatalysis in 1 M KOH. (a) LSV plots obtained with Ni-F, ultrathin graphite (UGr), N-doped graphite (NGr), and N-doped CNT (NCNT) at 10mVs^{-1} in 1M KOH. (b) Polarization curves-derived Tafel slopes for the corresponding electrocatalysts. (c) Electrochemical impedance spectroscopy data for hybrid materials in 1M KOH, (d) Long-term stability test carried out under a constant overpotential of 0.28 V vs. RHE.

To verify that the synthesized NCNTs@Ni electrode has superior HER electrocatalytic activity when compared to other carbon materials on Ni substrates, similar electrochemical performance evaluations were conducted on UGr@NiF, NGr@NiF and raw Ni-F. Polarization curves, corrected for electrolyte resistance, were recorded in LSV tests in 1 M KOH solution. The original HER data and Nyquist plots are shown in Figure S5. The comparison depicted in Figure 2a demonstrates that the NCNTs exhibit much higher activity than UGr and NGr. For NCNTs@Ni, a current density of 20 mA cm^{-2} can be achieved at an overpotential of 128 mV. In contrast, NGr@Ni, UGr@Ni, and raw Ni-F require overpotentials of 191 mV, 245 mV, and 254 mV, respectively, to drive the same current density. Furthermore, when overpotential is

plotted against current density, the NCNTs@Ni depicts the lowest Tafel slope ($121.04 \text{ mV dec}^{-1}$) among the four catalysts investigated, see Figure 2c.

The Tafel slope is closely related to electron and mass transport and follows the Volmer-Heyrovsky-Tafel mechanism. It is governed by the number and nature (whether or not electron transfer takes place) of the preceding steps and by the rate-determining step. A smaller Tafel slope indicates that the catalyst has a smaller $|\Delta G_{H^*}|$ and hence a smaller rate-determining step. For the NCNTs@Ni electrode, the electrochemical desorption pathway is the rate-determining step,^[6] and the Volmer-Heyrovsky-Tafel mechanism is reasonable for the HER. Furthermore, electrochemical impedance spectroscopy (EIS) in 1 M KOH solution was used to investigate the kinetics of the grown electrodes during the HER pathway. The charge-transfer resistance of the NCNTs@Ni-F electrode is slightly lower than that of NGr@Ni, but both catalysts are shown to have a faster charge-transfer capacity during the HER, when compared to UGr@Ni-F and Ni-F. However, because the NCNTs@Ni-F has a higher ECSA, the active performance of NCNTs@Ni-F is higher than that of NGr@Ni-F as shown in Figure S6. This also helps explain why NCNTs@Ni performs better than NGr@Ni-F.

5.3.3 Oxygen evolution reaction performance

The overpotential of the oxygen evolution reaction (OER) is an important measurement when evaluating the effectiveness of a particular catalyst, as the slow kinetics of the OER is the rate-determining step for the overall water splitting reaction. For this reason, the OER performance of NCNTs@Ni-F, in 1 M KOH, was also assessed. Figure 3a shows that the polarization curve of NCNTs@Ni-F achieved a low overpotential of 250 mV at a current density of 20 mA cm^{-2} . A lower Tafel slope of 52.4 mV dec^{-1} indicates that NCNTs@Ni electrode has a fast charge capacity during the OER. These results illustrated the high catalytic performance of NCNTs@Ni-F for the overall water splitting reaction, which is inconsistent with previous reports regarding the OER catalytic performance of N-doped graphene.

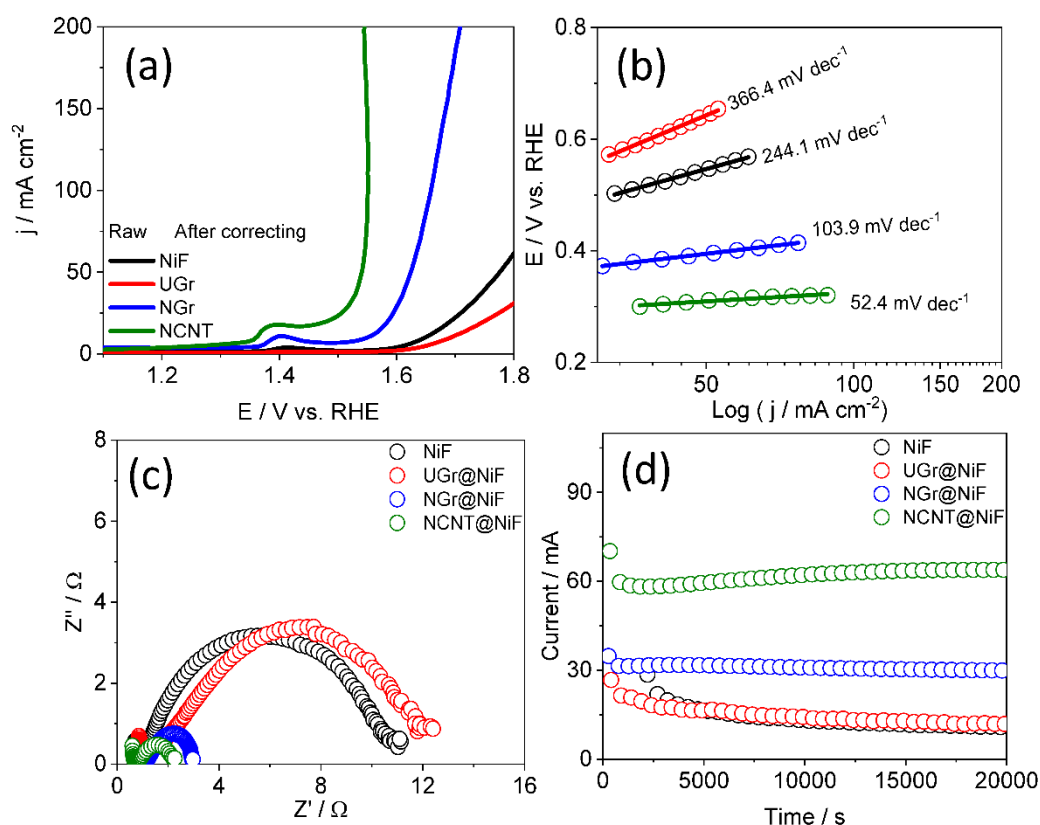


Figure 3. Electrocatalytic properties of NCNTs@Ni-F and other samples for Oxygen evolution reaction electrocatalysis in 1 M KOH. (a) LSV plots obtained with Ni-F, ultrathin graphite (UGr), N-doped graphite (NGr), and N-doped CNT (NCNT) at 10mVs^{-1} in 1M KOH. (b) Polarization curves-derived Tafel slopes for the corresponding electrocatalysts. (c) Electrochemical impedance spectroscopy data for hybrid materials in 1M KOH and (d) Long-term stability test carried out under a constant overpotential of 1.58 V vs. RHE.

As shown in Figure 7, the specific contribution of each participant in the system was investigated. The deposition of Fe NPs remarkably improved the electrocatalytic behavior of the OER before the NCNTs@Ni electrode was constructed; and synthesis of NCNTs on the deposited Fe NPs further facilitated this effect. The OER activity of the NCNTs@Ni electrode mainly originated from the electron-withdrawing effect of heteroatoms and the positive carbons adjacent to nitrogen.^[21, 22, 48] However, its actual active function to facilitate the OER is limited. This is inconsistent with the HER performance under the same processing parameters, indicating that the acute active sites facilitating the OER isn't the heteroatom concentration. However, being with an

available and highly-active group, such as g-N, could be a promising approach for enhancing the OER. Similarly, the stabilities of these catalysts were tested for 5h as shown in Figure 3d.

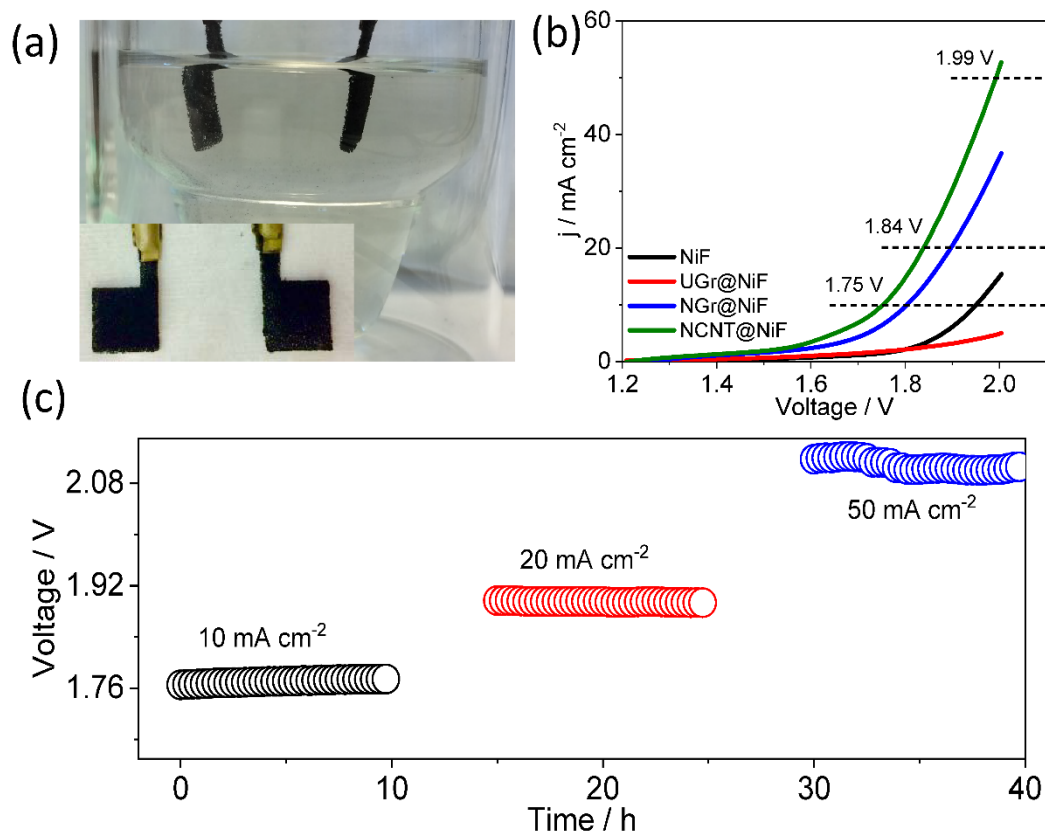


Figure 4. NCNTs@Ni-F electrocatalyst for overall water splitting in 1 M KOH. (a) Digital photograph of the two electrode configuration for both anode and cathode. (b) Polarization curve recorded at 10 mV s^{-1} . Inset: the NCNTs@Ni-F electrode for overall water splitting, (c) Long-term stability test carried out at constant current densities of 10, 20, and 50 mA cm^{-2} .

5.3.4 Over water splitting performance

NCNTs@Ni-F electrode was subsequently evaluated as both an anode and cathode in a single alkaline medium for the overall water-splitting reaction. Figure 4a depicts the polarization curve response obtained by plotting the current and potential at 10 mV s^{-1} . Under a two-electrode system, current densities of 10 mA cm^{-2} , 20 mA cm^{-2} , and 50 mA cm^{-2} were achieved and stable for 10 h at cell voltages of 1.76 V, 1.84 V, and 1.99 V, respectively (Figures 4b and 4c). These results are comparable with or

superior to previously reported results for only C-based electrocatalysts (Tables S2–S4).

5.3.5 Simulation of hydrogen evaluation reaction

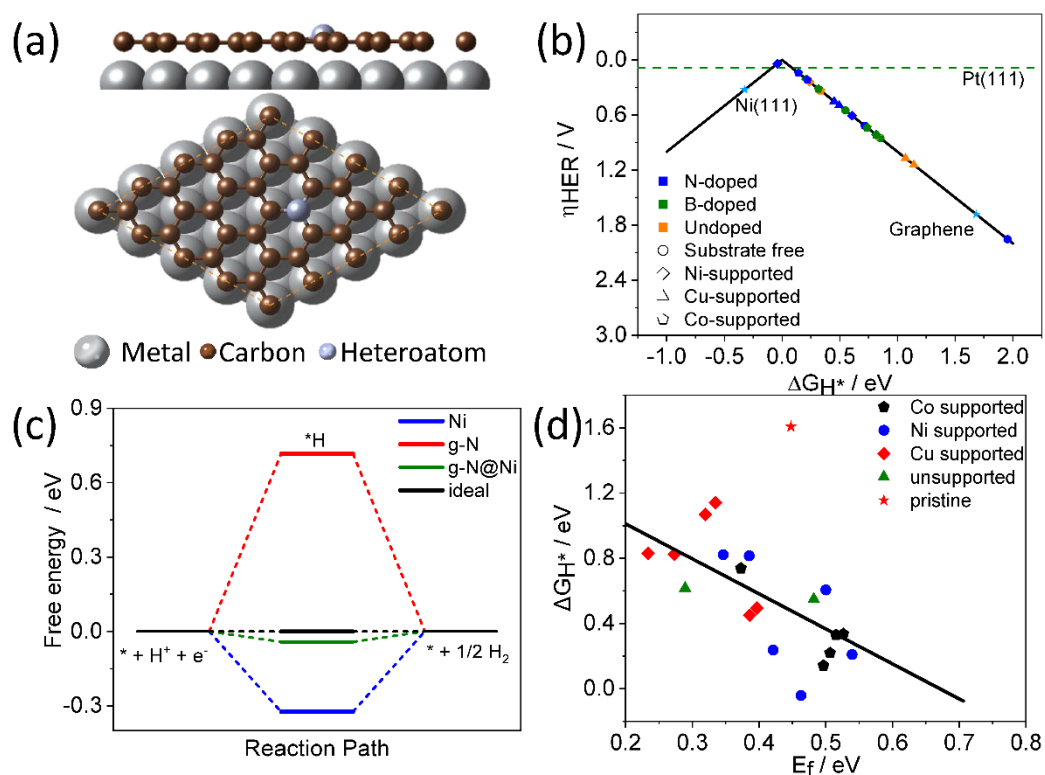


Figure 5. (a) Schematic illustration for the atomic structure of metal supported and heteroatom-doped graphene. (b) HER activities of the different metal supported and heteroatom-doped graphene sheets. (c) Free energy diagram for HER on Ni, N-doped graphene, Ni supported N-doped graphene and ideal catalyst. (d) The relationship between hydrogen adsorption Gibbs free energy ΔG_{H^*} and the formation energy of carbon vacancy.

The HER generally follows a three-step pathway: 1) the initial state of $H^+ + e^-$, 2) intermediate adsorption of H^* (* being the adsorption site) and, 3) production of $1/2 H_2$. Due to the mechanics of this reaction pathway, a catalyst's HER performance can be computationally evaluated by the adsorption Gibbs free energy of hydrogen (ΔG_{H^*}). An ideal HER catalyst should possess a moderate ΔG_{H^*} , close to 0 eV, in order to satisfy Sabatier's rule, i.e., simultaneously boost the adsorption and desorption process.^[9] This indicator has been extensively applied to predict catalyst HER activity

using first-principles calculations based on DFT.^[49] In this study, ΔG_{H^*} was employed to theoretically evaluate the HER performance of several carbon-based materials, including: pristine, Boron-doped graphene (BG); Nitrogen-doped graphene (NG); graphene coated metals; and pure metals, as shown in Figures 5 (a) and (b). Note that with the exception of the pure metals model, the plot exclusively shows HER activities of active carbon atoms. With respect to the B- and N-doped models, only graphitic heteroatom doping was considered, as all other doping methods result in a graphene layer collapsing onto the metal substrate. Negating the substantial planar distortion of the graphene sheet requires a large supercell and excessive computational cost, and thus, is beyond the scope of this study.

For unsupported graphene, only the carbon atoms surrounding the heteroatoms are considered as the active site. In contrast, metal-supported graphene has two active sites: 1) where heteroatoms occupy the top sites and, 2) face centre cubic (fcc) / hexagonal close packed (hcp) hollow sites of supported metals. According to the local atomic environment of active carbon atoms, these models are labelled as A-Gra@M-S, where A, M, and S denote the heteroatoms, supported metals, and hydrogen adsorption sites respectively. For detailed models and HER activities of other active sites (B and N atoms) refer to Figure S8. With pristine graphene used as the catalyst, the overall HER performance severely suffered from weak hydrogen binding and thus is limited by the adsorption step, which is inconsistent with previous literature.^[17, 50, 51] In the case where pure metals served as the catalyst, the desorption process was suppressed, owing to the powerful binding between hydrogen and metals.^[9] In contrast, both the doping and metal supporting models demonstrated considerably enhanced interaction between hydrogen and carbon atoms, which improved the overall HER performance of graphene. In particular, N-doped graphene supported by Ni (111) exhibited extraordinary HER activity with a moderate ΔG_{H^*} of -0.04 eV; and thus theoretically performed better than state-of-the-art Pt (111). Given these results, we further investigated the geometrical and electronic structure of these models to get a deeper understanding of the adsorption behaviour of hydrogen on carbon atoms and gain further insight into how doping and supporting metal improves the HER activities of graphene-based materials.

Currently, there are several descriptors relating to the intrinsic electronic structure of materials that can be used for evaluating the HER performance, including the work required to fill empty C states (W_{filling})^[52] and the energy level of the lowest unoccupied state referenced to vacuum level (ϵ_{LUS}).^[53] However, both descriptors are based on the rigid band approximation (RBA),^[52] which indicates that the adsorption of hydrogen injects a single electron into the substrate without altering the substrate's intrinsic band structure. Alternatively, our calculations showed that the adsorption of hydrogen significantly withdrew the active carbon atom from the graphene basal plane and directly opened a gap in the pristine graphene band structure (Figure S9). This phenomenon has also been confirmed by other theoretical calculations and experiments.^[50, 54-56] Using molecular orbital theory and first-principles calculation, S. Z. Qiao et al.^[17] proposed a descriptor E_p , namely the highest peak of the active centre DOS, which correlates linearly to the HER activity of carbon materials. Nevertheless, this descriptor also appears incompatible with our system, in that there is no clear trend between E_p and HER performance. The results for this and other descriptors are shown in Figure S10. Very recently, Wei jiang et al.^[49] put forward a suitable descriptor - the formation energy of oxygen vacancy E_f , for HER on oxygen-terminated MXenes. Their theoretical results demonstrated that the hydrogen adsorption on MXenes would extensively withdraw the active oxygen from the basal plane and substantially alter the intrinsic electronic structure of the substrate. This scenario parallels our system; the process is the same, but the materials are different. Further investigation into other descriptors ϵ_{LUS} and the number of electrons gained by the oxygen atom suggests that these descriptors are incapable of capturing the local structure distortion induced by hydrogen adsorption. Approximately 0.8–0.9 eV of distortion energy is required to pucker the planar graphene enough to form an sp^3 hybridized C–H bond.^[51] This distortion energy makes up a large proportion of the energy gain induced by hydrogen adsorption on pristine graphene. Thus, it is within reason to hypothesize that the HER performance of graphene-based materials will be substantially enhanced if the planar distortion can be mitigated. Following this principle, we calculated the carbon vacancy formation energy to explore the extent of distortion, then correlated this parameter to the Gibbs free energy of hydrogen adsorption. Figure 5d depicts a clear trend demonstrating that as E_f increases, ΔG_{H^+} decreases. Furthermore, the high E_f values indicate that formation of carbon vacancies is difficult, which indirectly implies the distortion does not occur easily. These results all support

the notion that metal substrates and heteroatom doping could alleviate the distortion of the graphene sheet.

The next issue to address was how to mitigate the distortion. Considering Ni supported models as an example, the catalyst performs much better if hydrogen is adsorbed on fcc hollow sites, where carbon binds less securely to the substrate; as opposed to on top of the Ni sites, where carbon binds more securely. This phenomenon is also manifested by the difference between the average height of carbon atoms at fcc hollow sites and Ni sites (see Table S4). The slightly higher carbon and lower carbon together established pseudo sp^3 networks, and hydrogen adsorption on the fcc hollow site of the carbon atoms was strengthened due to the reduction in distortion. Compared to Ni and Co substrates, Cu supported graphene exhibits inferior HER catalytic performance. This can be explained by the fact that the Cu-graphene bond is much weaker than the Ni- and Co- graphene bond, and by the height of graphene relative to these substrates. As for the consequence of doping, the incompatibility between the bond length C-N/C-B and C-C led to an upshift or downshift of the heteroatoms from the graphene basal plane. This phenomenon is not so apparent in unsupported graphene, but becomes evident in the metal-supported graphene sheet (Figure S11). Thus, the distortion caused by heteroatom doping pre-empted and partially negated the hydrogen adsorption deformation. Therefore, by intentionally introducing some planar distortion beforehand, via metal supporting and heteroatom doping, the distortion induced by hydrogen adsorption can be effectively mitigated, and thus the HER performance of these carbon-based materials is improved.

The NCNTs@Ni were constructed with abundant g-N in order to create more positive carbons adjacent to the dopants, and are in good agreement with DFT calculations. The DFT calculation models were established on the premise that the graphene and supporting frame shared the same dimensions. All models in previous studies neglected active sites that were distanced from the dopants.^[15] However, there is an intrinsic geometrical difference between the graphene and CNTs, especially with NCNTs that contain a high concentration of dopants away from substrate section. These will both enhance the catalytic activity and improve the ECSA of the NCNTs@Ni electrode.

5.3.6 Simulation of oxygen evaluation reaction

The origin of OER activity in NCNTs@Ni was investigated using DFT calculations. Three models were constructed and evaluated for their OER activity based on the previous established theoretical framework. The models consisted of: the edge of g-N doped graphene, the basal plane of g-N doped graphene, and N-doped graphene on Ni (111). For model details and adsorption structures, refer to Figure S8. Based on the free energy diagrams in Figure S12, the third step of the OER, namely the transition from *O to *OOH, is the rate-determining step for all three models. It is also apparent that carbon atoms surrounding the nitrogen at the bulk g-N exhibited the lowest OER activity, with an overpotential of 0.46 V, comparable to RuO₂, one of the best OER catalyst (0.42 eV).^[57] It should be noted that these findings are inconsistent with previous reports.^[15, 19, 20] Nevertheless, N-doped graphene on Ni (111) showed the least OER catalytic performance with an overpotential of 1.47 V. Therefore, the active site for the OER is not the metal supported N-doped graphene but the unsupported one, which is contrary to the active site in the HER. Although the metal substrate does not account for the OER activity of NCNTs, further experiments demonstrated that the Fe NPs on the NiF play a vital role in enhancing the OER performance, as reported in the previous study.^[58]

Summary

This study thoroughly samples the broader range of possible carbon materials, and exams their effectiveness as catalysts. The relative catalytic activity of NCNTs@Ni-F can be attributed to the following factors: 1) N-doping alters the electronic structure and further optimizes the reversible adsorption and desorption of hydrogen (Figures 5b and 5c). 2) A lower-temperature synthesis of NCNTs on the Ni-F ensures the presence of abundant g-N to facilitate the HER and OER, as shown in Figure 1 g. 3) High ECSAs enable close contact with the electrolyte, thus allowing more efficient utilization of the active site (Figure S6). 4) Increase in the Fe NPs concentration plays an important role in the OER (Figure S7). 5) The N-doped graphite fills the region free of NCNTs, not only enabling good mechanical adhesion and electrical attraction, but also improving the ECSA compared with NiF alone. 6) The positive carbon atoms adjacent to the incorporated nitrogen atoms facilitate the rate-determining step via the electrophilic OER owing to electron-withdrawing effect. 7) It is reasonable to conclude

that the geometric construction provides intrinsic catalytic effect, owing to the presence of considerable defects on the edge of bamboo-like NCNTs.

5.4 Conclusion

A combined theoretical and experimental study was carried out to synthesize and evaluate NCNTs as an ordinary and naturally abundant electrocatalyst for water splitting. The HER catalytic performance of metal supported and unsupported graphene sheets with heteroatom doping were evaluated by DFT calculations. Among all models, N-doped graphene coated on Ni (111) exhibited the best HER activity, which could be attributed to the negation of distortion induced by hydrogen adsorption. However, the main advantage is that the NCNTs@Ni electrode simultaneously improves both the HER and OER activities. This study customized the NCNTs doping by controlling the process parameters; the expected DFT results were not obtained. However, this study provides promising experimental evidence that a composite catalyst with a single dopant can be employed on a large scale to produce H₂ gas by splitting water and storing energy.

5.5 Reference

- [1] Y. Hou, X.D. Zhuang, X.L. Feng, Recent Advances in Earth-Abundant Heterogeneous Electrocatalysts for Photoelectrochemical Water Splitting, *Small Methods*, 1 (2017) 1700090
- [2] S.C. Huang, Y.Y. Meng, S.M. He, A. Goswami, Q.L. Wu, J.H. Li, S.F. Tong, T. Asefa, M.M. Wu, N-, O-, and S-Tridoped Carbon-Encapsulated Co₉S₈ Nanomaterials: Efficient Bifunctional Electrocatalysts for Overall Water Splitting, *Adv. Funct. Mater.*, 27 (2017) 1606585.
- [3] Y. Zheng, Y. Jiao, Y. Zhu, L.H. Li, Y. Han, Y. Chen, A. Du, M. Jaroniec, S.Z. Qiao, Hydrogen evolution by a metal-free electrocatalyst, *Nat. Commun.*, 5 (2014) 3783.
- [4] E. Fabbri, A. Habereder, K. Waltar, R. Kotz, T.J. Schmidt, Developments and perspectives of oxide-based catalysts for the oxygen evolution reaction, *Catal. Sci. Technol.*, 4 (2014) 3800-3821.
- [5] R.R. Rao, M.J. Kolb, N.B. Halck, A.F. Pedersen, A. Mehta, H. You, K.A. Stoerzinger, Z. Feng, H.A. Hansen, H. Zhou, L. Giordano, J. Rossmeisl, T. Vegge, I. Chorkendorff,

- I.E.L. Stephens, Y. Shao-Horn, Towards identifying the active sites on RuO₂(110) in catalyzing oxygen evolution, *Energy Environ. Sci.*, 10 (2017) 2626-2637.
- [6] Y. Li, H. Wang, L. Xie, Y. Liang, G. Hong, H. Dai, MoS₂ nanoparticles grown on graphene: an advanced catalyst for the hydrogen evolution reaction, *J. Am. Chem. Soc.*, 133 (2011) 7296-7299.
- [7] J. Du, F. Cheng, S. Wang, T. Zhang, J. Chen, M(salen)-derived nitrogen-doped M/C (M = Fe, Co, Ni) porous nanocomposites for electrocatalytic oxygen reduction, *Sci. Rep.*, 4 (2014) 4386.
- [8] X. Lu, W.L. Yim, B.H. Suryanto, C. Zhao, Electrocatalytic oxygen evolution at surface-oxidized multiwall carbon nanotubes, *J. Am. Chem. Soc.*, 137 (2015) 2901-2907.
- [9] J.K. Nørskov, T. Bligaard, A. Logadottir, J.R. Kitchin, J.G. Chen, S. Pandelov, U. Stimming, Trends in the Exchange Current for Hydrogen Evolution, *J. Electrochem. Soc.*, 152 (2005) J23-J26.
- [10] Y.H. Chang, C.T. Lin, T.Y. Chen, C.L. Hsu, Y.H. Lee, W. Zhang, K.H. Wei, L.J. Li, Highly efficient electrocatalytic hydrogen production by MoS(x) grown on graphene-protected 3D Ni foams, *Adv. Mater.*, 25 (2013) 756-760.
- [11] Y.M. Li, Z.G. Wang, X.J. Lv, N-doped TiO₂ nanotubes/N-doped graphene nanosheets composites as high performance anode materials in lithium-ion battery, *J. Mater. Chem. A*, 2 (2014) 15473-15479.
- [12] Y.K. Kim, H. Park, Light-harvesting multi-walled carbon nanotubes and CdS hybrids: Application to photocatalytic hydrogen production from water, *Energy Environ. Sci.*, 4 (2011) 685-694.
- [13] Z.B. Tian, C. Liu, Q.Y. Li, J.Y. Hou, Y. Li, S.Y. Ai, Nitrogen- and oxygen-functionalized carbon nanotubes supported Pt-based catalyst for the selective hydrogenation of cinnamaldehyde, *Appl. Catal., A*, 506 (2015) 134-142.
- [14] Z.W. Seh, J. Kibsgaard, C.F. Dickens, I. Chorkendorff, J.K. Nørskov, T.F. Jaramillo, Combining theory and experiment in electrocatalysis: Insights into materials design, *Science*, 355 (2017).
- [15] Y. Jiao, Y. Zheng, K. Davey, S.Z. Qiao, Activity origin and catalyst design principles for electrocatalytic hydrogen evolution on heteroatom-doped graphene, *Nat. Energy.*, 1 (2016) 1-9.

- [16] Y. Zheng, Y. Jiao, L.H. Li, T. Xing, Y. Chen, M. Jaroniec, S.Z. Qiao, Toward design of synergistically active carbon-based catalysts for electrocatalytic hydrogen evolution, *ACS Nano*, 8 (2014) 5290-5296.
- [17] Y. Jiao, Y. Zheng, K. Davey, S.-Z. Qiao, Activity origin and catalyst design principles for electrocatalytic hydrogen evolution on heteroatom-doped graphene, *Nature Energy*, 1 (2016).
- [18] G. Zhu, Z. He, J. Chen, J. Zhao, X. Feng, Y. Ma, Q. Fan, L. Wang, W. Huang, Highly conductive three-dimensional MnO₂-carbon nanotube-graphene-Ni hybrid foam as a binder-free supercapacitor electrode, *Nanoscale*, 6 (2014) 1079-1085.
- [19] M.T. Li, L.P. Zhang, Q. Xu, J.B. Niu, Z.H. Xia, N-doped graphene as catalysts for oxygen reduction and oxygen evolution reactions: Theoretical considerations, *J. Catal.*, 314 (2014) 66-72.
- [20] X.K. Kong, Q.C. Liu, D.B. Chen, G.L. Chen, Identifying the Active Sites on N-doped Graphene toward Oxygen Evolution Reaction, *Chemcatchem*, 9 (2017) 846-852.
- [21] Y. Zhao, R. Nakamura, K. Kamiya, S. Nakanishi, K. Hashimoto, Nitrogen-doped carbon nanomaterials as non-metal electrocatalysts for water oxidation, *Nat. Commun.*, 4 (2013) 2390.
- [22] B.S. Yeo, A.T. Bell, Enhanced activity of gold-supported cobalt oxide for the electrochemical evolution of oxygen, *J. Am. Chem. Soc.*, 133 (2011) 5587-5593.
- [23] Y.S. Dedkov, M. Fonin, Electronic and magnetic properties of the graphene-ferromagnet interface, *New Journal of Physics*, 12 (2010).
- [24] Y. Gamo, A. Nagashima, M. Wakabayashi, M. Terai, C. Oshima, Atomic structure of monolayer graphite formed on Ni(111), *Surf. Sci.*, 374 (1997) 61-64.
- [25] H. Liang, A.N. Gandi, D.H. Anjum, X. Wang, U. Schwingenschlogl, H.N. Alshareef, Plasma-Assisted Synthesis of NiCoP for Efficient Overall Water Splitting, *Nano Lett.*, 16 (2016) 7718-7725.
- [26] G. Kresse, J. Furthmuller, Efficiency of ab-initio total energy calculations for metals and semiconductors using a plane-wave basis set, *Comp. Mater. Sci.*, 6 (1996) 15-50.
- [27] G. Kresse, J. Furthmuller, Efficient iterative schemes for ab initio total-energy calculations using a plane-wave basis set, *Phys. Rev. B*, 54 (1996) 11169-11186.
- [28] P.E. Blöchl, Projector augmented-wave method, *Phys. Rev. B*, 50 (1994) 17953-17979.

- [29] J.P. Perdew, K. Burke, M. Ernzerhof, Generalized gradient approximation made simple, *Phys. Rev. Lett.*, 77 (1996) 3865-3868.
- [30] P.E. Blöchl, O. Jepsen, O.K. Andersen, Improved tetrahedron method for Brillouin-zone integrations, *Physical Review B*, 49 (1994) 16223-16233.
- [31] J. Klimes, D.R. Bowler, A. Michaelides, Chemical accuracy for the van der Waals density functional, *J Phys Condens Matter*, 22 (2010) 022201.
- [32] J. Sun, A. Ruzsinszky, J.P. Perdew, Strongly Constrained and Appropriately Normed Semilocal Density Functional, *Phys Rev Lett*, 115 (2015) 036402.
- [33] H. Peng, Z.-H. Yang, J.P. Perdew, J. Sun, Versatile van der Waals Density Functional Based on a Meta-Generalized Gradient Approximation, *Phys. Rev. X*, 6 (2016).
- [34] S. Grimme, J. Antony, S. Ehrlich, H. Krieg, A consistent and accurate ab initio parametrization of density functional dispersion correction (DFT-D) for the 94 elements H-Pu, *J. Chem. Phys.*, 132 (2010) 154104.
- [35] A. Tkatchenko, M. Scheffler, Accurate molecular van der Waals interactions from ground-state electron density and free-atom reference data, *Phys Rev Lett*, 102 (2009) 073005.
- [36] X. Zhang, Y. Huang, X. Chen, Q. Gao, W. Zhang, Nitrogen-doped carbon nanotubes based on melamine-formaldehyde resin as highly efficient catalyst for oxygen reduction reaction, *J. Colloid Interface Sci.*, 509 (2018) 1-9.
- [37] L. Huang, Q.H. Chang, G.L. Guo, Y. Liu, Y.Q. Xie, T. Wang, B. Ling, H.F. Yang, Synthesis of high-quality graphene films on nickel foils by rapid thermal chemical vapor deposition, *Carbon*, 50 (2012) 551-556.
- [38] J.K. Chinthaginjala, D.B. Thakur, K. Seshan, L. Lefferts, How Carbon-Nano-Fibers attach to Ni foam, *Carbon*, 46 (2008) 1638-1647.
- [39] Y. Lu, Z.P. Zhu, D.S. Su, D. Wang, Z.Y. Liu, R. Schlogl, Formation of bamboo-shape carbon nanotubes by controlled rapid decomposition of picric acid, *Carbon*, 42 (2004) 3199-3207.
- [40] M. Junga, K.Y. Eunb, J.K. Leeb, K.R. Leeb, Y.J. Baikb, J.W. Parka, Growth of carbon nanotubes by chemical vapor deposition, *Diamond Relat. Mater.*, 10 (2001) 1235-1240.
- [41] Z.N. Tetanaa, S.D. Mhlangaa, G. Bepetea, R.W.M. Krauseb, N.J. Coville, The Synthesis of Nitrogen-Doped Multiwalled Carbon Nanotubes Using an Fe-Co/CaCO₃, *S. Afr. J. Chem.*, 65 (2012) 39-49.

- [42] L.M. Malard, M.A. Pimenta, G. Dresselhaus, M.S. Dresselhaus, Raman spectroscopy in graphene, *Phys. Rep.*, 473 (2009) 51-87.
- [43] T. Sharifi, F. Nitze, H.R. Barzegar, C.W. Tai, M. Mazurkiewicz, A. Malolepszy, L. Stobinski, T. Wagberg, Nitrogen doped multi walled carbon nanotubes produced by CVD-correlating XPS and Raman spectroscopy for the study of nitrogen inclusion, *Carbon*, 50 (2012) 3535-3541.
- [44] O.Y. Podyacheva, A.N. Suboch, S.N. Bokova-Sirosh, A.I. Romanenko, L.S. Kibis, E.D. Obratsova, V.L. Kuznetsov, Analysis of Defect-Free Graphene Blocks in Nitrogen-Doped Bamboo-Like Carbon Nanotubes, *Phys. Status Solidi B*, 255 (2018) 1700253.
- [45] X. Lu, C. Zhao, Electrodeposition of hierarchically structured three-dimensional nickel-iron electrodes for efficient oxygen evolution at high current densities, *Nat. Commun.*, 6 (2015) 6616.
- [46] J. Zhang, Z. Zhao, Z. Xia, L. Dai, A metal-free bifunctional electrocatalyst for oxygen reduction and oxygen evolution reactions, *Nat. Nanotechnol.*, 10 (2015) 444-452.
- [47] I.Z. Gonzalez, A.M. Valenzuela-Muniz, G. Alonso-Nunez, M.H. Farias, Y.V. Gomez, Influence of the Synthesis Parameters in Carbon Nanotubes Doped with Nitrogen for Oxygen Electroreduction, *ECS J. Solid State Sci. Technol.*, 6 (2017) M3135-M3139.
- [48] H. Kim, K. Lee, S.I. Woo, Y. Jung, On the mechanism of enhanced oxygen reduction reaction in nitrogen-doped graphene nanoribbons, *Phys. Chem. Chem. Phys.*, 13 (2011) 17505-17510.
- [49] W. Jiang, X. Zou, H. Du, L. Gan, C. Xu, F. Kang, W. Duan, J. Li, Universal Descriptor for Large-Scale Screening of High-Performance MXene-Based Materials for Energy Storage and Conversion, *Chemistry of Materials*, 30 (2018) 2687-2693.
- [50] E.J. Duplock, M. Scheffler, P.J. Lindan, Hallmark of perfect graphene, *Phys Rev Lett*, 92 (2004) 225502.
- [51] S. Casolo, O.M. Lovvik, R. Martinazzo, G.F. Tantardini, Understanding adsorption of hydrogen atoms on graphene, *J Chem Phys*, 130 (2009) 054704.
- [52] Y. Liu, Y.M. Wang, B.I. Yakobson, B.C. Wood, Assessing carbon-based anodes for lithium-ion batteries: a universal description of charge-transfer binding, *Phys Rev Lett*, 113 (2014) 028304.

- [53] Y. Liu, J. Wu, K.P. Hackenberg, J. Zhang, Y.M. Wang, Y. Yang, K. Keyshar, J. Gu, T. Ogitsu, R. Vajtai, J. Lou, P.M. Ajayan, Brandon C. Wood, B.I. Yakobson, Self-optimizing, highly surface-active layered metal dichalcogenide catalysts for hydrogen evolution, *Nat. Energy.*, 2 (2017).
- [54] J. Zhou, M.M. Wu, X. Zhou, Q. Sun, Tuning electronic and magnetic properties of graphene by surface modification, *Applied Physics Letters*, 95 (2009).
- [55] J.O. Sofo, A.S. Chaudhari, G.D. Barber, Graphane: A two-dimensional hydrocarbon, *Physical Review B*, 75 (2007).
- [56] R. Balog, B. Jorgensen, L. Nilsson, M. Andersen, E. Rienks, M. Bianchi, M. Fanetti, E. Laegsgaard, A. Baraldi, S. Lizzit, Z. Slijivancanin, F. Besenbacher, B. Hammer, T.G. Pedersen, P. Hofmann, L. Hornekaer, Bandgap opening in graphene induced by patterned hydrogen adsorption, *Nat Mater*, 9 (2010) 315-319.
- [57] I.C. Man, H.Y. Su, F. Calle-Vallejo, H.A. Hansen, J.I. Martinez, N.G. Inoglu, J. Kitchin, T.F. Jaramillo, J.K. Norskov, J. Rossmeisl, Universality in Oxygen Evolution Electrocatalysis on Oxide Surfaces, *Chemcatchem*, 3 (2011) 1159-1165.
- [58] G. Chieffi, C. Giordano, M. Antonietti, D. Esposito, FeNi nanoparticles with carbon armor as sustainable hydrogenation catalysts: towards biorefineries, *J. Mater. Chem. A*, 2 (2014) 11591-11596.

5.6 Supporting information

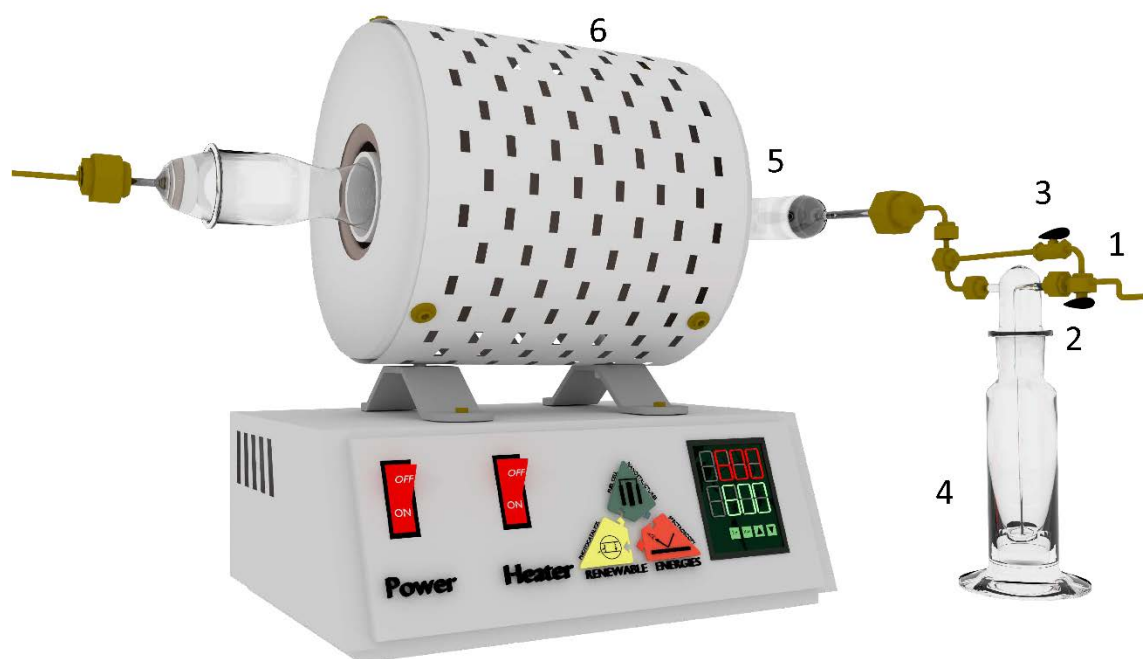


Figure S1. Simple schematic drawing of atmospheric pressure chemical vapor deposition (APCVD) system. 1) gas mixing Ar + H₂ or Ar + H₂ + CH₄; 2) Changeover valve 3) Changeover valve; 4) Liquid precursor (ACN); 5) Quartz tube; 6) APCVD.

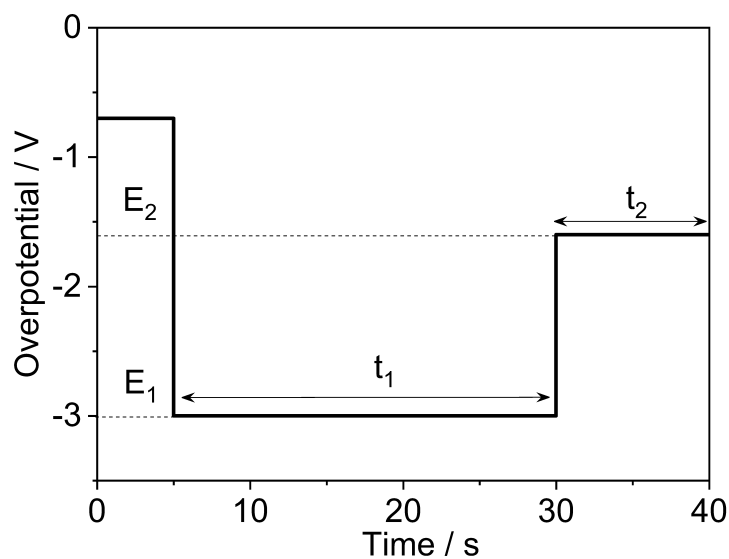


Figure. S2. Schematic representation of the double pulse potential technique, nucleation potential: $E_1 = -3$ V; growth potential: $E_2 = -1.6$ V; nucleation time: t_1 , and growth time: t_2 .

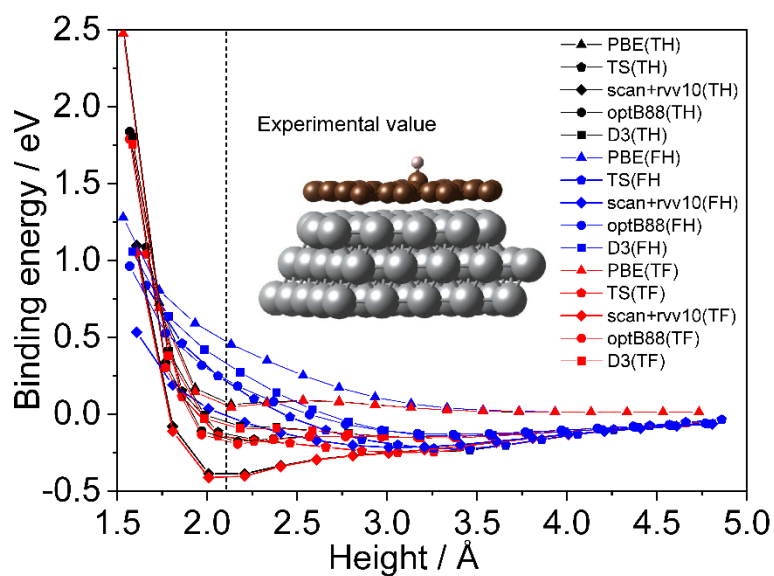


Figure S3. The binding energy as a function of PBE, optB88, SCAN+rvv10 reproduced the experimental value of the height of graphene (about 2.1 Å), where the blue, green, and orange indicates Cobalt, Nickel, and the Copper substrate.

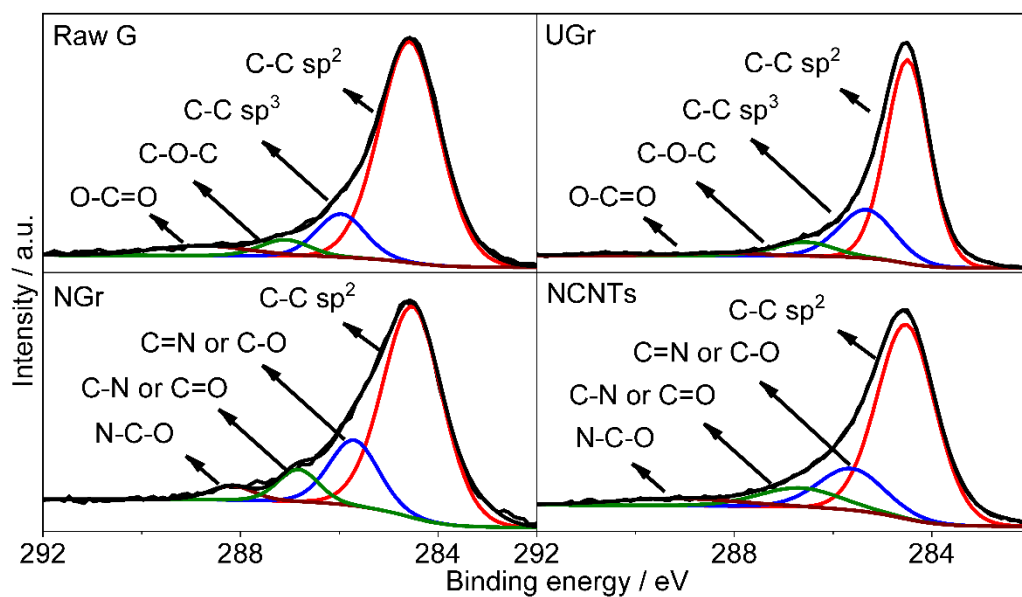


Figure S4. XPS spectra of graphene, ultrathin graphite, N-doped graphene, and N-doped CNTs on Ni foam. The growth time of graphene and ultrathin graphite are respectively 20 min and 50 min, the growth temperature 1080°C. Synthesis of N-doped graphene and N-doped CNTs are respectively 750°C and 600°C in APCVD; the growth time are respectively 10 min and 30 min.

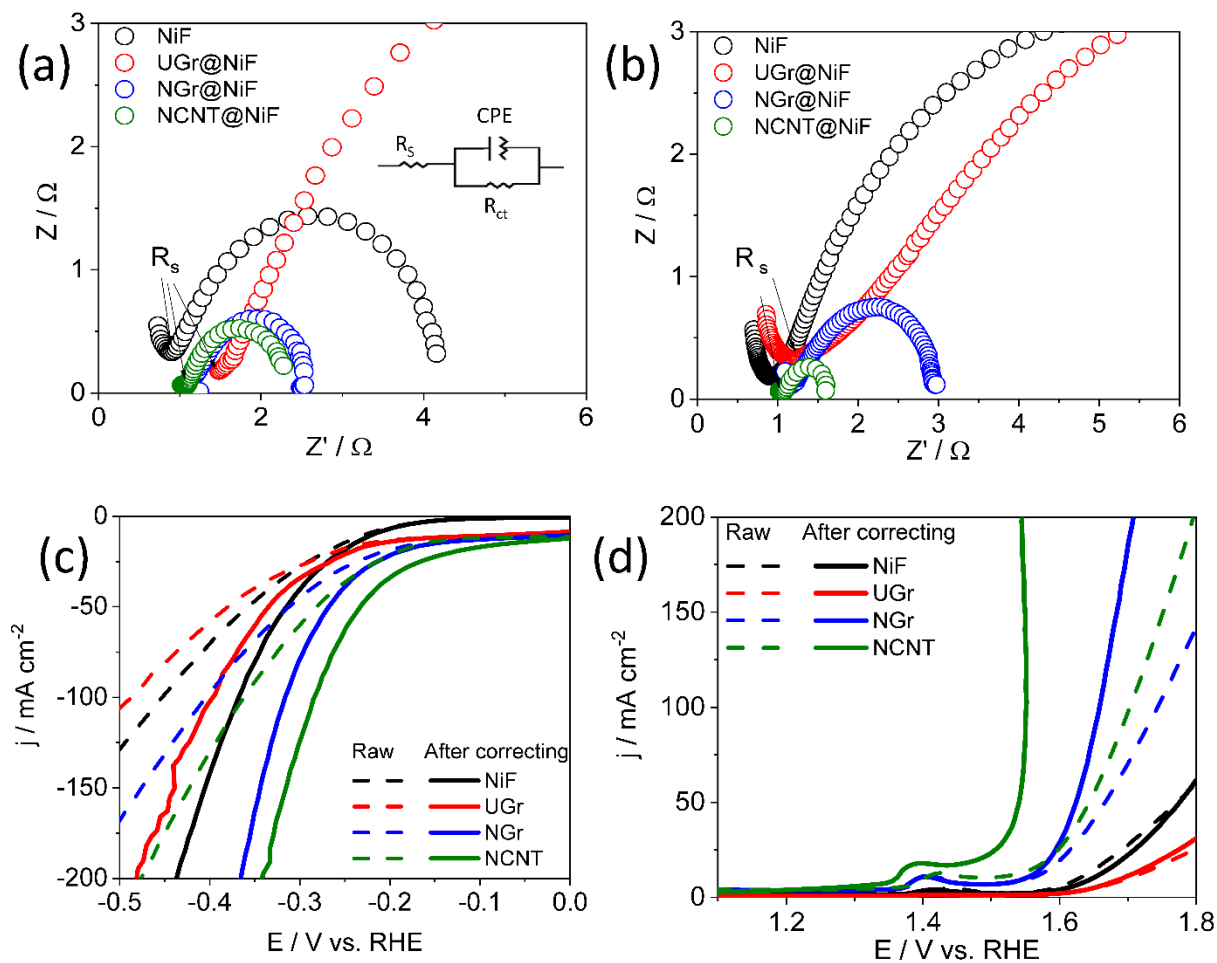


Figure S5. (a) and (b) Nyquist plots of NiF, UGr, NGr, and NCNTs for HER, shown in the inset, the equivalent circuit diagram used for analysis of the EIS curves measured for the HER and OER. (c) and (d) Before and after correcting LSV plots obtained with NiF, ultrathin graphite (UGr), N-doped graphite (NGr), and N-doped CNT (NCNT) at 10mVs^{-1} in 1M KOH for the HER and OER.

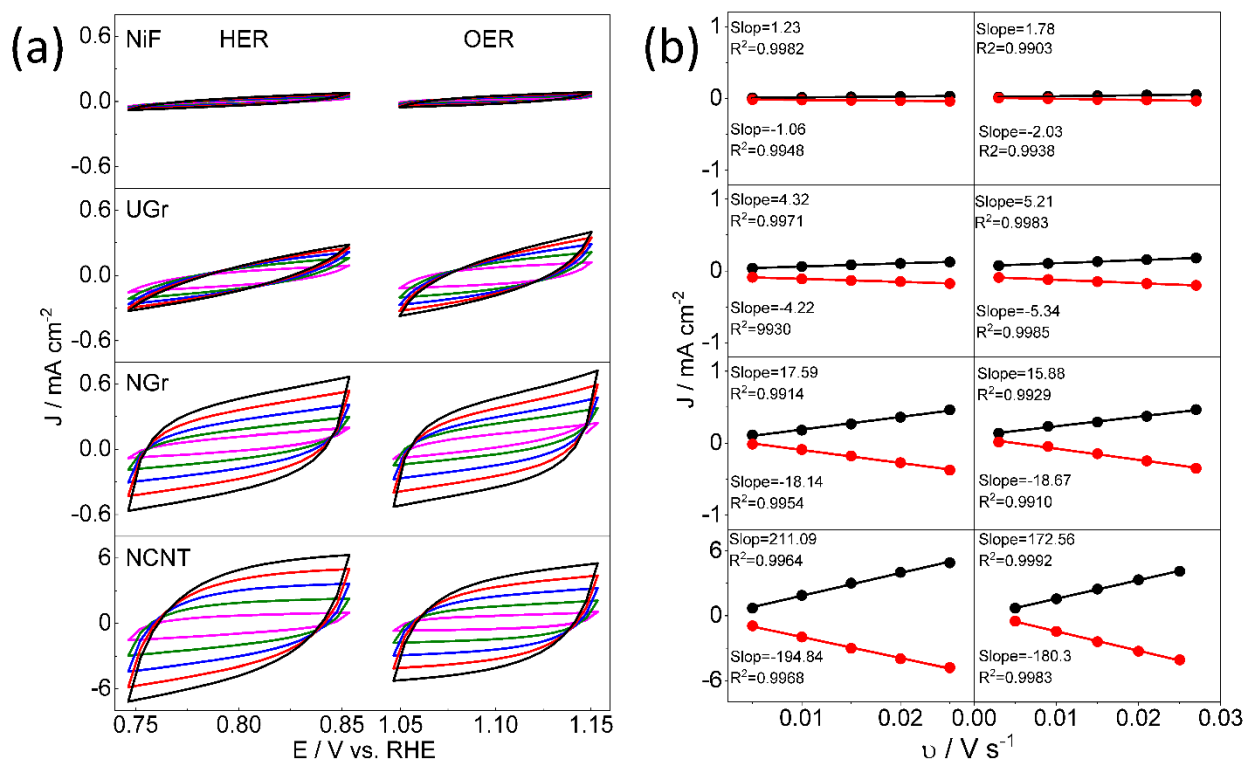


Figure S6. Electrochemical capacitance measurements for the estimation of the relative electrochemical active surface area of Ni foam, ultrathin graphite, N-doped graphite, and N-doped CNT upon HER and OER. (a) Cyclic voltammograms in the region of 0.75 – 0.85 V vs. RHE and 1.05 – 1.15 V vs. RHE (b) The differences in current density at 0.80 V and 1.1 V vs. RHE plotted as a function of scan rate fitted to a linear regression, where the slope is C_{dl} .

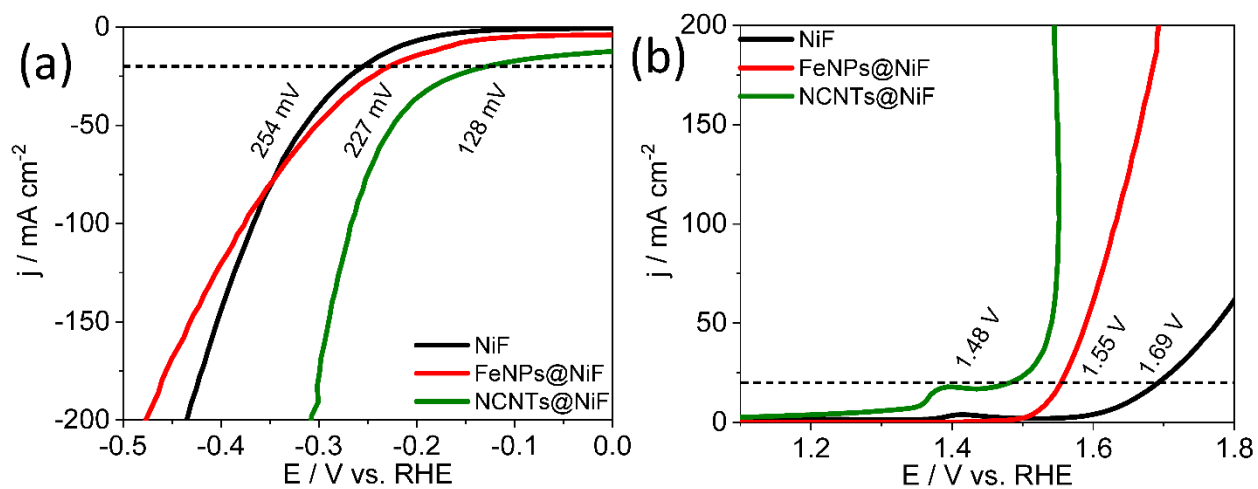


Figure S7. The effect of FeNPs on the electrocatalytic activities of NCNTs@Ni-F electrode. Nucleation time (t_1) is 70 s; the growth time is 10 s (t_2). The NCNTs were prepared with the parameter of Table S2.

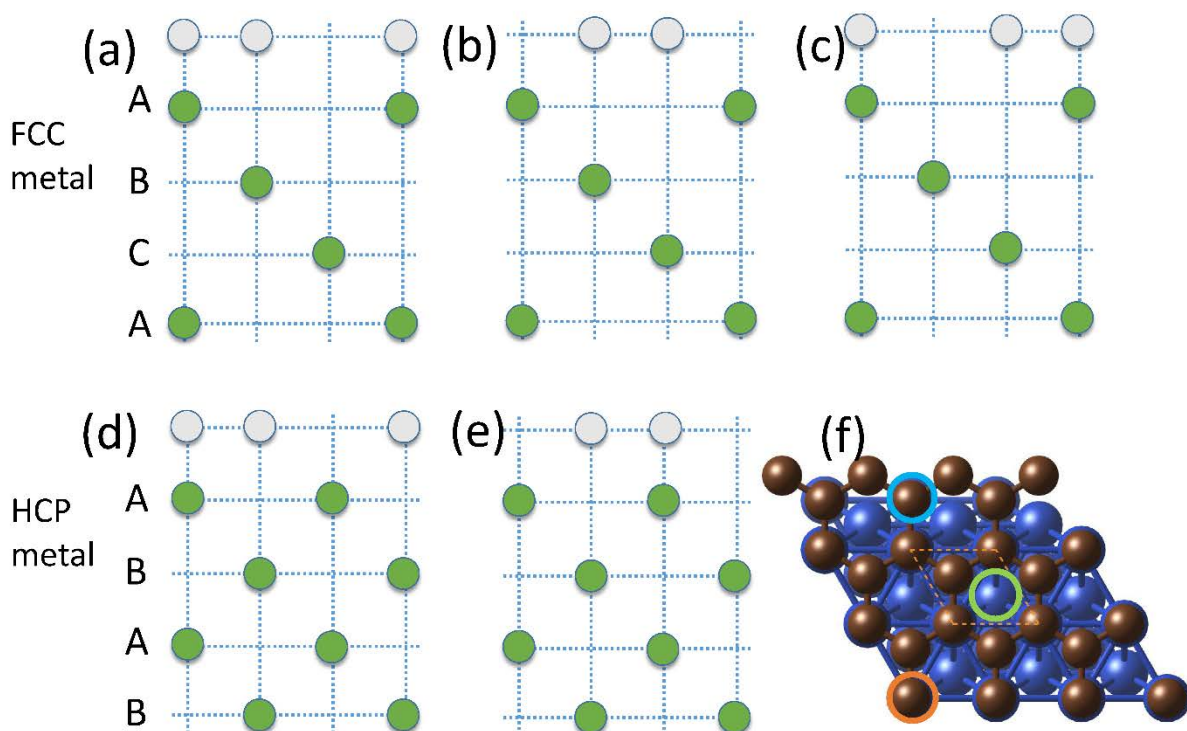


Figure S8. Three possible Schematic illustrations with C_{3v} symmetry for graphene on (a) the top and hcp hollow (TH), (b) fcc hollow and hcp hollow (FH), and (c) top and fcc hollow (TF) sites of Cu or Ni. (d) TH and (e) FH of Co, where the green circles indicate Cu/Co/Ni, grey circles indicate B/C/N. (f) the geometric structure of adsorption sites for FCC and HCP, where the blue circle indicates FCC hollow site, an orange circle indicates top site and green circle indicates HCP hollow sites.

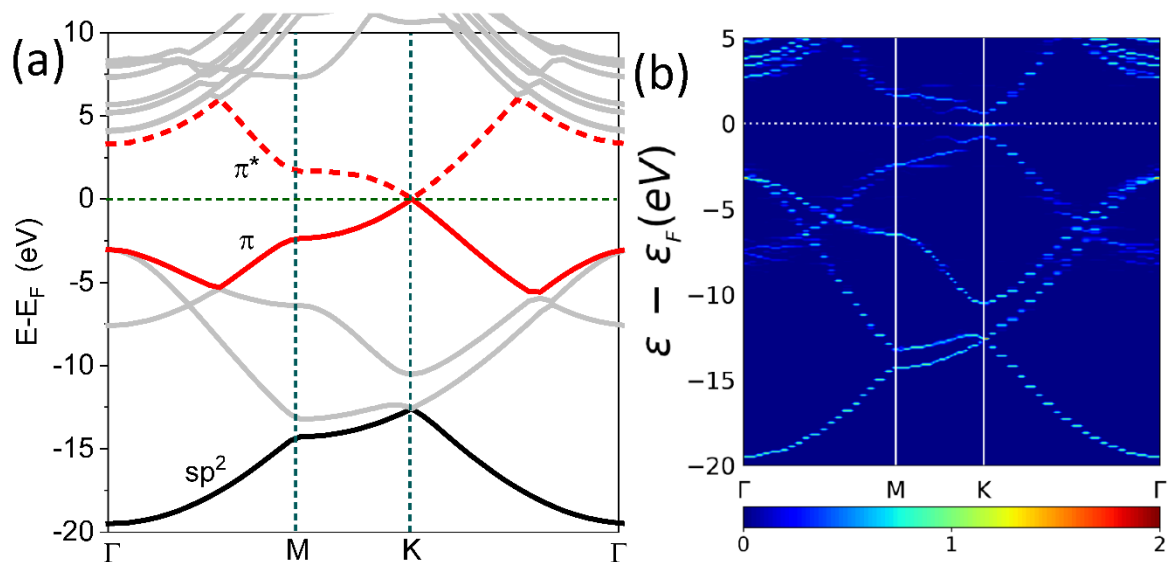


Figure S9. The band structure of (a) pristine graphene and (b) hydrogen adsorbed graphene.

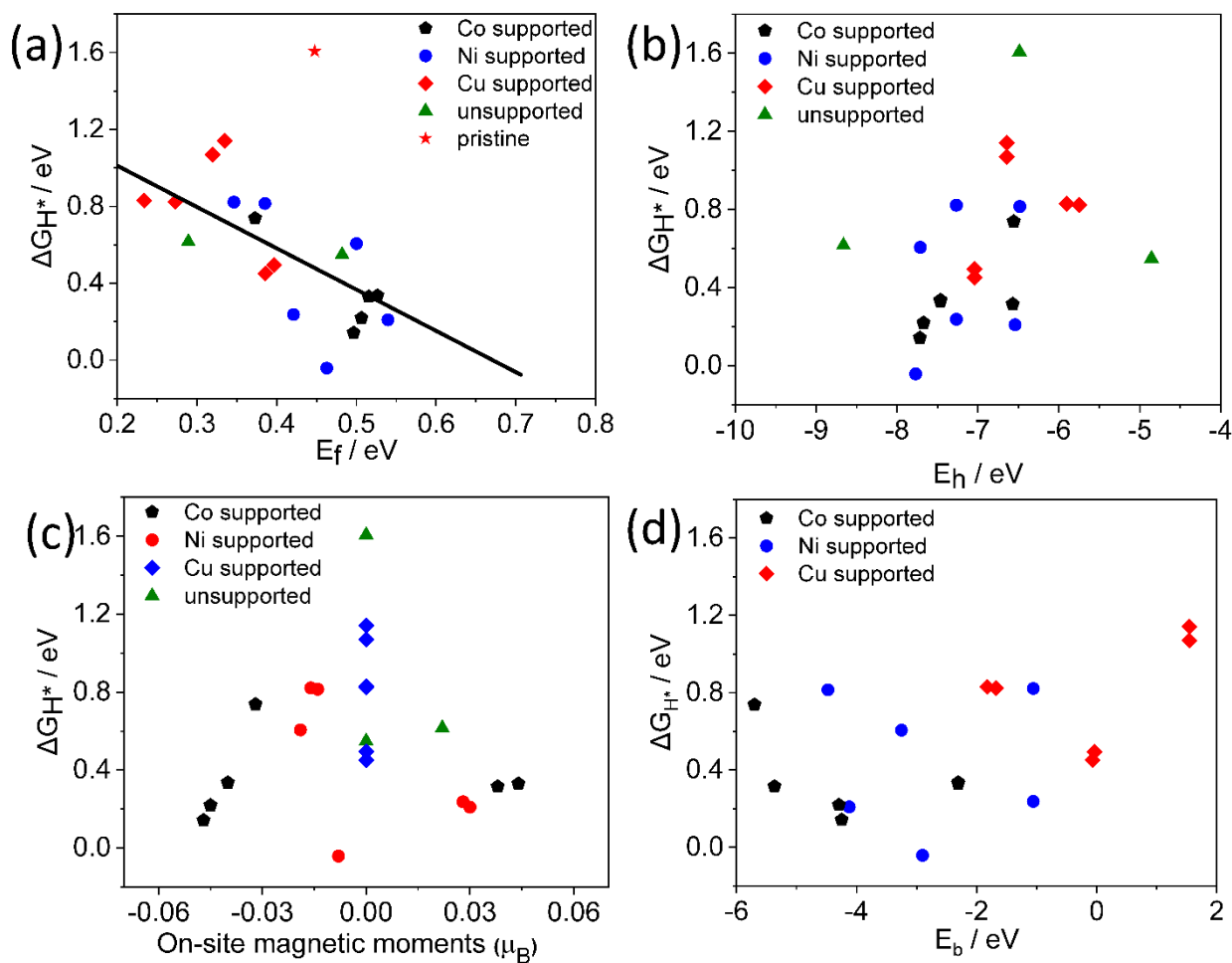


Figure S10. The relationships between free adsorption energy of hydrogen ΔG_{H^*} and (a) the formation energy of carbon vacancy; (b) the energy level of the highest peak in the density of states of an active carbon atom; (c) the on-site magnetic moments; (d) The binding energy of graphene sheets and metal substrates.

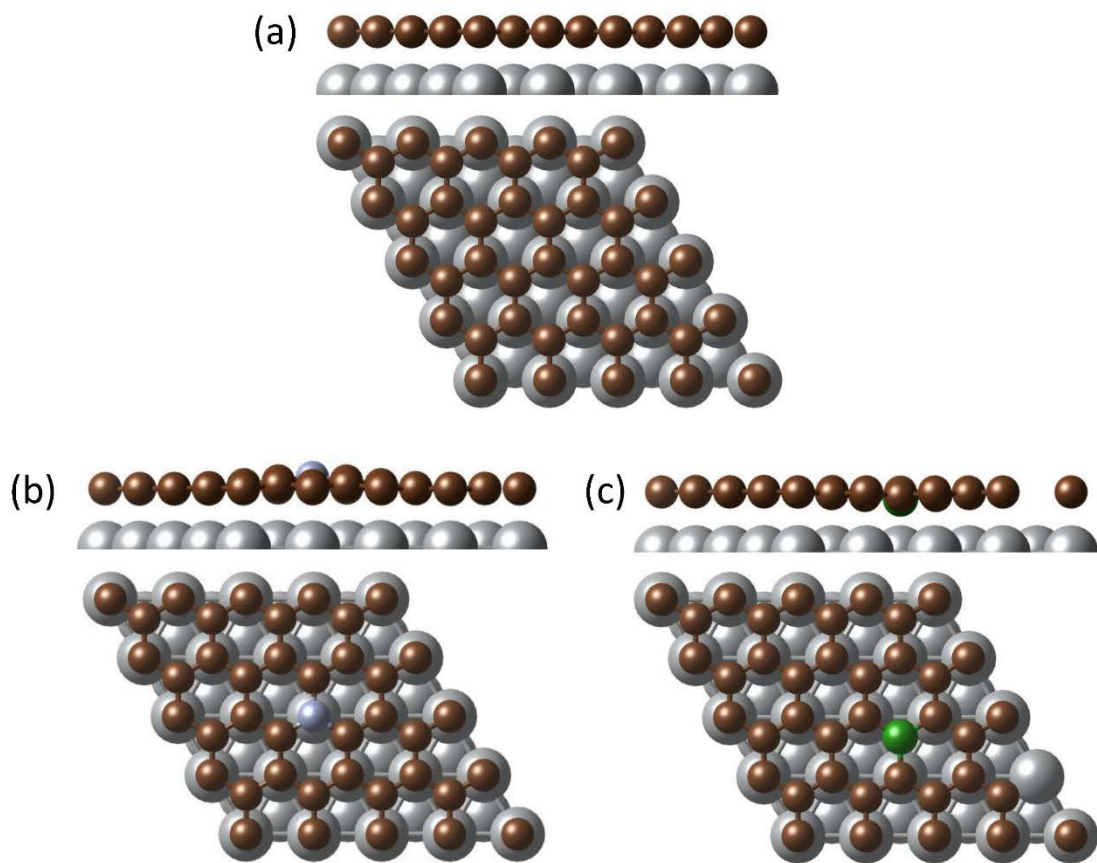


Figure S11. The atomic structures of Ni supported (a) pristine graphene; (b) N-doped graphene; (c) B-doped graphene.

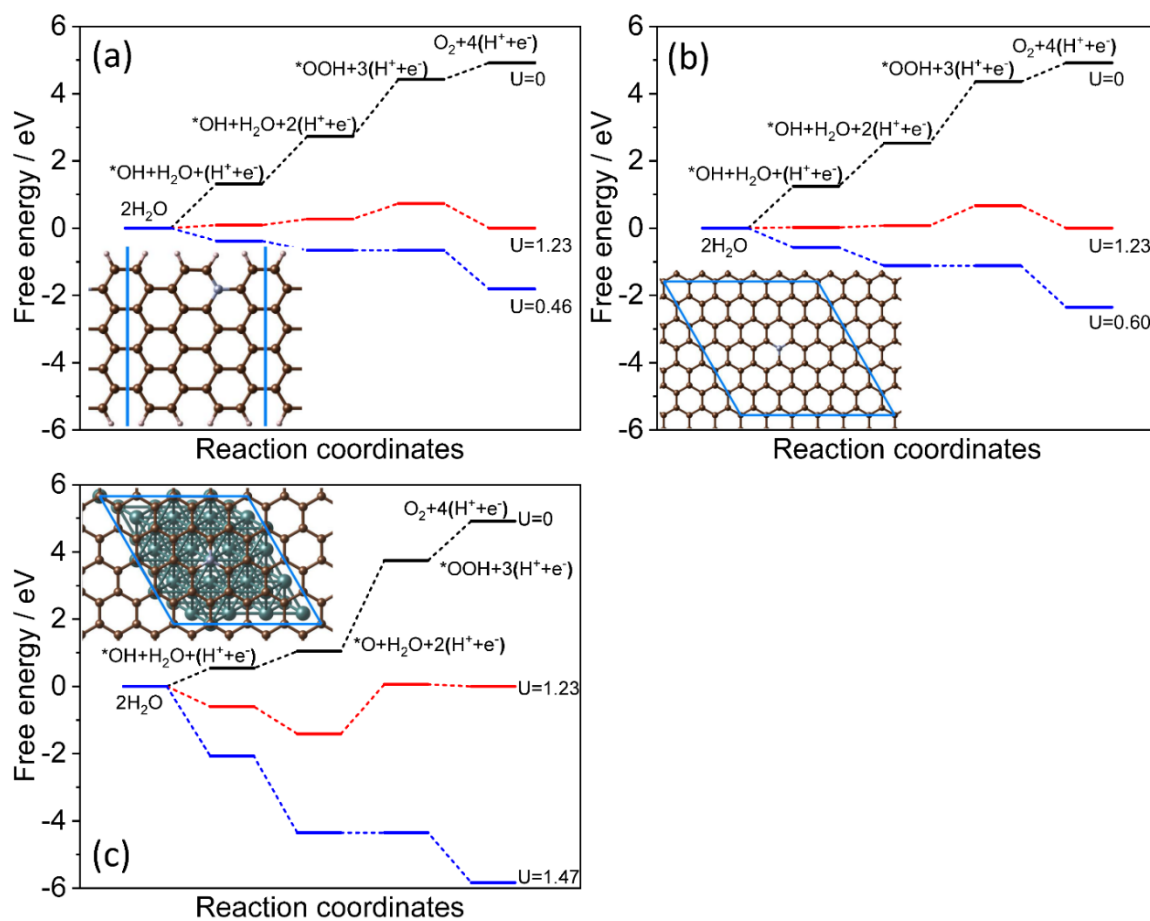


Figure S12. Schematic energy profiles for the OER pathway on (a) graphitic-N edge, (b) graphitic-N bulk and (c) graphitic-N@Ni

Table S1. Comparison of the catalytic activity toward the HER in 1 M KOH of the NCNTs@NiF with other reported high performance HER catalysts. a: 20 mA cm⁻², b: 1M NaOH.

Electrocatalysts	j =10 (mA cm ⁻²)	Tafel Slop (mV dec ⁻¹)	Reference
NCNT NiF	128 ^a	112.04	This work
NiFe-OH-PO ₄ /NiF	135 ^a	33.4	[1]
NiFe LDH@NiCoP/NiF	120	88	[2]
Mo _{0.6} Ni _{0.4} /Ti foil	65	72	[3]
NiFe-MOF	134	42	[4]
CoNiN@C/CuF	120	140	[5]
NiCo ₂ S ₄ /NiF	210	58.9	[6]
Hierarchical NiCo ₂ O ₄ hollow microcuboids	110 ^b	49.7	[7]
FeSe ₂ /NiF	178	/	[8]
Fe-Ni@NC-CNTs/GCE	202	113.7	[9]
Co ₁ Mn ₁ CH/NiF	180	/	[10]
Ni ₅ P ₄ nanosheets/NiF	150	53	[11]
Mo _{5.9} Ni _{94.1} S/NiF	60.8	39.2	[12]
NiSe-Ni _{0.85} Se/CP	101	74	[13]
Co(OH) ₂ @NCNTs/NiF	170	/	[14]

Table S2. Comparison of the catalytic activity toward the HER in 1 M KOH of the NCNTs@NiF with other reported high performance OER catalysts. a: 20 mAcm⁻², b: 1M NaOH, c: 30mA cm⁻².

Electrocatalysts	J=10 (mA cm ⁻²)	Tafel Slop (mV dec ⁻¹)	Reference
NCNT NiF	250 ^a	52.4	This work
NiFe-OH-PO ₄ /NiF	249 ^a	41.76	[1]
NiFe LDH@NiCoP/NiF	220	48.6	[2]
Mo _{0.6} Ni _{0.4} /Ti foil	290	42	[3]
CoNiN@C/CuF	265	56	[5]
NiCo ₂ S ₄ /NiF	260	40.1	[6]
Hierarchical NiCo ₂ O ₄ hollow microcuboids	290 ^b	53	[7]
FeSe ₂ /NiF	245	/	[8]
Fe-Ni@NC-CNTs/GCE	274	45.47	[9]
Co ₁ Mn ₁ CH/NiF	294 ^c	/	[10]
W _{0.5} Co _{0.4} Fe _{0.1} /NiF	310	32	[15]
NiCo ₂ O ₄ @ FeOOH/NiF	187	24.18	[16]
Mo _{5.9} Ni _{94.1} S/NiF	213	35.1	[12]
NiSe-Ni _{0.85} Se/CP	300	98	[13]
Co(OH) ₂ @NCNTs@NF,	270	72	[14]

Table S3. Comparison of the catalytic activity toward the overall water splitting in 1 M KOH of the NCNTs@Ni-F with other reported high performance bi-functional catalysts.

Catalyst	Cell voltages (V) at		Reference
	J=10 mA cm ⁻²		
NCNT/Ni-F	1.75		This work
Co(OH) ₂ @NCNTs@NiF	1.72		[14]
Ni@NiO@NiF	1.71		[13]
Co-P/NC@CC	1.77		[17]
Hierarchical			
NiCo ₂ O ₄ hollow	1.65		[7]
microcuboids			
FeSe ₂ /NiF	1.78		[8]

Table S4. The bind energy E_b between metal substrates and graphene and the height of graphene sheets on different metal supports.

	TH		FH		TF	
	E _b (eV)	h (Å)	E _b (eV)	h (Å)	E _b (eV)	h (Å)
Co	-0.128	2.099	-0.061	2.430	~	~
Ni	-0.078	2.179	-0.070	2.349	-0.079	2.163
Cu	-0.008	3.104	0.002	3.253	-0.018	3.031

Reference

- [1] Z. Lei, J. Bai, Y. Li, Z. Wang, C. Zhao, Fabrication of Nanoporous Nickel-Iron Hydroxylphosphate Composite as Bifunctional and Reversible Catalyst for Highly Efficient Intermittent Water Splitting, *ACS Appl. Mater. Interfaces*, 9 (2017) 35837-35846.
- [2] H. Zhang, X. Li, A. Hähnel, V. Naumann, C. Lin, S. Azimi, S.L. Schweizer, A.W. Maijenburg, R.B. Wehrspohn, Bifunctional Heterostructure Assembly of NiFe LDH Nanosheets on NiCoP Nanowires for Highly Efficient and Stable Overall Water Splitting, *Adv. Funct. Mater.*, 28 (2018) 1706847.
- [3] T. Zhang, X. Liu, X. Cui, M. Chen, S. Liu, B. Geng, Colloidal Synthesis of Mo-Ni Alloy Nanoparticles as Bifunctional Electrocatalysts for Efficient Overall Water Splitting, *Adv. Mater. Interfaces*, 5 (2018) 1800359.
- [4] J. Zhang, T. Wang, P. Liu, Z. Liao, S. Liu, X. Zhuang, M. Chen, E. Zschech, X. Feng, Efficient hydrogen production on MoNi₄ electrocatalysts with fast water dissociation kinetics, *Nat. Commun.*, 8 (2017) 15437.
- [5] M. Liu, W. Zheng, S. Ran, S.T. Boles, L.Y.S. Lee, Overall Water-Splitting Electrocatalysts Based on 2D CoNi-Metal-Organic Frameworks and Its Derivative, *Adv. Mater. Interfaces*, (2018) 1800849.
- [6] A. Sivanantham, P. Ganesan, S. Shanmugam, Hierarchical NiCo₂S₄Nanowire Arrays Supported on Ni Foam: An Efficient and Durable Bifunctional Electrocatalyst for Oxygen and Hydrogen Evolution Reactions, *Adv. Funct. Mater.*, 26 (2016) 4661-4672.
- [7] X. Gao, H. Zhang, Q. Li, X. Yu, Z. Hong, X. Zhang, C. Liang, Z. Lin, Hierarchical NiCo₂O₄ Hollow Microcuboids as Bifunctional Electrocatalysts for Overall Water-Splitting, *Angew. Chem. Int. Ed.*, 55 (2016) 6290-6294.
- [8] C. Panda, P.W. Menezes, C. Walter, S. Yao, M.E. Miehl, V. Gutkin, K. Meyer, M. Driess, From a Molecular 2Fe-2Se Precursor to a Highly Efficient Iron Diselenide Electrocatalyst for Overall Water Splitting, *Angew. Chem. Int. Ed.*, 56 (2017) 10506-10510.
- [9] X. Zhao, P. Pachfule, S. Li, J.R.J. Simke, J. Schmidt, A. Thomas, Bifunctional Electrocatalysts for Overall Water Splitting from an Iron/Nickel-Based Bimetallic Metal-Organic Framework/Dicyandiamide Composite, *Angew. Chem. Int. Ed.*, 57 (2018) 8921-8926.

- [10] H. Duan, D. Li, Y. Tang, Y. He, S. Ji, R. Wang, H. Lv, P.P. Lopes, A.P. Paulikas, H. Li, S.X. Mao, C. Wang, N.M. Markovic, J. Li, V.R. Stamenkovic, Y. Li, High-Performance Rh₂P Electrocatalyst for Efficient Water Splitting, *J. Am. Chem. Soc.*, 139 (2017) 5494-5502.
- [11] M. Ledendecker, S. Krick Calderon, C. Papp, H.P. Steinruck, M. Antonietti, M. Shalom, The synthesis of nanostructured Ni₅P₄ films and their use as a non-noble bifunctional electrocatalyst for full water splitting, *Angew. Chem. Int. Ed.*, 54 (2015) 12361-12365.
- [12] C. Du, Y. Men, X. Hei, J. Yu, G. Cheng, W. Luo, Mo-Doped Ni₃S₂ Nanowires as High-Performance Electrocatalysts for Overall Water Splitting, *ChemElectroChem*, 5 (2018) 1-8.
- [13] H. Sun, Z. Ma, Y. Qiu, H. Liu, G.G. Gao, Ni@NiO Nanowires on Nickel Foam Prepared via "Acid Hungry" Strategy: High Supercapacitor Performance and Robust Electrocatalysts for Water Splitting Reaction, *Small*, (2018) e1800294.
- [14] P. Guo, J. Wu, X.-B. Li, J. Luo, W.-M. Lau, H. Liu, X.-L. Sun, L.-M. Liu, A highly stable bifunctional catalyst based on 3D Co(OH)₂@NCNTs@NF towards overall water-splitting, *Nano Energy*, 47 (2018) 96-104.
- [15] Y. Pi, Q. Shao, P. Wang, F. Lv, S. Guo, J. Guo, X. Huang, Trimetallic Oxyhydroxide Coralloids for Efficient Oxygen Evolution Electrocatalysis, *Angew. Chem. Int. Ed.*, 56 (2017) 4502-4506.
- [16] L. Tao, M. Li, S. Wu, Q. Wang, X. Xiao, Q. Li, M. Wang, Y. Fu, Y. Shen, Sea coral-like NiCo₂O₄@(Ni, Co)OOH heterojunctions for enhancing overall water-splitting, *Catal. Sci. Technol.*, 8 (2018) 4151-4158.
- [17] X. Liu, J. Dong, B. You, Y. Sun, Competent overall water-splitting electrocatalysts derived from ZIF-67 grown on carbon cloth, *RSC Adv.*, 6 (2016) 73336-73342.

Summary and outlook

The development of high-efficient and high-stability carbon-based catalyst, e.g. graphene, N-doped graphene, and N-doped carbon nanotubes, for energy storage and conversion, e.g. solid acid fuel cell, vanadium redox flow battery, electro/photocatalytic water splitting, and more, was the scope of the thesis.

In the first part of this thesis, high-quality monolayer graphene was synthesized over the Cu foil via a low-pressure CVD system. A simple 2-dimensional electrode consisting of the solid acid fuel cell electrolyte material CsH_2PO_4 combined with a graphene layer as a metal-free catalyst to study the electrochemical activity of ORR, which can be performed by the diameter of the impedance arc. The ORR impedance was remarkably reduced when pristine 1-LG served as cathode electrode compared with that of graphene free. The excellent electrochemical performance was achieved by introducing O_2 plasma and N_2 plasma. The DFT calculation explored that the improvement of catalytic activity induced by plasma treatment could be attributed to two beneficial consequences. The first consequence was to break the graphene sheets and create more edge sites. The second consequence was to dope heteroatoms into the basal plane of graphene sheets and surface functional groups, which substantially altered the electronic structure of the carbon active sites via the electron-withdrawing effect. This discovery that the zigzag (ZZ) carbon is the most active site for the oxygen reduction reaction (ORR) on both the O_2 and N_2 plasma-etched graphene. Furthermore, the armchair (AM) carbon adjacent to the surface oxygen groups and doping heteroatom is another main active site for O_2 and N_2 plasma-etched graphene, respectively. The results of this study will guide future endeavours in developing non-precious metal catalytically active and stable materials for fuel cell cathodes.

The development of a novel high-stable and high-efficient promising electrode for the all-vanadium redox flow battery (VRFB) is the second scope of this thesis. Owing to that it is considered one of the most promising solutions for stationary storage of fluctuating renewable energy. Firstly, the nanocrystalline graphene was directly grown over the $(\text{Ti})_{\text{hcp}}$ substrate by tailoring the phase transition temperature. Followed then, the electrochemical performance of isolated pristine graphene, nanocrystalline graphene, and N-doped graphene towards the V(IV)/V(V) redox pair was investigated

due to the Ti as inert substrate towards the mentioned reaction. The general trend of irreversible peak current density of these electrodes is: NG@Ti > G@Ti > NCG@Ti > Ti. The asymmetric conductance behavior in the metal-graphene interface, as well as high contact resistance between graphene and Ti, could be the main reason that irreversible response occurs on various electrodes. Besides, the poor activity of NCG@Ti electrode compared to the case of G@Ti and NG@Ti can be assigned to the high defect density, which will lead to the scattering of the electron, and further result from the decrease of conductivity and reduction of activity. The three to five-fold anodic peak current density for G@Ti and NG@Ti electrode compared to the original Ti electrode peak can be ascribed to two reasons. The first reason was that exhibits sufficient total quantity of sp^2 carbons on G@Ti and NG@Ti electrodes, which will create abundant adsorption sites and homogenous electron transfer towards the V(IV)/V(V) redox pair reaction. The second was that the strong electron-withdrawing effect of doping nitrogen. Furthermore, the nitrogen may exhibit π - π interaction with an empty molecular orbital of $[VO]^{2+}$ or $[VO_2]^+$ in the form of N-V band. Resulting in that the delamination of graphene and degradation of peak current density during redox stage. It is reasonable that the repeating sweeping oxidation peaks drop severely with the increase in the cycle number on various electrodes. However, we first investigated the effect of individual graphene, nanocrystal graphene, and N-doped graphene on the electrochemical performance towards the $[VO]^{2+}/[VO_2]^+$ redox couple, which will propose an ingenious method to develop novel, stable, and high-efficient electrodes for large scale energy storage systems.

The investigation of 2-dimensional sp^2 carbon materials combined with inert Ti substrate demonstrated that the activity had been improved towards the V(IV)/V(V) redox pair of VRFB. The effect of isolated NCNTs on the electrochemical activity of the V(IV)/V(V) couple of VRFB was also achieved in the third part of this thesis. Where Ti-foil and Ti-mesh were used as a novel substrate to grow NCNTs by CVD at 600 °C over electrodeposited iron particles. Actually, it is largely due to that the homogeneous and rather uniform as well as individual Fe particles were contributed by using a long nucleation pulse to form nuclei on the substrate surface and a constant growth pulse to grow the nuclei into clusters, namely double pulse deposition approach. The voltammograms of both NCNTs@Ti foil and NCNTs@Ti mesh, for different deposition times of iron as well as different NCNTs growth times, displays a significant redox

activity towards the V(IV)/V(V) redox pair, making them suitable substrates for the investigation of carbon-based materials towards the given reaction. Given the difference in the two-dimensional and three-dimensional structure of the Ti foil and Ti mesh, the latter is the ten-fold current density of the former. Furthermore, NCNTs grown over Ti mesh provide promising performances towards the V(IV)/V(V) as well as the V(III)/V(IV) redox pair. Moreover, we have finished the investigation of both 2-dimensional and 3-dimensional sp² carbon nanomaterials towards the V(IV)/V(V) redox couple in this thesis, which will guide future endeavours to develop both catalytically active and stable materials for energy storage and conversion technology.

Clean and renewable energy-driven water splitting to produce H₂ and O₂ has been commonly studied as a promising way to release global energy crisis and demands. Therefore, in the last part of this thesis, we focused on exploring the excellent and stable sp² carbon nanomaterials, e.g. graphene, N-doped graphene, ultrathin graphite, and N-doped carbon nanotubes in combination with Ni foam as a catalyst towards electrocatalytic water splitting. Firstly, NCNTs, a highly abundant graphitic nitrogen and an extremely effective electrocatalyst, was directly synthesized over Ni foam at low temperature via APCVD. Additionally, the electrochemical activity of both the hydrogen evolution reaction and oxygen evolution reaction was performed by liner scanning voltammetry. The overpotentials required to achieve 20 mA cm⁻² current density in 1 M potassium hydroxide (KOH) electrolyte for oxygen evolution reaction (OER) and hydrogen evolution reaction (HER) are 250 mV and 128 mV, respectively. When the as-grown NCNTs were used as the electrocatalyst for both the cathode and anode, an overall water-splitting current density of 10 mA cm⁻² was obtained at 1.76 V vs reversible hydrogen electrode in 1 M KOH electrolyte. Furthermore, the DFT calculation coupled with experimentation revealed that the contribution of both the metal substrate and heteroatom doping to facilitate the HER performance and produce renewable energy via electrolytic water splitting. Therefore, the relative catalytic activity of NCNTs@Ni can be attributed to the following factors: (1) N-doping alters the electronic structure and further optimizes the reversible adsorption and desorption of H. (2) A lower-temperature synthesis of NCNTs on Ni foam ensures the presence of abundant g-N to facilitate the HER and OER. (3) High ECSAs enable close contact with the electrolyte, thus allowing more efficient utilization of the active site. (4) The increase in the content of FeNPs should not be ignored for OER. (5). The N-doped

graphite fills the region free of NCNTs, thus not only enabling good mechanical adhesion and electric connection but also improving the ECSA compared with bare Ni foam. (6). the positive C atoms adjacent to the incorporated N atom facilitate the rate-determining step via the electrophilic OER owing to electron-withdrawing effect. (8) It is reasonable that the geometric construction provides intrinsic catalytic property owing to the presence of a large amount of defect on the edge of bamboo-like NCNTs. (9) The N-doped graphene coated on Ni (111) exhibited best HER activity, which could be attributed to the proper cancellation of distortion induced by hydrogen adsorption.

The development of promising sp^2 carbon nanomaterials for energy storage and conversion has shown in this thesis. However, there are following points will be suggested for a further investigation of this work. Firstly, much more stable and efficient metal-free catalyst, such as sulphur or boron doped graphene, towards the ORR reaction for solid acid fuel cell should be studied. In additional to poor stability, the degradation of total carbon content remains a challenge. The impedance of the graphene-based electrode was remarkably improved by introducing the defective sites, surface oxygen species and doping nitrogen. However, the relationship between electrochemical performance and a high percentage of doping nitrogen combined with sufficient carbon content remain unknown. Therefore, of particular interest is the endeavor of metal-free catalysts by introducing heteroatoms on sp^2 carbon nanomaterials in the next steps.

Secondly, both Ti mesh and Ti foil served as an inert supporting electrode to study the individual electrochemical performance of N-doped carbon nanotubes, graphene, nanocrystalline graphene, and N-doped graphene. However, the most active sites should be further studied toed for porous electrode due to the effect of surface area, porosity, and double layer capacity, etc. on the electrochemical performance.